# Insight into Enceladus's ocean chemistry, habitability, and past from fractionation studies of the erupting plume

Lucas M. Fifer

A dissertation

submitted in partial fulfillment of the

requirements for the degree of

Doctor of Philosophy

University of Washington

2025

Reading Committee:

David C. Catling, Chair

Jonathan D. Toner

Drew J. Gorman-Lewis

Program Authorized to Offer Degree:

Earth and Space Sciences

©Copyright 2025
Lucas M. Fifer

University of Washington

## Abstract

Insight into Enceladus's ocean chemistry, habitability, and past
from fractionation studies of the erupting plume

Lucas M. Fifer

Chair of the Supervisory Committee:
David C. Catling
Department of Earth and Space Sciences

The erupting plume of Enceladus provides an ideal opportunity to investigate the chemistry and astrobiological potential of the subsurface ocean. However, the complexities of the eruption process likely result in a plume that is chemically fractionated and distinct from its ocean source. Chemical fractionation in the plume is not well understood, but it has ramifications for both extrapolation from plume measurements to ocean composition, and for long-term changes to the ocean chemistry due to preferential eruptive loss. In this work we (1) numerically model gas fractionation over the course of an Enceladus plume eruption, including gas exsolution from the ocean, (2) use laboratory experiments to constrain and validate our numerical models of gas exsolution, and (3) use models to investigate the long-term effects of plume eruption on Enceladus's bulk chemistry and constrain the longevity of plume eruption. We find that Enceladus's ocean is likely gas- and ammonium-rich and moderately alkaline, with free energy for

methanogenesis. We also find that terrestrial models and measurements of mass transfer can generally be applied to carbon dioxide exsolution under Enceladus conditions, but may underestimate mass transfer coefficients of insoluble gases. Finally, we constrain overall timescales of plume eruption to 30–300 Myr and find that Enceladus's early ocean may have been carbon dioxide-rich and acidic, but was more likely ammonium-rich and basic. Our work advances our understanding of this small, dynamic moon and the nature of its ocean-plume connection, and provides tools for the interpretation of future spacecraft measurements at Enceladus.

# Table of Contents



# Acknowledgements

I am grateful to so many people who have helped me complete my thesis. Here is an incomplete list.

First, I need to thank my committee members. Thank you to my advisor, David Catling, for all his advice over the years on all things science, writing, and career-related. Thanks to Jon Toner for taking me on as a grad student at the start of grad school and introducing me to Enceladus. Thanks to Drew Gorman-Lewis for lending his geomicrobial expertise and getting me hooked on aqueous chemistry. Thanks to Brook Nunn for lending her knowledge and perspective on biosignature detection and missions.

In addition to David and Jon, I need to thank my other collaborators, Fabian Klenner, Rachael Hamp, Benjamin Mousseau and Kendall Ford, without whom this work would not have been possible. Thanks to the many kind folks who have given me feedback on this research over

the years, including Baptiste Journaux, Chris Glein, Julie Castillo-Rogez, Karl Mitchell, Mohit Melwani Daswani, Pete Higgins, Steve Vance, Jason Rabinovitch, Mark Fox-Powell, Alex Berne, Ashley Schoenfeld, Wanying Kang, Colin Meyer, Noah Randolph-Flagg, Frank Postberg, and many others. Thanks also to Tori Hoehler and Alta Howells for all their support and mentorship.

A huge thank you to Mike Wong and Nick Wogan for being incredible sources of encouragement, advice, and inspiration over the years. Thank you to everyone (but especially the grads) in ESS, Astrobiology and eSTEAM for being my support network throughout grad school. Thanks to the rest of the Catling research group for being a wonderful research family.

Thanks to the planet Saturn and of course, all of its rings (and moons).

Thanks to my parents and my brother, James, for supporting me all along this journey (and especially to James for reminding me to look after myself and have fun along the way). Thanks to all my family and friends near and far for being so supportive and reminding me often that Enceladus is really, really cool.

Most importantly, thank you to my wife, Stephanie Seto, for moving to Seattle to support my grad school dreams, and sticking around even when it became clear that the rain was not going to stop. Thank you for your endless support.

Finally, thank you to Brian Eno and Kid Cudi, just in case they're reading this.

# Chapter 1: Introduction and Statement of Astrobiology Relevance

An erupting plume at the south pole of Enceladus spews a mixture of gas and micron-sized ice grains into space (Porco et al., 2006). The Cassini spacecraft flew through this plume, measuring the gas composition with a pair of mass spectrometers (Postberg et al., 2009; Waite et al., 2009). The measured composition paints a picture of an ocean source to the plumes, consistent with Enceladus's orbital motion that suggests a global liquid layer beneath the outer ice shell (Thomas et al., 2016). For the moment, Enceladus has one of the most well-understood oceans in our solar system, second only to the Earth. The plume composition hints at a mildly saline ocean, with dissolved gases, organics, active hydrothermalism, and a suite of bioessential elements that could support Enceladean life, if it is present (Khawaja et al., 2019; McKay et al., 2008; Peter et al., 2023; Postberg et al., 2018, 2023; Waite et al., 2017).

However, the plume is likely not a perfect sample of the ocean due to chemical fractionation during eruption. Different gases can be enriched or depleted along this journey, e.g., from condensation onto the icy fissure walls (Glein et al., 2015; Glein & Waite, 2020), or at the transition from aqueous to gas phase at the ocean's surface. An accurate estimation of the chemistry in the ocean therefore requires a clear and quantitative understanding of these fractionation processes, and how they would function under Enceladus conditions. Furthermore, the preferential loss of some ocean constituents may have changed Enceladus's bulk and ocean composition over time, depending on the timescales of plume eruption. The modern plume and bulk composition of Enceladus can even provide constraints on the longevity of eruption, by comparison to a reasonable (likely cometary) starting composition. The open questions and opportunities for investigation around fractionation in the Enceladus ocean-plume system motivate my thesis work, outlined below.

In Chapter 2, we investigate chemical fractionation of gases from Enceladus's ocean to plume over the course of an eruption. We use numerical models of gas exsolution at the ocean-gas interface and vapor condensation onto the icy conduit. Our model produces improved estimates on the ocean composition from plume measurements. Better understanding of the concentration of gases (such as carbon dioxide, ammonia, hydrogen and methane) in the ocean is crucial to knowing the habitability of Enceladus's ocean because dissolved gases determine the pH, nutrient availability, and free chemical energy for metabolism. This work was published in the *Planetary Science Journal* in 2022 (Fifer et al., 2022).

In Chapter 3, we validate our numerical modeling of plume fractionation through experimental analogs. Specifically, we investigate gas exsolution at the ocean-gas interface using a custom-built reaction chamber under low pressure and low temperature conditions. These experiments fill a gap in the literature by testing the validity of theoretical models built for terrestrial atmospheric settings on an Enceladus analog environment. As in Chapter 2, this experimental work is vital to our understanding of the ocean composition and potential for life. A manuscript on this work is in preparation for submission.

In Chapter 4, we model the long-term chemical evolution of Enceladus as a result of plume eruption. This work helps to constrain Enceladus's past ocean and bulk composition and the longevity of active plume eruption. This modeling work also helps to determine the source of methane measured in Enceladus's plume by examining a primordial source to the methane (in contrast to previous work that favored a biological explanation), and testing prior assumptions that Enceladus's ocean composition is in a steady state (Affholder et al., 2021).

# Chapter 2: Chemical Fractionation Modeling of Plumes Indicates a Gas-rich, Moderately Alkaline Enceladus Ocean

This chapter was published in the *Planetary Science Journal* as the following:

Fifer, L. M., Catling, D. C., & Toner, J. D. (2022). Chemical Fractionation Modeling of Plumes Indicates a Gas-rich, Moderately Alkaline Enceladus Ocean. *The Planetary Science Journal*, *3*(8), 191. https://doi.org/10.3847/PSJ/ac7a9f

It is reproduced here in full with permission of the journal.

The Planetary Science Journal, 3:191 (19pp), 2022 August https://doi.org/10.3847/PSJ/ac7a9f
© 2022. The Author(s). Published by the American Astronomical Society.
OPEN ACCESS

# Chemical Fractionation Modeling of Plumes Indicates a Gas-rich, Moderately Alkaline Enceladus Ocean

Lucas M. Fifer, David C. Catling, and Jonathan D. Toner
Department of Earth and Space Sciences, University of Washington, Seattle, WA 98195, USA; lufifer@uw.edu
*Received 2021 July 18; revised 2022 June 12; accepted 2022 June 17; published 2022 August 11*

## Abstract

Enceladus harbors an ocean beneath its ice crust that erupts spectacular plumes from fissures at the south pole. The plume composition was measured by the Cassini spacecraft, and provides evidence for the ocean's gas content, salinity, pH, and potential for life. Understanding the ocean's composition is complicated by physicochemical processes that alter the plume composition during eruption, such as water vapor condensation in the icy fissures and gas exsolution from the ocean surface. We developed a model that includes key fractionation processes, in particular fractionation during gas exsolution, which has not been previously considered. Our model predicts a moderately alkaline (pH 7.95–9.05), gas-rich ocean ($\sim 10^{-5}$–$10^{-3}$ molal) with high concentrations of ammonium ions ($10^{-2}$–$10^{-1}$ molal). Our derived dissolved gas concentrations are higher than in recent studies because we account for gas exsolution, which depletes gases in the plume compared to the ocean, and because our model conserves mass flow rates between gas exsolution from the ocean and eruption from the tiger stripe fissures. We find carbon dioxide and hydrogen concentrations that could provide sufficient chemical energy for oceanic life in the form of hydrogenotrophic methanogens. Carbon dioxide concentrations of $10^{-5}$–$10^{-3}$ molal indicate a more Earth-like pH than the pH ~8.5–13.5 in previous studies. The inferred bulk ammonium and total inorganic carbon concentrations are consistent with cometary levels. This corroborates evidence from cometary deuterium-hydrogen (D/H) ratios that Enceladus formed from comet-like planetesimals. Our results suggest a gas-rich ocean that inherited its high volatile concentrations from comet-like building blocks.

*Unified Astronomy Thesaurus concepts:* Astrobiology (74); Saturnian satellites (1427); Chemical abundances (224); Water vapour (1791); Comet volatiles (2162); Methane (1042); Carbon dioxide (196)

## 1. Introduction

### 1.1. Background

Enceladus' plumes are actively erupting in the south polar region from ~100 km long 'tiger stripe' fissures (Porco et al. 2006). The plume vapor composition has been measured during several flybys by Cassini's Ion and Neutral Mass Spectrometer (INMS; Waite et al. 2006, 2009, 2017), and solid particles have been analyzed by the Cosmic Dust Analyzer (CDA; Postberg et al. 2009, 2011, 2018; Khawaja et al. 2019). The presence of sodium and potassium salts in the plume indicates an oceanic source with a salinity and approximate composition of 0.05–0.2 molal NaCl, and 0.01–0.1 molal $Na_2CO_3$ or $NaHCO_3$ (Postberg et al. 2009). Studies of the moon's orbital libration indicate that this ocean is likely global, decoupling the rocky core from the ice shell (Thomas et al. 2016). Tidal forces provide heat to maintain this ocean over long timescales (Choblet et al. 2017), and lead to the formation of tiger stripe stress fractures through which plume material erupts (Hemingway et al. 2019). Modeling suggests that the ocean partially fills the fissures and is the source of the plumes (Kite & Rubin 2016; Nakajima & Ingersoll 2016).

The plumes of Enceladus inform our understanding of the chemical conditions in the subsurface ocean, but fractionation processes create compositional differences between the plume and ocean (Glein et al. 2015; Bouquet et al. 2019; Glein & Waite 2020). In this paper, we focus on two fractionation processes that alter the composition of the plume gas during its journey: condensation of water vapor on fissure sidewalls and different rates that gases exsolve from the ocean (which has not been as extensively modeled in previous studies). We build numerical models of plume eruption that incorporate these fractionation effects to predict possible ocean compositions from the plume composition measured by the Cassini spacecraft.

### 1.2. Plume Composition Measured by Cassini

The gas component of the plume is primarily water vapor ($H_2O$), with smaller amounts of hydrogen ($H_2$), carbon dioxide ($CO_2$), methane ($CH_4$), and ammonia ($NH_3$) (see Table 1). The $H_2$ and $CO_2$ detected by the INMS are a potential source of chemical energy. In principle, life could use chemical energy in the $H_2$-$CO_2$ redox pair for methanogenesis (McKay et al. 2008; Waite et al. 2017; Affholder et al. 2021; Higgins et al. 2021). CDA analysis of the plume ice grains and INMS analysis of the plume gas found high-mass hydrocarbons (Postberg et al. 2018), and lower-mass oxygen- and nitrogen-bearing organics (Magee & Waite 2017; Bouquet et al. 2019; Khawaja et al. 2019). These organics could be a product of life, or could fuel life in the ocean.

The composition and concentration of dissolved gases in the ocean reveal Enceladus' internal physical processes and potential for biology. The concentration of $CO_2$ in the ocean is crucial for understanding the ocean's chemistry and habitability (Glein & Waite 2020). $CO_2$ lowers pH by reacting with water to form carbonic acid ($H_2CO_3$). Ocean pH impacts not only the viability of life on Enceladus (near-neutral pH often correlates with diversity of terrestrial microbial

Original content from this work may be used under the terms of the Creative Commons Attribution 4.0 licence. Any further distribution of this work must maintain attribution to the author(s) and the title of the work, journal citation and DOI.

**Table 1**
Measured Gas Abundances in Enceladus' Plume

| Species | Volume Mixing Ratio (%) |
|---|---|
| $H_2O$ | 96–99 |
| $CO_2$ | 0.3–0.8 |
| $CH_4$ | 0.1–0.3 |
| $NH_3$ | 0.4–1.3 |
| $H_2$ | 0.4–1.4 |

**Note.** From Waite et al. (2017).

communities; Keller & Zengler 2004; Fierer & Jackson 2006), but also the speciation of other dissolved ions. In particular, the aqueous speciation of ammonia is a function of pH. In the presence of free protons ($H^+$), $NH_3$ will protonate to form ammonium ($NH_4^+$), and both $NH_3$ and $NH_4^+$ are key in terrestrial metabolism (Hoch et al. 1992). Because the negative log of the equilibrium constant ($pK_a$) for the $NH_3 + H^+ \rightleftharpoons NH_4^+$ reaction is ~10.1 (at 273 K; Bates & Pinching 1949), having an ocean pH above or below this value will determine whether $NH_3$ (>10.1) or $NH_4^+$ (<10.1) dominates, and therefore the availability of these species for biology. Modeling of ocean chemistry and analysis of the erupted plume composition has produced a range of pH estimates (see Section 1.3), from acidic to highly alkaline (Marion et al. 2012; Glein et al. 2015), so that the implied $NH_4^+$ concentrations have varied widely. The wide range in ocean chemistry estimates from previous studies reflects the disparate ways plume fractionation has or has not been accounted for, which we will explore in Section 1.3.

Other gases in the plume are evidence of hydrothermal, and possibly biological, processes occurring in the ocean. Together, $CH_4$ and $H_2$ suggest hydrothermal activity at the base of Enceladus' ocean (Waite et al. 2017). Three possible sources could account for methane. Hydrogenotrophic methanogens consume $CO_2$ and $H_2$ and could produce the $CH_4$ (McKay et al. 2008; Taubner et al. 2018; Affholder et al. 2021). Methanogens on Earth thrive in anoxic environments, and their metabolic pathway is one of the earliest known metabolisms on Earth (Bapteste et al. 2005). Alternatively, methane may be produced abiotically via Fischer–Tropsch-type reactions (McCollom & Seewald 2006) associated with hydrothermal environments, although more recent studies find that abiotic production of methane in hydrothermal environments may be limited in the absence of a hydrogen vapor phase (McCollom 2016; see also Bradley 2016; Reeves & Fiebig 2020). Finally, the methane could be primordial like in comets (McKinnon et al. 2018). Better constraints on the concentrations of these gases in the ocean can help to reveal their and Enceladus' origins, by comparison with typical volatile budgets of planet-forming materials.

### *1.3. Fractionation in the Gas Phase of the Plume*

While measurements of specific chemical species in the plume allow us to infer their presence in the ocean, the *concentrations* of chemical species can differ between the ocean and plume due to fractionation. Fractionation causes certain plume components to erupt preferentially while leaving others behind, resulting in differing ocean and plume compositions. Therefore direct extrapolation of concentrations in the plume to those in the ocean could be inaccurate. Understanding fractionation is important for future missions that propose to sample Enceladus' plumes because it would allow us to translate improved measurements of the plume (Reh et al. 2016; Cable et al. 2021; MacKenzie et al. 2021) into a more complete picture of the ocean's characteristics. Here, we focus on two fractionation effects: water vapor condensation and differential gas exsolution.

Water vapor will condense out of the plume and onto the walls of the fissure as it travels upwards, enriching the relative concentrations of other gases ($CO_2$, $CH_4$, $NH_3$, and $H_2$) that do not condense significantly (Glein et al. 2015). In general, at equilibrium, the pressure and density of water vapor in contact with liquid water or solid ice is set by the temperature of the liquid or solid phase (Murphy & Koop 2005). If the pressure in the gas phase is less than this equilibrium value (the "saturation vapor pressure"), then evaporation or sublimation into the gas phase will occur; if the pressure in the gas phase is greater than the saturation vapor pressure, then condensation will occur. In Enceladus' plume, water vapor condensation is expected to occur because of the temperature difference between the base of the fissure (where ice meets the ocean) and the plume outlet at Enceladus' surface (Glein et al. 2015; Nakajima & Ingersoll 2016). As the plume vapor moves upwards through a fissure that is colder toward the surface, the plume vapor will become supersaturated with respect to the ice, and water will condense out of the plume onto the walls to restore equilibrium. The temperature of the ocean can be estimated from the freezing point of a moderately saline ocean, around 273 K, with salinity estimates of the ocean coming from the measured salt concentrations in the plume ice grains (Postberg et al. 2009). The temperature at the plume outlet is $197 \pm 20$ K based on infrared observations taken by Cassini of the tiger stripes (Goguen et al. 2013).

Glein et al. (2015) use the temperature difference between the ocean and plume outlet to estimate the vapor condensation that occurs during eruption. They assume instantaneous equilibration, so that the density of water vapor at any vertical height within the plume is equal to the saturation vapor density of the ice walls. Using this model, Glein et al. (2015) estimate that the plume loses >99% of its water vapor due to condensation.

Because condensation tends to remove water vapor without significantly affecting the other gases, condensation should produce an erupted plume with enriched concentrations of nonwater gases, which could cause overestimates of oceanic gas concentrations if not accounted for. Marion et al. (2012) do not account for vapor condensation. Instead, they assume that the plume gases are in equilibrium with the ocean. As a result, they predict relatively high gas concentrations in the ocean, including dissolved $CO_2$, and consequently an acidic ocean pH of 5.74–6.76.

By contrast, studies that accounted for water vapor condensation suggest that nonwater gases dissolved in the ocean are more dilute than in the plume. For example, Glein et al. (2015) predict a highly alkaline pH, 10.8–13.5. Other estimates for ocean pH include 8.5–9, from the distribution of salts in the plume ice grains (Postberg et al. 2009), and 8.5–10.5, from conditions necessary to form silica nanoparticles that were measured streaming away from the Saturnian

system (Kempf et al. 2005), and thought to originate from Enceladus (Hsu et al. 2015). Glein & Waite (2020) find that an ocean pH range of 8.5–9 provides the best fit to both the CDA analysis of salts in the plume ice grains (Postberg et al. 2009) and activity estimates for oceanic $CO_2$ from INMS data (after accounting for water vapor condensation out of the plume).

Gas exsolution has not yet been adequately explored but will cause further fractionation between plume and ocean concentrations. The production of plume water vapor and all plume gases are driven by differences in partial pressures between their aqueous forms in the ocean and the plume gas above it. Furthermore, differential rates of gas exsolution will fractionate gases between the aqueous and gas phases. Consequently, rapidly exsolving gases are likely enriched in the plume and slowly exsolving gases are depleted in the plume. Rates of gas exsolution can be measured experimentally or calculated via a theoretical model such as a thin-film model, wherein the rate of mass transfer is set by the rate of diffusion (theoretically or experimentally determined) over a hypothetical thin film (with experimentally determined thickness) that lies at the interface of the liquid–gas phase boundary (Cussler 2009). Because it is far more abundant than other volatiles, water enters the gas phase of the plumes at a much greater rate than other gases exsolve. Consequently, water should be enriched in the plume, and any extrapolation of plume measurements that does not account for this would underestimate dissolved gas concentrations. Gas exsolution in the Enceladus ocean–plume system counteracts the loss of water via condensation; condensation of water vapor tends to deplete the plume in water vapor relative to other gases, while gas exsolution tends to enrich the plume in water vapor.

In the rest of the paper, we outline our modeling methods used to quantify fractionation that occurs during (1) condensation of water vapor as the plume erupts through the ice fissures (Sections 2.1, 2.2), and (2) dynamic gas exsolution at the ocean–plume boundary (Section 2.3). We model these fractionation steps in the reverse order of occurrence during eruption because our goal is to begin with the measured plume composition as model input and produce an ocean composition as model output. In this modeling scheme, outputs of the condensation model are used as inputs to the gas exsolution model. We also outline how we model aqueous speciation in Enceladus' ocean (Section 2.4). Then we describe the results of our modeling efforts, and compare our predictions for ocean composition to previous studies (Section 3). Finally, we consider the implications of our results for Enceladus' origin and its chemical energy for life (Section 4).

## 2. Methods

### 2.1. Water Vapor Condensation Model

To quantify water vapor condensation, we adopt the model of Nakajima & Ingersoll (2016) for plume formation, eruption, and partial condensation. This model assumes that liquid water partially fills the tiger stripe fissures and evaporates, and the resulting plume gas accelerates toward Enceladus' surface due to strong pressure gradients (Figure 1(a)). In the past, some studies have proposed that a solid source could generate the plumes via ice sublimation and/or clathrate decomposition (Kieffer et al. 2006; Nimmo et al. 2007). However, the detection of salt-rich ice grains (Postberg et al. 2009) and silica nanoparticles in the plume (Hsu et al. 2015) strongly indicate that a liquid ocean in direct contact with a rocky core is the source of the plume (see also Spencer et al. 2018, for a review of the present state of knowledge of the plume source). In modeling the gas phase dynamics, we approximate the gas as pure water vapor, as in Nakajima & Ingersoll (2016), due to the low mixing ratios of nonwater gases (Table 1). During transport to the surface, plume water vapor condenses on the conduit walls. We assume that solid ice grains in the plume are formed via rapid freezing of aerosol-like ocean droplets that are flung from the ocean surface due to bubbling, boiling, or turbulence (Postberg et al. 2009). These particles get carried by the plume gas.

To estimate the importance of condensation onto ice grains in the plume versus the walls of the fissure, we find a ratio in the total surface areas of these two condensation sites. We calculate this ratio by approximating the grains as spherical particles 1 $\mu$m in size (Postberg et al. 2009) and with density equal to that of pure ice, approximated as the density at the freezing point, $\rho_{ice} \approx 917\ \mathrm{kg\ m^{-3}}$. The assumption of an approximately pure ice composition is justified given that even the most salt-rich ice grains are >98% water-ice (Postberg et al. 2009). With the above particle radius and density, we can estimate an average grain surface area $SA_{\mathrm{grain}} = 1.26 \times 10^{-11}\ \mathrm{m^2}$, average grain volume $V_{\mathrm{grain}} = 4.19 \times 10^{-12}\ \mathrm{m^3}$, and average grain mass $m_{\mathrm{grain}} = 3.84 \times 10^{-9}\ \mathrm{kg}$. We then use the observed dust-to-gas mass ratio, $R_{\text{dust-to-gas}} \approx 10\%$ (Hedman et al. 2018), and the plume vapor density $\rho_{\mathrm{gas}}$ (an output of the model described in the following paragraphs) to find the number density of grains in the plume within the plume conduit at a given moment, $n_{\mathrm{grains}} = R_{\text{dust-to-gas}}\rho_{\mathrm{gas}}/m_{\mathrm{grain}}$. The total surface area of all ice grains in the conduit at a given moment can be expressed as

$$SA_{\text{tot. grains}} = SA_{\mathrm{grain}} n_{\mathrm{grains}} DL\delta, \tag{1}$$

where $D$ is the total distance from the ocean–plume boundary to the plume outlet, $L$ is the length of the fissure, and $\delta$ is the (thin) width of the fissure (Figure 1(b)). The surface area of the fissure walls can be expressed as

$$SA_{\mathrm{walls}} \approx 2DL, \tag{2}$$

neglecting the small end wall area ($2D\delta$). The ratio of ice grain surface area to fissure walls is thus

$$f = \frac{SA_{\text{tot. grains}}}{SA_{\mathrm{walls}}} = \frac{SA_{\mathrm{grain}} n_{\mathrm{grains}} \delta}{2}. \tag{3}$$

Using Equation (3), we find that the ratio of ice grain surface area to wall surface area that the plume vapor encounters during eruption is about $1{:}10^9$. This is a conservative estimate as it assumes that the ice grains are stationary (and that the plume vapor "sees" all grains in the conduit), but in reality the ice grains are moving upward as well, being carried in the plume gas such that the plume vapor will only "see" a fraction of all ice grains in the conduit. From the ratio of surface areas that we calculate, we posit that vapor condensation onto the solid ice grains is negligible compared to condensation onto the walls of the conduit.

The model of plume eruption (Nakajima & Ingersoll 2016) includes conservation of mass, momentum and energy, expressed through Equations (A1)–(A3) listed in Appendix A. These three equations, along with an equation for the internal energy ($du = C_v dT$, where $u$ is the internal energy, $C_v$ is the specific heat capacity of water vapor at constant volume, and $T$ is

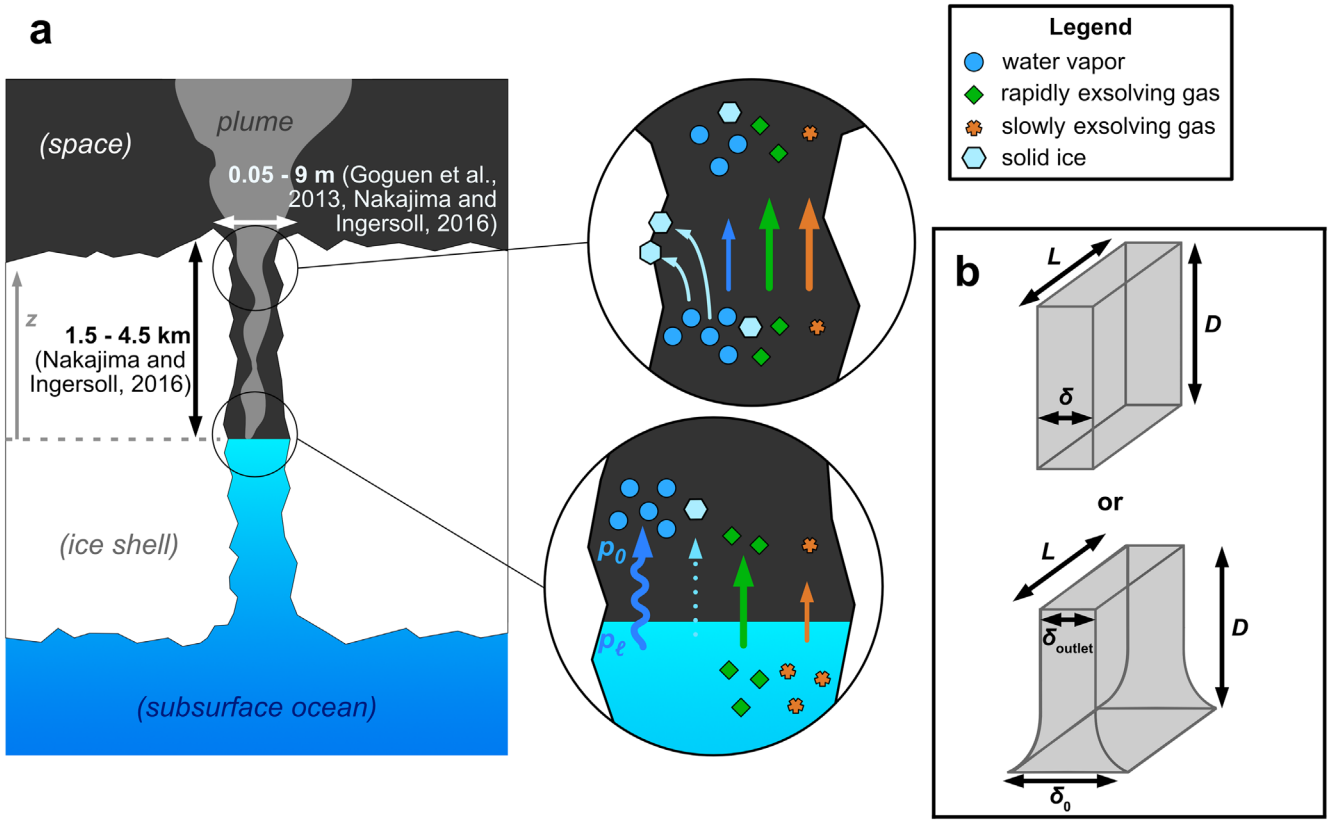


**Figure 1.** (a) A diagram showing the ocean source to Enceladus' plumes, and two key fractionation processes. In the lower-right circle, water evaporation and gas exsolution occur at different rates, enriching the plume in water vapor and those gases that exsolve rapidly. The vapor pressure of the liquid ($p_\ell$) is larger than the partial pressure of water vapor directly above the ocean ($p_0$), driving evaporation (Nakajima & Ingersoll 2016). Solid ice grains in the plume are formed via freezing of aerosol-like droplets of water, and carried in the plume gas (Postberg et al. 2009). In the upper-right circle, water vapor condenses out of the plumes onto the walls of the ice fissures, whereas other gases do not condense out significantly (Glein et al. 2015). (b) Diagrams of the modeled fissure geometries, with depth $D$ measured from the surface to the ocean—plume boundary, fissure length $L$, and either constant diameter $\delta$ or a tapering diameter starting from $\delta_0$ at the ocean and narrowing to $\delta_{\rm outlet}$ at the plume outlet (see Equation (6)).

the temperature of the plume), ideal gas law, and temperature-dependent saturation vapor pressure $p$ of ice at absolute temperature $T$,

$$p = 3.63 \times 10^{12}\ \text{Pa} \times \exp(-6137\ \text{K}/T), \tag{4}$$

are used to find expressions for the terms $dT/dz$, $du/dz$, $ds/dz$, $d\rho/dz$, $dp/dz$, and $dv/dz$. Here $z$ is the vertical distance from the gas–water interface at the bottom of the fissure (Figure 1), $s$ is the solid mass fraction of the plume, $\rho$ is the density, $p$ is the pressure, and $v$ is the velocity. Equation (4) assumes that the vapor is approximately at pressure equilibrium with the ice walls throughout the conduit, which is justified given that the expected equilibration times are on the order of milliseconds (Ingersoll & Pankine 2010). With these expressions, we use a finite-difference method beginning from the ocean–plume boundary, calculating each $d(X)/dz$ term iteratively (where $(X) = T$, $u$, $s$, etc.), stepping upward through the fissure by small (typically $\sim$1 meter) distances $\Delta z$.

For the lower boundary, at the ocean–plume interface, we use the following equation

$$\rho_0 v_0 \delta_0 = \frac{(p_\ell(T_\ell) - p_0)}{\sqrt{2\pi R T_\ell / M}} \delta_0, \tag{5}$$

from Nakajima & Ingersoll (2016) to determine the rate of water evaporation. In Equation (5), the subscript $\ell$ represents a parameter of the liquid water, and the subscript 0 represents a parameter of the bottommost numerical "cell" of the plume vapor. Here $\delta$ is the diameter of the fissure, $R$ is the universal gas constant, and $M$ is the molar mass of water. Equation (5) is a form of the Hertz relation (Persad & Ward 2016), wherein a Maxwell–Boltzmann distribution is assumed for particle velocities in both the liquid and gas phase, and mass transfer between phases is determined by the frequency with which particles collide with the phase boundary.

As in Nakajima & Ingersoll's (2016) work, we initialize the model by guessing a value for the plume gas pressure directly above the ocean ($p_0$). We use the bisection method to iteratively guess $p_0$, until we find a solution for all variables ($T$, $u$, $s$, $\rho$, $p$, $v$) as a function of $z$ such that the plume velocity $v$ at the outlet is within the range of the escape velocity from Enceladus' surface and the sound speed (given by $v_{\rm sound} = \sqrt{\gamma RT/M}$, where $\gamma$ is the ratio of specific heat capacity at constant pressure to specific heat capacity at constant volume, taken to be 1.333 for water vapor). The escape velocity is taken as a lower limit because the erupting plume vapor is observed to escape from Enceladus, while some fraction of the slower ice grains fall back to the surface (Kempf et al. 2010; Hansen et al. 2020). The speed of sound is taken as an upper limit to the plume velocity because one-dimensional flow of gas through a long pipe should remain below the speed of sound as long as the initial velocity (in this case, of the plume evaporating at the

ocean surface) is below the speed of sound (Landau & Lifshitz 1959; Nakajima & Ingersoll 2016). For additional details of the condensation model, see Appendix A, and our code, which we have made open source.

Observed heat fluxes from the south polar terrain and mass fluxes of the eruptions provide constraints on other model parameters, such as the geometry of the tiger stripe fissures. The temperature of the fissure walls, which decreases toward the outlet, is found using Equations (A4)–(A8). In these equations, the heat generated by condensation is assumed to be responsible for the elevated heat fluxes observed in Enceladus' south polar terrain in the vicinity of the tiger stripe fissures (Nakajima & Ingersoll 2016). We consider a range of possible fissure geometries, with fissure depths ($D$) ranging from 1000 meters to 5000 meters, and fissure outlet diameters ($\delta_{outlet}$) ranging from 0.05–0.1 m because these ranges allow the model to match the measured material fluxes (Hansen et al. 2017, 2020; Teolis et al. 2017). Across the different model trials we also vary the diameter of the fissure at the ocean–plume interface ($\delta_0$) from 0.05–1000 m, and the tapering rate of the fissure diameter ($d\delta/dz$). Following the work of Nakajima & Ingersoll (2016), we include models with both an unchanging fissure diameter ($d\delta/dz = 0$ so that $\delta(z) = \delta_0 = \delta_{\rm outlet}$), and an exponentially narrowing fissure where the tapering rate is defined by

$$\frac{d\delta}{dz} = \delta_{\rm outlet} + (\delta_0 - \delta_{\rm outlet}) \exp\left(-\frac{z}{Y}\right). \quad (6)$$

Here, $Y$ is a constant in units of meters (varied from 1–100 m) that corresponds roughly to the vertical distance over which the fissure narrows to its outlet diameter.

### 2.2. Effect of Vapor Condensation on Plume Gas Composition

The model of plume vapor production and partial loss via condensation provides us with five key outputs that we then use to calculate the initial *plume gas* composition, in the early stages of eruption just above the liquid water interface. The key outputs of the condensation model are the partial pressure of water ($p$) at both the ocean–plume boundary and at the plume outlet, the evaporation rate at the ocean–plume boundary ($\Phi_{\rm H_2O,evaporation}$), the eruption rate ($\Phi_{\rm H_2O,eruption}$) of water vapor at the plume outlet, as well as the pressure difference across the ocean–plume boundary ($\Delta p = p_\ell - p_0$, where $p_\ell$ is the vapor pressure of the liquid ocean). The eruption rate predicted by the model is also used to constrain which fissure geometries are most likely, as in Nakajima & Ingersoll (2016). With these key parameters in hand, we use the following equations to determine how relative abundances of plume gases are altered by condensation.

We note that under the assumption of negligible condensation for all nonwater gas species $i$, the exsolution rates (in units of kilograms per second in our calculations) for these gases from the ocean should be equal to the eruption rates seen from the fissure outlet, establishing mass conservation for the nonwater gases

$$\Phi_{i,\rm exsolution} = \Phi_{i,\rm eruption}. \quad (7)$$

Here, $\Phi_{i,\rm exsolution}$ is the exsolution rate of nonwater gas species $i$ from the exposed area of the ocean filling the tiger stripe fissure, and $\Phi_{i,\rm eruption}$ is the eruption rate from the plume outlet at the surface of Enceladus.

With the goal of finding the molar mixing ratios of gases just above the ocean–plume boundary, we can reframe Equation (7) in terms of ocean-to-plume evaporation and plume-measured eruption rates of water, and mixing ratios:

$$\underset{\text{kg s}^{-1}\text{ nonwater gas at ocean-plume interface}}{(\Phi_{\rm H_2O,evaporation})(\chi_i/\chi_{\rm H_2O})} = \underset{\text{kg s}^{-1}\text{ nonwater gas at surface of Enceladus.}}{(\Phi_{\rm H_2O,eruption})(\chi_{i,\rm Cassini}/\chi_{\rm H_2O,Cassini})} \quad (8)$$

Here, $\chi_i$ is the molar mixing ratio of each gas $i$ just above the ocean–plume boundary, and $\chi_{i,\rm Cassini}$ is the molar mixing ratio measured by the Cassini spacecraft in the plume above Enceladus (see Table 1). By mass conservation, the total mass flow rate (kg s$^{-1}$) of any gas at the surface of Enceladus is the same as at the Cassini spacecraft altitude. Consequently, in Equation (8), we take eruption rates at the surface of Enceladus as proportional to mixing ratios in the erupted plume as measured by Cassini. Also, in Equation (8), we assume that exsolution rates for nonwater gases from the ocean are proportional to their mixing ratios just above the ocean. For the mass flow rates of water, we assume that evaporation is proportional to the water vapor mixing ratio just above the ocean. Water vapor is lost to fissure walls, but although $\Phi_{\rm H_2O,evaporation} > \Phi_{\rm H_2O,eruption}$, this change in water mass flow is compensated for in Equation (8) by $\chi_i/\chi_{\rm H_2O} < \chi_{i,\rm Cassini}/\chi_{\rm H_2O,Cassini}$, such that mass conservation of nonwater gases is expressed by the equality.

The definition of Equations (7)–(8) differs from the assumptions of Glein et al. (2015) and Glein & Waite (2020) where conservation was instead framed in terms of densities. We use mass flow rates (kg s$^{-1}$) in our definition because mass flow rate is conserved for flowing fluids in a conduit while density and velocity may vary. In the condensation model described in Section 2.1 (from Nakajima & Ingersoll 2016), the plume water vapor accelerates due to pressure gradients toward the surface and the vacuum of space. Nonwater gases will accelerate similarly, meaning that velocity may increase, density may decrease, but mass flow rate for the nonwater gases must be conserved throughout the fissure.

The statement of mass conservation in Equation (7) will not apply to water vapor due to loss via condensation, so instead we define a fractional loss of water vapor,

$$f_{\rm vapor\ loss} = 1 - \frac{\Phi_{\rm H_2O,eruption}}{\Phi_{\rm H_2O,evaporation}}. \quad (9)$$

Here, $f_{\rm vapor\ loss}$ is the fraction of plume water vapor lost via condensation onto the fissure walls. Again this definition deviates from the work of Glein et al. (2015) and Glein & Waite (2020) where vapor loss was defined by a change in the vapor density. We will explore the implications of this difference in Section 3.

By combining Equations (8)–(9) we can find molar mixing ratios directly above the ocean from known plume-measured mixing ratios and derived vapor loss from the condensation model,

$$\frac{\chi_i}{\chi_{\rm H_2O}} = (1 - f_{\rm vapor\ loss})\frac{\chi_{i,\rm Cassini}}{\chi_{\rm H_2O,Cassini}}. \quad (10)$$

To find the partial pressures of all plume gases just above the ocean–plume interface, we use

$$p_i = \frac{\chi_i}{\chi_{H_2O}} p_{H_2O}. \quad (11)$$

Here, Equation (11) assumes that water vapor dominates the total pressure.

We additionally estimate how the salt concentration of ice grains may be altered by vapor condensation onto the grains. As described in Section 2.1, we find a ratio of surface areas for plume ice grains to fissure walls of $\sim 1{:}10^9$. For total condensation rates on the order of $\sim 10^2$–$10^3$ kg s$^{-1}$ (Nakajima & Ingersoll 2016), and assuming condensation rates proportional to the surface areas of nucleation sites ($\Phi_{\text{cond., grains}}/\Phi_{\text{cond., walls}} = SA_{\text{grains}}/SA_{\text{walls}}$) we estimate condensations rates onto ice grains of $\sim 10^{-7}$–$10^{-6}$ kg s$^{-1}$. For total plume eruption rates $\sim 10^2$ kg s$^{-1}$ (Hansen et al. 2017, 2020), the eruption rate of ice grains is $\sim$10 kg s$^{-1}$ (Hedman et al. 2018). Thus the fraction of the erupting ice grain mass that comes from condensed water vapor is only $10^{-8}$–$10^{-7}$. Because of this minimal contribution of condensed water vapor to the mass of ice grains, the salt concentrations of these grains measured by the CDA are taken as equal to salt concentrations in the ocean.

### 2.3. Models of Ocean Degassing

In order to find the abundances of dissolved gases in the ocean, we require a model of mass transfer across the ocean–plume phase boundary. Due to considerable uncertainty in the mechanisms by which the plume gas is produced, we outline three potential models for ocean outgassing (see Figure 2) in the following subsections: (1) a thin-film model of mass transfer from the ocean surface; (2) a boiling model where gases exsolve into vapor bubbles as they rise from a boiling depth <1 meter (Ingersoll & Nakajima 2016) below the ocean surface; and (3) a model proposed by Glein & Waite (2020) wherein the plume gas flux is dominated by degassing of aerosol-like droplets.

#### 2.3.1. Thin-film Gas Exsolution Model

First, we adopt a thin-film model of mass transfer to describe gas exsolution (Figure 2(a)), wherein mass transfer across the phase boundary is limited by diffusion through a hypothetical interfacial film at the ocean surface that is stagnant, i.e., not convecting (Cussler 2009). Thin-film models have also been applied to gas exsolution from the terrestrial ocean (Broecker & Peng 1982). The molar flux across this liquid–gas boundary (where ocean transitions to plume) for each gas species, *i,* is given by the following equation,

$$J_i = K_{p,i}(p_i^* - p_i). \quad (12)$$

Here, $K_{p,i}$ is an overall mass-transfer coefficient (in units of mol m$^{-2}$ Pa$^{-1}$ s$^{-1}$), $p_i^*$ is a theoretical gas partial pressure that would be in equilibrium with the concentration in the ocean (related via Henry's law: $p_i^* = x_i/H_i$), and $p_i$ is the actual partial pressure in the plume gas just above the phase boundary. Overall mass-transfer coefficients for the dissolved gases ($K_{p,i}$) are found via

$$\frac{1}{K_{p,i}} = \frac{1}{k_{x,i}H_i} + \frac{1}{k_{p,i}} \approx \frac{1}{k_{x,i}H_i}. \quad (13)$$

Here, $H_i$ is the Henry's law coefficient for gas $i$ (in units of Pa$^{-1}$; Sander 2015), $k_{x,i}$ is the liquid-sided mass-transfer coefficient (in units of mol m$^{-2}$ s$^{-1}$), and $k_{p,i}$ is the gas-sided mass-transfer coefficient (in units of mol m$^{-2}$ Pa$^{-1}$ s$^{-1}$). Henry's law and mass-transfer coefficients vary significantly between gases. The liquid-sided mass-transfer coefficient can be related to a diffusion coefficient via

$$k_{x,i} = \frac{D_i c_{H_2O}}{\Delta}. \quad (14)$$

Here, $D_i$ (in units of m$^2$ s$^{-1}$) is the diffusion coefficient through liquid water, $c_{H_2O}$ is the concentration of water ($\approx 5.55 \times 10^4$ mol m$^{-3}$), and $\Delta$ is the thickness of the interfacial thin film, often taken as 0.0001 m (Cussler 2009). The approximation in Equation (13) can be made because for most gases the diffusion coefficient through water vapor is much larger than the diffusion coefficient through liquid water, and therefore $k_{p,i} \gg k_{x,i}$. In other words, the slower diffusion through the liquid dominates the overall mass-transfer rate, effectively acting as a bottleneck.

As introduced in Equation (5), we adopt the Hertz relation to model evaporation from the ocean. We can define a mass-transfer coefficient for water in the same units as the overall mass-transfer coefficients for dissolved gases (mol m$^{-2}$ Pa$^{-1}$ s$^{-1}$) via

$$K_{p,H_2O} = \frac{1}{\sqrt{2\pi RTM}}. \quad (15)$$

Here, as in Equation (5), $R$ is the ideal gas constant, $T$ is the temperature at the ocean–plume interface, and $M$ is the molar mass of water.

To determine concentrations of gases in the ocean, we assume that the partial pressures of all gases directly above the ocean are proportional to their molar fluxes across the ocean–plume boundary (as defined in Equation (12)), e.g., for a nonwater gas species $i$ relative to water,

$$\frac{p_i}{p_{H_2O}} = \frac{J_i}{J_{H_2O}} = \frac{K_{p,i}(p_i^* - p_i)}{K_{p,H_2O}(\Delta p_{H_2O})}. \quad (16)$$

Here, $\Delta p_{H_2O}$ is the difference between the saturation vapor pressure of the liquid and the partial pressure of water in the vapor phase. Also, $p_i^*$ is as defined after Equation (12). Rearranging the above equation, we solve for the partial pressure of gas $i$ in the ocean,

$$p_i^* = p_i + \frac{p_i K_{p,H_2O}(\Delta p_{H_2O})}{p_{H_2O} K_{p,i}}. \quad (17)$$

Finally, to convert hypothetical partial pressures to molal concentrations (moles per kilogram of $H_2O$), we use

$$b_i = \frac{p_i^* H_i}{M}. \quad (18)$$

Here, $b_i$ is the molality of species $i$, $H_i$ is the Henry's law constant in units of Pa$^{-1}$, and $M$ is the molar mass of water.

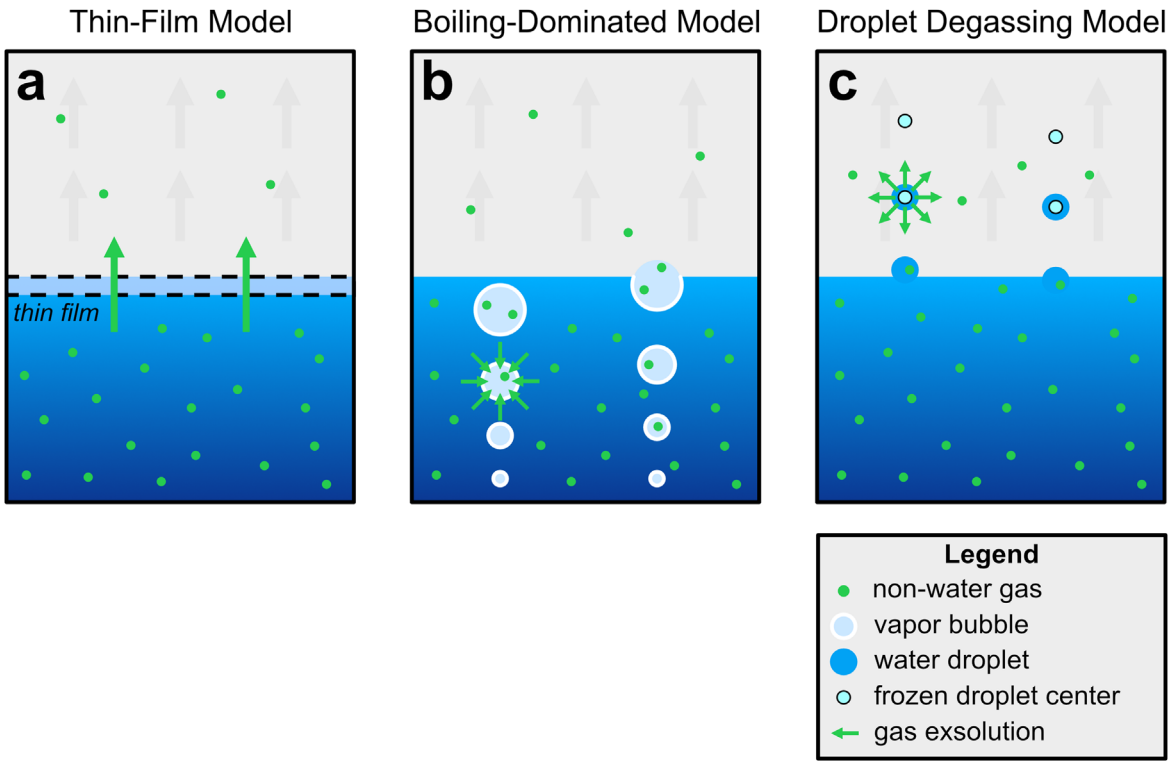


**Figure 2.** The three models of ocean outgassing considered in this study. (a) In a thin-film gas exsolution model, outgassing fluxes from the ocean are determined by diffusive mass transfer across a hypothetical stagnant (i.e., not convecting) thin film at the ocean–gas interface. (b) In a boiling-dominated model, gases exsolve into vapor bubbles that rise and grow from a boiling depth ~0.71 m below the surface (Ingersoll & Nakajima 2016). The relative gas abundances in the plume are then set by the gas abundances acquired during the bubbles' short (<5 s) journey to the surface. (c) In a droplet-dominated degassing model (Glein & Waite 2020), gas in the plume is the result of complete vaporization of the outer layer of aerosol-like water droplets, while the inner volume of the droplets freeze and form ice grains of the plume.

#### 2.3.2. Boiling Vapor Bubble Model

In the second outgassing scenario, we consider a case where the release of gas from Enceladus' ocean is dominated by vapor bubbles produced by ocean boiling under near-vacuum conditions (Figure 2(b)). We take the boiling depth of 0.71 m calculated by Ingersoll & Nakajima (2016) as the depth from which these bubbles originate. As the bubbles rise due to buoyant forces, water vapor and nonwater gases alike exsolve into the bubble. The degree to which the partial pressures of gases in the bubble equilibrate with the ocean is directly proportional to their rates of exsolution. However, unlike the thin-film model of exsolution at the surface, in the boiling scenario the gas phase (the bubble) has some time to at least partially equilibrate before it reaches the surface.

To estimate the growth of rising vapor bubbles, we adopt Rayleigh's (1917) model for spherical bubble growth:

$$\frac{dR_{\text{bubble}}}{dt} = \pm\sqrt{\frac{2}{3}\left(\frac{P_{\text{sat}}(T_\infty) - P_\infty}{\rho_l}\right)}. \tag{19}$$

Here, $R_{\text{bubble}}$ is the radius of the spherical bubble, $P_{\text{sat}}(T_\infty)$ is the saturation vapor pressure of the liquid at the far-field temperature $T_\infty$ (i.e., the temperature of the liquid), $P_\infty$ is the far-field (i.e., the hydrostatic) pressure, and $\rho_l$ is the density of the liquid. We include a thermal lapse rate of $-2.70\ \text{K m}^{-1}$ in this near-surface layer as determined by Ingersoll & Nakajima (2016), so that $T_\infty$ is a function of depth.

To estimate the velocity of the rising vapor bubbles, we use Park et al.'s (2017) parameterization for the size-dependent velocity ($v_b$) of vapor bubbles,

$$v_b = \frac{1}{\sqrt{\frac{144\mu_l^2}{g^2\rho_l^2 d_e^4} + \frac{\mu_l^{4/3}}{0.14425^2 g^{5/3}\rho_l^{4/3} d_e^3} + \frac{1}{\frac{2.14\sigma_l}{\rho_l d_e} + 0.505 g d_e}}}. \tag{20}$$

Here, $\mu_l$ is the viscosity of the liquid, $g$ is gravitational acceleration, $d_e$ is the equivalent diameter of the bubble (in the simplified spherical model we consider, $d_e = 2R_{\text{bubble}}$ always), and $\sigma_l$ is the surface tension of the liquid. While Equation (20) includes terms that describe how bubble velocity changes with shape (as large bubbles change from spheres to spherical caps; Park et al. 2017), we approximate all bubbles as spherical regardless of size, for simplicity in calculating their surface areas and volumes.

Rates of gas transfer from the dissolved aqueous phase into the bubble are found by

$$\begin{aligned}\frac{dn_i}{dt} &= K_{p,i}(p_i^* - p_{i,\text{bubble}}(t))A_{\text{bubble}}(t)\\ &= K_{p,i}(p_i^* - p_{i,\text{bubble}}(t))4\pi(R_{\text{bubble}}(t))^2.\end{aligned} \tag{21}$$

Here, $n_i$ is the total number of moles of gas $i$ in the bubble, $K_{p,i}$ is once again an overall mass-transfer coefficient in units of mol $\text{m}^{-2}$ $\text{s}^{-1}$ $\text{Pa}^{-1}$, $p_i^*$ is the partial pressure of gas $i$ in the ocean, $p_{i,\text{bubble}}$ is the partial pressure in the bubble, $A_{\text{bubble}}$ is the surface area of the bubble, and $R_{\text{bubble}}$ is the bubble radius. The changing partial pressure in the bubble is found using the

ideal gas law ($p_{i,\mathrm{bubble}}V_{\mathrm{bubble}} = n_i RT_\infty$),

$$\frac{dp_{i,\mathrm{bubble}}}{dt} = K_{p,i}(p_i^* - p_{i,\mathrm{bubble}}(t))A_{\mathrm{bubble}}(t)\frac{RT_\infty}{V_{\mathrm{bubble}}(t)} = K_{p,i}(p_i^* - p_{i,\mathrm{bubble}}(t))\frac{3RT_\infty}{R_{\mathrm{bubble}}(t)}. \quad (22)$$

Here, $R$ is the ideal gas constant, $V_{\mathrm{bubble}}$ is the volume of the spherical bubble, and we have assumed that the bubble is in thermal equilibrium with the ocean such that $T_\infty$ can be taken as the temperature of gas.

We use two different methods to determine mass-transfer coefficients for gas transfer into the bubble. The first comes from Higbie (1935), as cited in Nock et al. (2016), where a mass-transfer coefficient (in units of meters per second) is defined by

$$k_{L,i} = 2\sqrt{\frac{D_i v_b}{\pi d_e}}. \quad (23)$$

Here, $D_i$ is the diffusion coefficient of gas $i$ in water. The second formulation we use for the mass-transfer coefficient comes from Frössling (1938), as cited in Nock et al. (2016),

$$k_{L,i} = c\sqrt{\frac{v_b}{d_e}}D_i^{(2/3)}\nu_l^{(-1/6)}. \quad (24)$$

Here, $c$ is a unitless coefficient that varies from 0.42–0.95 (Nock et al. 2016) and $\nu_l$ is the kinematic viscosity ($= \mu_l/\rho_l$). The mass-transfer coefficients defined in Equations (23) and (24) are converted into overall mass-transfer coefficients (Cussler 2009) via

$$K_{p,i} = k_{x,i}H_i = k_{L,i}c_{\mathrm{H_2O}}H_i. \quad (25)$$

Here, as in the thin-film model definition in Section 2.3.1, $k_{x,i}$ is the liquid-sided mass-transfer coefficient, $c_{\mathrm{H_2O}}$ is the concentration of water, and $H_i$ is the Henry's law constant in units of $\mathrm{Pa}^{-1}$.

We take the two definitions for mass-transfer coefficients from Equations (23) and (24) as conservative upper and lower limits for the rate of gas transfer, noting that experimentally measured gas transfer rates of $CO_2$ into bubbles fall within this range (Nock et al. 2016). Because Equation (24) (Frössling 1938) provides the lower of the two estimates, we adopt the lowest value for $c$ ($= 0.42$) to find the most conservative lower limit for this mass-transfer coefficient. We also note that an overall mass-transfer coefficient calculated using the thin-film model of Section 2.3.1 (using Equations (13) and (14)) falls within the the limits provided by Equations (23) and (25) or (24) and (25), so the possibility that thin-film diffusion governs gas transfer into the bubbles is implicitly included in this boiling vapor bubble model.

To derive oceanic gas concentrations from plume ratios in the case of boiling-dominated outgassing, we must define a relationship between the partial pressures of gases above the ocean, and the partial pressures that would be in equilibrium with ocean concentrations. To accomplish this, we numerically model a bubble growing and rising from an initial depth ranging from $z = -0.71$ to $-0.01$ m, with initial zero bubble radius and zero bubble velocity. We use this range for initial depth because bubbles can nucleate at any depth within the boiling layer. We step forward in time with a finite-difference method, using Equation (19) to find the bubble's growing radius (and, in turn, the spherical bubble's surface area and volume), and Equation (20) to find the bubble's velocity (and, in turn, the bubble's vertical position $z$). During this rising and growing period, we find the changing partial pressures of $H_2$, $CO_2$, $CH_4$, and $NH_3$ in the bubble using Equation (22). When the bubble reaches the ocean surface ($z = 0$), we stop the model and note the ratio between the final partial pressure in the bubble ($p_{i,\mathrm{bubble,final}}$) and the hypothetical partial pressure in equilibrium with the aqueous phase ($p_i^*$),

$$f_{i,\mathrm{boiling}} = \frac{p_{i,\mathrm{bubble,final}}}{p_i^*}. \quad (26)$$

We assume that in the boiling-dominated outgassing model, the partial pressures in the bubble upon reaching the surface are equivalent to the partial pressures just above the ocean ($p_{i,\mathrm{bubble,final}} = p_i$). Thus combining Equations (18) and (26), we find the molality of dissolved gases in the boiling-dominated scenario to be

$$b_i = \frac{p_i}{f_{i,\mathrm{boiling}}}\frac{H_i}{M}. \quad (27)$$

Here $p_i$ is the partial pressure of gas $i$ just above the ocean (an output of the condensation model; Equation (11)), $H_i$ is the Henry's law constant, and $M$ is the molar mass of water.

Bubbles tend to nucleate in cavities on surfaces (in this case, e.g., cavities in the submerged portion of the fissure walls), growing to some "departure diameter" at which point upward forces on the bubble (e.g., buoyancy) overcome downward forces (e.g., surface tension), and the bubble detaches from the nucleation site (Jones et al. 1999). In the case of the Enceladus ocean–plume system, the initial stage of bubble growth before detachment could increase the final bubble volume and thus decrease the final partial pressure in the bubble and $f_{i,\mathrm{boiling}}$ (Equation (26)). To include this effect, we calculate the departure diameter from a semiempirical formula (Kocamustafaogullari 1983)

$$d_d = 2.64 \times 10^{-5}\left(\frac{\sigma_l}{g\Delta\rho}\right)^{0.5} me\left(\frac{\Delta\rho}{\rho_g}\right)^{0.9}. \quad (28)$$

Here, $\sigma_l$ is the surface tension of the liquid, $g$ is the gravitational acceleration, $\Delta\rho$ is the density difference between the fluid and the vapor in the bubble, and $\rho_g$ is the density of the vapor in the bubble. For the initial stationary period of bubble growth, we use the time derivative of the expanding bubble radius (Equation (19)) in place of the bubble's translational velocity when calculating mass-transfer rates from Equations (23) and (24).

#### 2.3.3. Aerosol Droplet Degassing Model

Previous work by Glein & Waite (2020) assumed a model where gas transfer into the plume occurs primarily from aerosol-like droplets of ocean spray (Figure 2(c)). That study posited that due to rapid freezing of these droplets and formation of an ice shell in the inner volume (Waite et al. 2017), degassing and evaporation should only occur from the outermost layer of the droplet. Complete degassing of this outer layer would imply equal abundances between the ocean and plume gas concentrations (Glein & Waite 2020). In this model

plume abundances can be related to ocean abundances via

$$\left(\frac{\chi_i}{\chi_{H_2O}}\right)_{\text{plume at ocean}} = \left(\frac{\chi_i}{\chi_{H_2O}}\right)_{\text{in ocean}} \quad \text{or } b_i = \frac{p_i}{p_{H_2O}M}. \quad (29)$$

Here, $b_i$ is the molality of gas $i$ in the ocean (mol $kg^{-1}$ water), $p_i$ and $p_{H_2O}$ are the partial pressures (Pa) just above the ocean of gas $i$ and water vapor, respectively, and $M$ is the molar mass of water (kg $mol^{-1}$). We will compare the outputs of this and the other two ocean degassing models in Section 3.

### 2.4. Aqueous Chemistry Model

The physical chemistry models in Sections 2.1, 2.2, and 2.3 provide a method to estimate dissolved gas concentrations in the ocean from plume measurements; additionally modeling aqueous chemistry allows us to estimate the ocean pH and concentrations of dissolved ions. In aqueous chemistry, there is charge balance, such that the total oceanic concentration of positively charged cations is equal to the total concentration of negatively charged anions. CDA analysis of the solid ice grains suggests that the dominant salts in Enceladus' ocean are NaCl and $NaHCO_3$ or $Na_2CO_3$. The salinities in the ice grains ([NaCl] = 0.05–0.2 molal, [$Na_2CO_3$ or $NaHCO_3$] = 0.01–0.1 molal) are thought to closely represent the ocean salinity (Postberg et al. 2009; see also Section 2.2). Our charge balance equation includes the concentrations of the ionic components of these salts ($Na^+$, $Cl^-$, $HCO_3^-$, $CO_3^{2-}$), the dissociation products of water ($H^+$ and $OH^-$), and the dissolved $NH_3$ speciation product ammonium ($NH_4^+$):

$$[Na^+] + [NH_4^+] + [H^+] = [Cl^-] + [HCO_3^-] + 2[CO_3^{2-}] + [OH^-]. \quad (30)$$

Here, the brackets indicate the molal concentration of the ion. To solve the above equation, due to the pH-dependent speciation of carbonates and ammonia and dissociation of water, we can rewrite many of the above species in terms of $[H^+]$ (related to the pH), equilibrium constants, and activity coefficients ($\gamma_i$). We rearrange to put known quantities on the left side:

$$[Na^+] - [Cl^-] = [HCO_3^-] + 2[CO_3^{2-}] + [OH^-] - [H^+] - [NH_4^+] = \frac{K_1\gamma_{CO_2}[CO_2^*]}{\gamma_{HCO_3^-}\gamma_{H^+}[H^+]} + 2\frac{K_1K_2\gamma_{CO_2}[CO_2^*]}{\gamma_{CO_3^{2-}}(\gamma_{H^+})^2[H^+]^2} + \frac{K_w a_w}{\gamma_{OH^-}\gamma_{H^+}[H^+]} - [H^+] - \frac{[NH_3]\gamma_{H^+}[H^+]}{\gamma_{NH_4^+}K_a}. \quad (31)$$

Here, $[CO_2^*]$ ($\approx[CO_2]$) is the total concentration of dissolved $CO_2$ and carbonic acid ($H_2CO_3$), $K_1$ is the dissociation constant of carbonic acid into bicarbonate, $K_2$ is the dissociation constant of bicarbonate into carbonate, $K_w$ is the dissociation constant for water, and $K_a$ is the dissociation constant of $NH_4^+$ into $NH_3$. To find these temperature-dependent constants at the estimated ocean temperature of 273 K, we use experimentally determined values and equations developed to match empirical data (Bates & Pinching 1949; Millero et al. 2002; Bandura & Lvov 2006). In Equation (31), $\gamma_i$ refers to the activity coefficient of a species $i$, and $a_w$ is the activity of water (see Appendix B for full calculation of activity coefficients and $a_w$).

By noting that the bulk of sodium ions are those associated with NaCl and Na-carbonate salts, we can assume the following:

$$[Na^+] = [Na^+]_{NaCl} + [Na^+]_{Na-carbonates}, \quad (32)$$

$$[Cl^-] = [Cl^-]_{NaCl}. \quad (33)$$

Since $[Na^+]_{NaCl} = [Cl^-]_{NaCl}$, Equation (31) can be simplified to

$$[Na^+]_{Na-carbonates} = \frac{K_1\gamma_{CO_2}[CO_2^*]}{\gamma_{HCO_3^-}\gamma_{H^+}[H^+]} + 2\frac{K_1K_2\gamma_{CO_2}[CO_2^*]}{\gamma_{CO_3^{2-}}(\gamma_{H^+})^2[H^+]^2} + \frac{K_w a_w}{\gamma_{OH^-}\gamma_{H^+}[H^+]} - [H^+] - \frac{[NH_3]\gamma_{H^+}[H^+]}{\gamma_{NH_4^+}K_a}. \quad (34)$$

Using $[Na^+]_{Na\text{-}carbonates} = 0.01$–$0.1$ molal, and approximating $[CO_2^*]$ as $[CO_2]$ (a quantity we have derived via the fractionation model), we solve the above equation numerically for $[H^+]$. Once $[H^+]$ is known, pH ($=-\log(\gamma_{H^+}[H^+])$) and $[NH_4^+]$ ($=[NH_3]\gamma_{H^+}[H^+]/\gamma_{NH_4^+}K_a$) are derived for the ocean. We initially assume that all activity coefficients are equal to 1 to get a rough estimate for the concentrations of all unknown ionic species ($[NH_4^+]$, $[CO_3^{2-}]$, $[HCO_3^-]$, $[H^+]$, and $[OH^-]$). We then follow the Pitzer method (described in Appendix B) to find the activity coefficients for ions and the activity of water. We plug these activity coefficients and the activity of water into Equation (34) and iteratively repeat until our numerical solutions for dissolved concentrations converge.

### 2.5. Implications for Possible Methanogenesis

Finally, we explore the available energy for hydrogenotrophic methanogenesis in the ocean, from the $H_2$-$CO_2$ redox pair. Following the method of Waite et al. (2017), we calculate an "apparent affinity," a measure of the available energy for the $H_2$-$CO_2$ redox pair in the ocean, via

$$A = 2.302\,6RT(\log K - \log Q), \quad (35)$$

where $R$ is the universal gas constant, $T$ is the temperature of the medium, $K$ is the equilibrium constant for the reaction, and $Q$ is the reaction quotient. As in Waite et al. (2017), $\log K$ is taken to be 37.44, while $\log Q$ is defined based on the predicted dissolved gas concentrations via

$$\log Q = \log\left(\frac{[CH_4][H_2O]^2}{[CO_2][H_2]^4}\right), \quad (36)$$

from the chemical equation $CO_2 + 4H_2 \rightleftharpoons CH_4 + 2H_2O$.

## 3. Results

We ran our model for a range of fissure geometries, with depths from 1000–5000 m, outlet diameters from 0.05–0.1 m, fissure diameters at the ocean interface from 0.05–1000 m, and tapering factors from 1–100 m, and made predictions for dissolved gas concentrations, ion concentrations, and ocean pH for each geometry. We found that narrower fissures or

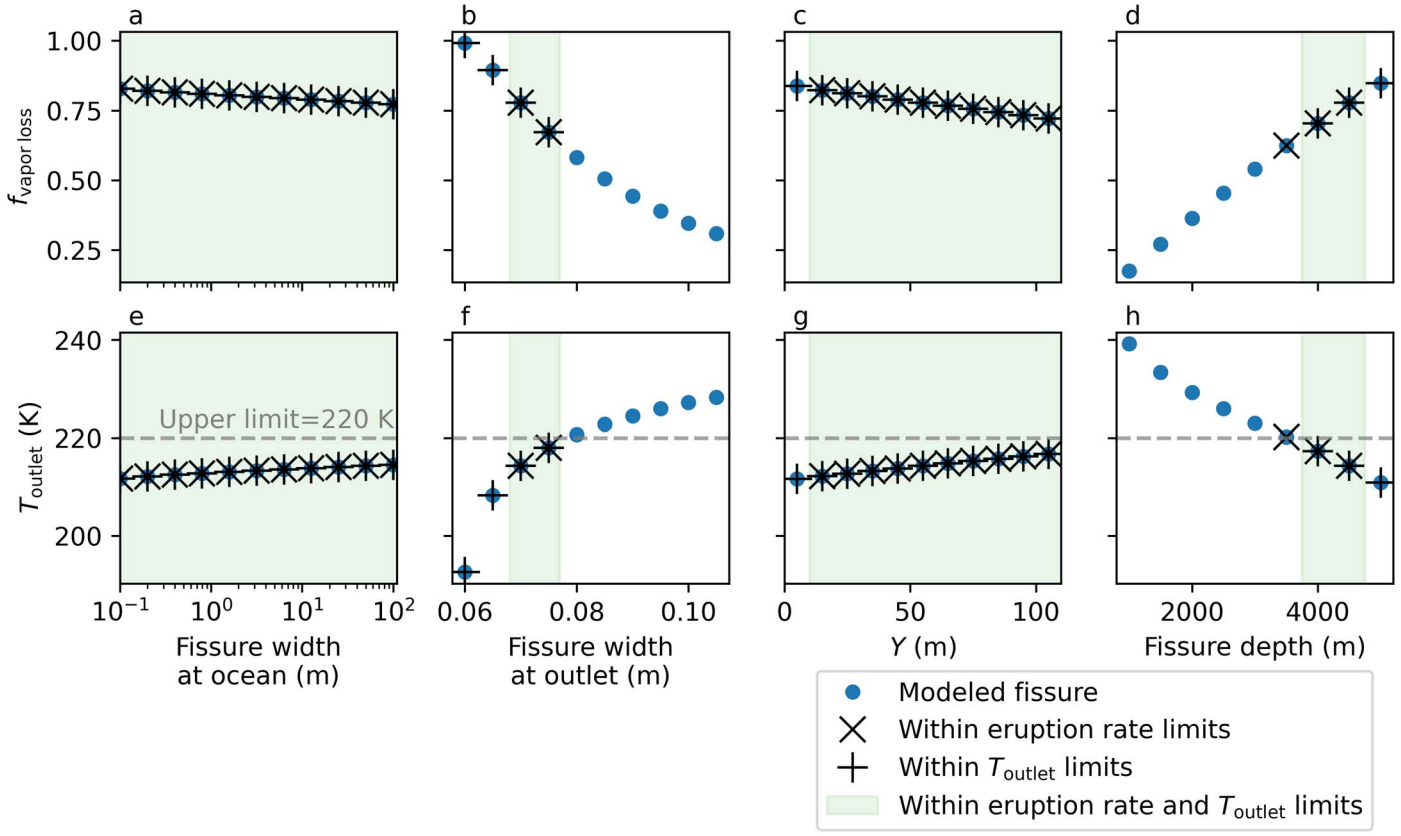


**Figure 3.** A subset of our modeling results to show the effect of fissure geometry on condensation. Top row: the fraction of plume vapor loss (a model output, defined in Equation (9)) that occurs due to condensation for different fissure geometries (model inputs), varying (a) fissure width at the ocean–plume interface, (b) fissure width at the plume outlet, (c) the tapering factor $Y$ (see Equation (6)), and (d) the depth of the fissure from outlet to ocean–plume interface. Bottom row: the temperature of the ice walls at the fissure outlet (a model output) for different fissure geometries varying (e) fissure width at the ocean–plume interface, (f) fissure width at the plume outlet, (g) the tapering factor $Y$, and (h) the depth of the fissure from outlet to ocean–plume interface. In all subplots shown here, the fissure's geometrical parameters are held constant at the following values unless varied on the $x$-axis: $\delta_0 = 50$ m, $\delta_{outlet} = 0.07$ m, $Y = 55$ m, $D = 4500$ m. Blue points indicate unrestricted model results, points with black "×"s are models that reproduce observed eruption rates of 180–338 kg s$^{-1}$ (Hansen et al. 2017, 2020), and models with black "+"s produce fissure outlet temperatures ⩽220 K (the gray dashed line in the bottom row also indicates this temperature limit). Only fissures that fit both restrictions (points with "×" and "+", also indicated by the shaded region) are deemed viable. Fissures that are narrower at the outlet or deeper overall result in a larger fraction of the plume's water vapor being removed ((b) and (d)), and thus will produce larger differences between relative gas abundances in the plume at the bottom of the conduit versus at the top (at Enceladus' surface). Fissures that are narrower at the ocean interface or have a smaller tapering factor $Y$ also tend to lose more water vapor ((a) and (c)), but the effect is less pronounced. Across all plots, $T_{outlet}$ is anticorrelated with the fraction of water vapor lost, because the final vapor pressure of the plume is tied directly to the temperature of the ice wall at the outlet (Equation (4)).

deeper fissures (where the plume has a longer distance to travel from ocean to fissure outlet) tend to result in lower predicted oceanic gas concentrations. This comes from the fact that narrower and/or deeper fissures tend to lose more water vapor via condensation (Figure 3). Therefore direct measurements of the erupted plume and lack of accounting for condensation would severely *overestimate* the concentrations of the minor (i.e., nonwater) gases in these cases. In the case of a wider and/or shallower fissure, water loss via condensation is lower so the discrepancies between plume and ocean abundances are smaller, resulting in higher predicted dissolved gas concentrations. The fractional loss of water vapor may also be understood in terms of the fissure wall's temperature: wider outlets and shallower fissures correspond to higher fissure outlet temperatures (Figure 3) and therefore smaller temperature differences between ocean and outlet. Because the vapor pressure of the plume is temperature dependent and set by rapid equilibration with the fissure walls (Equation (4)), a smaller temperature change over the eruptive journey results in less vapor lost. Fissures with narrower widths at the ocean interface and smaller tapering factors also tend to result in greater vapor loss (Figures 3(a), (c)), but the influence of these two parameters is less significant than for fissure outlet width and fissure depth (Figures 3(b), (d)) over the range of geometries considered.

We can constrain our predictions for ocean gas concentrations based on observed eruption rates, observed outlet temperature constraints, and reasonable upper limits on ion concentrations from plume ice grain composition. We first narrow our consideration of fissure geometries to only those that reproduce observed eruption rates of 180–338 kg s$^{-1}$ total plume mass (Hansen et al. 2017, 2020). We follow the example of Nakajima & Ingersoll (2016) in using this constraint, considering only fissure geometries where the erupted flux times the fissure diameter, times the total length of the fissure (taken to be 1–1.7 × 500 km) are within the uncertainty range of 180–338 kg s$^{-1}$. We also restrict our predictions based on the temperature of the ice at the plume outlet—an output parameter of the vapor condensation model. We only consider fissure models with outlet temperatures ⩽220 K, on the basis that fissures at temperatures exceeding this should sublimate away meters of ice within days, widening the fissure outlet, and rapidly exposing colder ice at greater depth and distance away from the outlet (Goguen et al. 2013). Finally, we set an upper

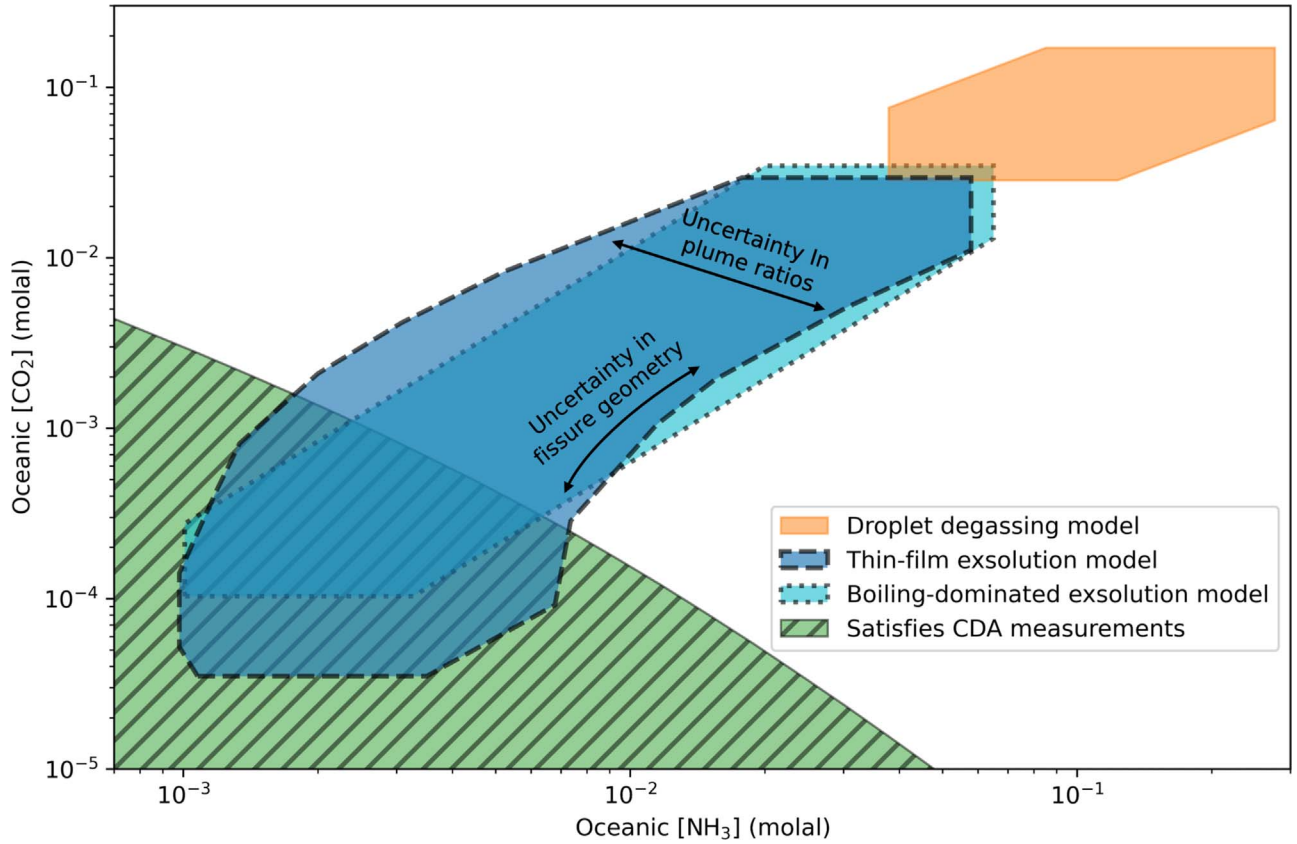


**Figure 4.** Model predictions for dissolved concentrations of $NH_3$ (horizontal axis) and $CO_2$ (vertical axis). The flat-color regions (dark blue, cyan, orange) show the range of oceanic dissolved gas predictions for each outgassing model (thin-film exsolution, boiling-dominated exsolution, and droplet degassing, respectively). For each model, the full range of predictions includes uncertainty from both the range of fissure geometries that reproduce observed eruption rates of 180–338 kg $s^{-1}$ (Hansen et al. 2017, 2020) and produce fissure outlet temperatures $\leqslant$220 K, and uncertainty in the plume measurements of gas mixing ratios (Waite et al. 2017; see Table 1). Generally the extent of each of the three regions from upper left to lower right corresponds to uncertainty in the plume mixing ratios, while the extent from lower left to upper right corresponds to uncertainty from the range of fissure geometries that match observations (both directions are indicated with labeled black arrows). The striped green region indicates the combination of $CO_2$ and $NH_3$ concentrations that are reconcilable with CDA measurements of salts; that is, [NaCl] = 0.05–0.2 molal, [$Na_2CO_3$ or $NaHCO_3$] = 0.01–0.1 molal (Postberg et al. 2009), and all ion concentrations $\leqslant$0.2 molal. The region of overlap between the striped green region and any of the other regions shows the range of predictions for a given outgassing model that is compatible with CDA measurements. The thin-film exsolution model produces the largest range in possible oceanic concentrations, the boiling-dominated exsolution model has a smaller range with similar upper limits, and the droplet degassing model does not produce any chemistries that are reconcilable with CDA measurements.

limit on ion concentrations predicted by the aqueous chemistry model. Although upper limits of ammonium ions in plume ice grains (and therefore the ocean) have not yet been defined in analysis of CDA data, if we assume comparable instrument sensitivity between $NH_4^+$ salts and salts that were measured (e.g., NaCl), we can set an estimated upper limit for all ions of 0.2 molal water (based on the upper limit established for NaCl; Postberg et al. 2009).

The three restrictions described above (eruption rate, $T_{\rm outlet}$, and ion chemistry) reduce the uncertainty in our dissolved gas concentrations to within 2–3 orders of magnitude (Figures 4, 5). Generally we predict fairly high gas concentrations in the ocean, with concentrations of $\sim 10^{-5}$–$10^{-3}$ molal (Figure 5). Specifically, we find the following molal concentrations: $[CO_2] = 3.5 \times 10^{-5}$ to $1.8 \times 10^{-3}$, $[CH_4] = 1.1 \times 10^{-5}$ to $6.4 \times 10^{-4}$, $[H_2] = 1.4 \times 10^{-5}$ to $9.3 \times 10^{-4}$, and $[NH_3] = 9.8 \times 10^{-4}$ to $7.2 \times 10^{-3}$ molal. Using the aqueous chemistry model described in Section 2.4, we obtain concentrations of ammonium ions in the ocean between 0.01 and 0.2 molal (Figure 5). Notably all fissures with widths $<\sim$5 m at the ocean-plume interface (not included in Figures 4 and 5) are ruled out of our predictions for the ocean chemistry because they lead to very high (>1 molal) concentrations of gases. Such high molalities of neutral dissolved gases like $CO_2$ and $NH_3$ further imply ion concentrations of 10–1000 molal, which would be extremely difficult to reconcile with ice grain compositions that are >98% water (Postberg et al. 2009), or solubility limits on the order of 1–10 molal.

We also find that the droplet-dominated degassing model produces high gas concentrations ($\sim 10^{-1}$ molal), and consequently ion concentrations of $10^0$–$10^2$ molal (orange region in Figure 4) that are irreconcilable with CDA measurements. This result contrasts with the findings of Glein & Waite (2020), where a droplet-dominated degassing model predicted $CO_2$ concentrations of $\sim 10^{-6}$–$10^{-3}$ molal (red error bar in Figure 5). We predict gas concentrations several orders of magnitude higher (in the droplet-dominated case) because of the difference in how we handle mass conservation during vapor condensation. In our model, we find that the initial mixing ratios of nonwater gases in the plume are lower than what was measured by Cassini, by a factor of $(1 - f_{\rm vapor\ loss})$ (Equation (10)), where $f_{\rm vapor\ loss}$ is a fractional loss defined by eruption rates, and is on the order of 0.6–0.7 (see Figure 3). By contrast, models where mass conservation and $f_{\rm vapor\ loss}$ are defined in terms of equilibrium vapor densities would generally

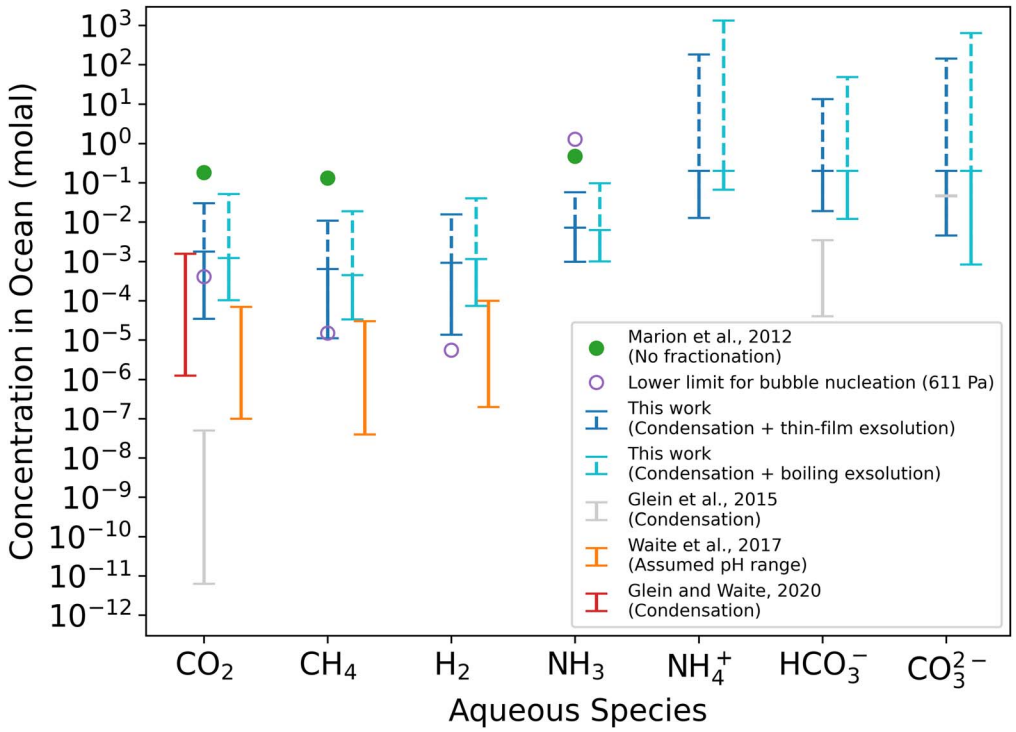


**Figure 5.** Predicted gas and ion concentrations from this work, using the thin-film model of exsolution (shown with dark blue error bars) and the boiling-dominated model of exsolution (cyan error bars) compared to previous studies. The two estimates from this work are shown as solid error bars for limits that are consistent with CDA analysis of salt content, while the dashed parts of the error bars are not consistent due to ion concentrations greater than 0.2 molal. Marion et al. (2012; green dots) assumed no fractionation between the plume and ocean. Waite et al. (2017; orange error bars) assumed a pH range of 9–11 based on prior studies, and found a $CO_2$ concentration that was consistent with that pH. They then used gas-to-gas ratios in the plume to find gas-to-gas ratios in the ocean. Glein et al. (2015; gray error bars) accounted for water vapor loss during condensation for a plume that stays in vapor pressure equilibrium with fissure walls that cool toward the surface. Glein & Waite (2020; red error bar) later reported an updated range for oceanic $CO_2$ using the same model of condensation as Glein et al. (2015) and additionally incorporating limits based on CDA measurements of salts. The open purple circles show the lowest concentration at which each gas would spontaneously form bubbles, as in a carbonated drink (Liger-Belair 2012). A limit for bubble nucleation that is below the estimates for gas concentration (seen for $H_2$) suggests that $H_2$ bubbles are likely forming in the near-surface ocean. $NH_3$ bubbles will not form because the required limit for bubble nucleation is far above the estimated oceanic concentrations.

find $f_{\text{vapor loss}} > 0.995$, and therefore much lower initial mixing ratios in the plume.

The concentrations of ammonium and ammonia calculated specifically for the droplet degassing model here may be overestimates because our model does not account for the dissociation kinetics of ammonium. Rapid dissociation of $NH_4^+$ into $NH_3$ (Perrin & Engler 1991) within liquid water aerosol droplets could occur simultaneously with droplet degassing of $NH_3$, meaning that $NH_3$ in the plume could be sourced from a combination of both ammoniacal species (rather than $NH_3$ alone, which is the assumption of all our outgassing models). The most extreme endmember case would be complete conversion of dissolved $NH_4^+$ in the outer volume of the droplet into gaseous $NH_3$, which would lead to predicted oceanic concentrations of total ammoniacal species ($\approx[NH_4^+]$ in the estimated pH regime) of $4 \times 10^{-2}$–$3 \times 10^{-1}$ molal, and therefore $[NH_3] \approx 10^{-3}$–$10^{-2}$ molal. These concentrations are more similar to the estimates of the thin-film and boiling-dominated models, but our predicted $CO_2$ concentrations would be unchanged (from the orange region in Figure 4), so we would still find no overlap between the droplet degassing model and the allowable chemistries from CDA analysis shown in Figure 4. Waite et al. (2017, Supplementary Material) found that speciation between $CO_2$, $CO_3^{2-}$, and $HCO_3^-$ is negligible on the timescales of droplet degassing and freezing, so $CO_2$ is not affected in the same way as $NH_3$. We do not expect ammonium dissociation to affect predictions for aqueous ammonia in the thin-film model. Studies of ammonia volatilization in the context of agricultural environments find that volatilization rates are predicted by thin-film models and are controlled by aqueous $NH_3$, not directly by $NH_4^+$ or total ammoniacal concentrations (Jayaweera & Mikkelsen 1990; Jayaweera et al. 1990; Montes et al. 2009).

Using our predictions for dissolved gas concentrations and the equilibrium model of aqueous chemistry, we also model a pH range for the ocean. When limiting our results to fissure geometries that reproduce the observed rates of eruption, outlet temperatures, and our estimated upper limit for $[NH_4^+]$ (Figure 4), we predict a pH range of 7.95–9.05 (Figure 6). In addition to pH variation from different fissure geometries, a large contribution to uncertainty in our predicted ocean pH stems from uncertainties in the mixing ratios of $CO_2$ and $NH_3$ in the erupted plume, 0.3–0.8 and 0.4–1.3, respectively (Waite et al. 2017). When the concentration of sodium carbonate or bicarbonate salts is varied, higher salt concentrations produce a slightly higher predicted pH, but the effect is minimal over the range of salt concentrations explored of 0.01–0.1 molal, from Postberg et al. (2009). Higher concentrations of sodium chloride salts produce a slightly lower predicted pH, due to the salinity dependence of carbonic acid dissociation constants (Millero et al. 2002) and ion–ion interactions that tend to lower activity coefficients, but the difference between a 0.05 molal NaCl ocean and a 0.2 molal NaCl ocean (the range reported in Postberg et al. 2009) is only about −0.15 pH units.

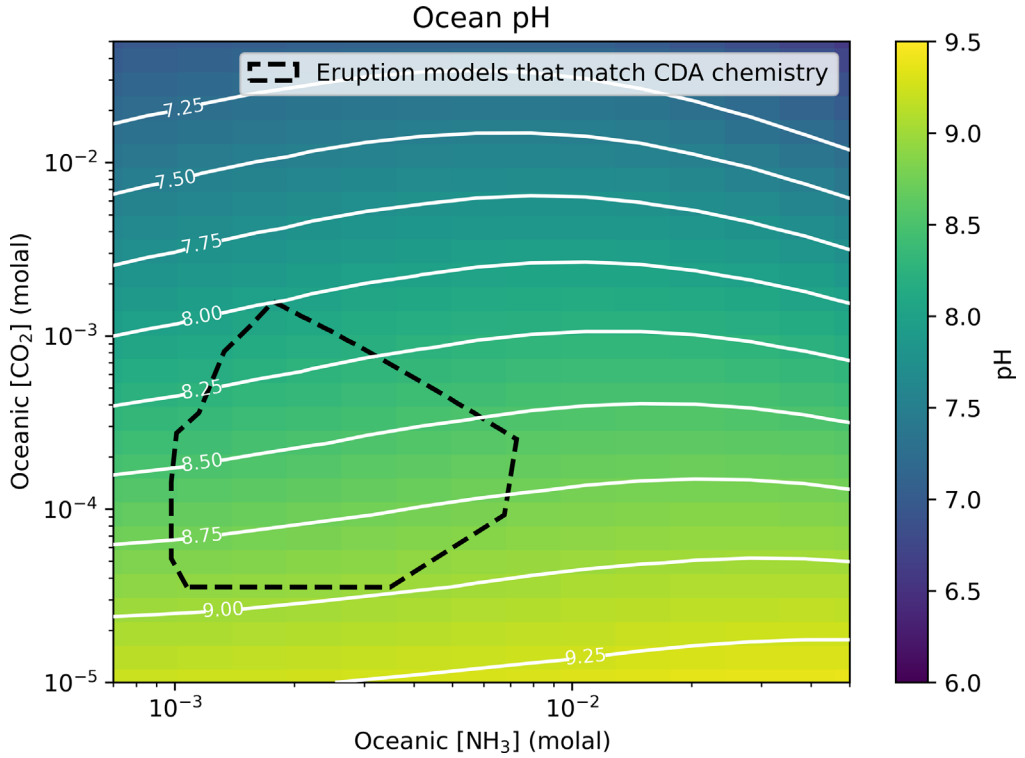


**Figure 6.** Our predicted pH for the ocean (plotted in color, with white contour lines of constant pH), as a function of predicted oceanic [$NH_3$] and [$CO_2$]. The dashed shape indicates the uncertainty space of our predictions for [$NH_3$] and [$CO_2$], and is the region of overlap between our physical chemistry models and allowable ion concentrations from the CDA analysis that was shown in Figure 4. Consequently, the full range of pH is that within the dashed shape. Higher concentrations of $CO_2$ lead to lower pH, because dissolved $CO_2$ acts as a weak acid, and higher concentrations of $NH_3$ tend to lead to higher pH, because dissolved $NH_3$ acts as a weak base. The pH range plotted here (8.00–9.00) is specific to the salt concentrations [$NaHCO_3$ or $Na_2CO_3$] = 0.05 molal and [NaCl] = 0.1 molal, but this pH range is very similar to our full predicted pH (∼7.95–9.05) that includes the full uncertainty in ocean salt concentrations (Postberg et al. 2009).

## 4. Discussion

Our model results point to Enceladus' ocean being rich in hydrogen, carbon dioxide, methane and ammonia (Figure 5). We infer dissolved gas concentrations in Enceladus' ocean that are higher than recent estimates, which accounted for condensation of water vapor in the plumes but not fractionation during gas exsolution (Glein et al. 2015; Waite et al. 2017; Glein & Waite 2020). The gas concentrations we deduce generally sit around the $10^{-5}$–$10^{-3}$ molal range, which in some cases are up to 4 orders of magnitude greater than the predicted concentrations of the aforementioned studies. However, we calculate lower gas concentrations than Marion et al. (2012), a study that accounted for neither condensation nor gas exsolution. Our values that fall below the no-fractionation model (Marion et al. 2012) are most easily explained by the enrichment and depletion of water vapor in the plume (relative to all other gases) during each fractionation process considered. As the plume travels upwards in the icy fissure, water vapor becomes *depleted* in the plume primarily due to condensation onto the fissure walls and secondarily due to condensation onto the solid ice grains. By contrast, during the gas exsolution process, water vapor is *enriched* in the plume due to its rapid evaporation rate. The fractionation processes compete but, as can be seen in Figure 5, condensation ultimately has a greater effect. If the opposite were true, we would find gas concentrations greater than the estimates of Marion et al. (2012).

A large portion of the uncertainty in our predicted gas concentrations arises from the wide range of fissure geometries that match observations, and the resultingly wide range in degrees of condensation that may occur during eruption (Figure 3). In particular, the outsized role that fissure depth and width at the fissure outlet play in controlling gas concentrations motivates additional modeling and observation to better constrain the shape and size of the tiger stripe fissures. The proposed Enceladus Orbilander mission includes a radar sounder in its suite of instruments (MacKenzie et al. 2021); if capable of resolving the fissure depth, width, and shape, such an instrument could prove invaluable for relating plume gas ratios to ocean gas concentrations in the future.

Although we present the results of the three distinct outgassing models separately, a combination of two or perhaps all three mechanisms are probably responsible for production of the plume gas. However, without empirical knowledge of the conditions at the ocean–plume interface, it is difficult to define the relative contributions of each process to the erupted gas. To compare overall outgassing rates from thin-film exsolution versus aerosol droplet degassing, we might consider the ratio of surface areas between the exposed portion of the ocean in the fissure, and suspended aerosol droplets just above it; if the surface areas of both are similar, then we would expect approximately equal contributions from both to the plume gas. Given that droplets freeze and degas in ∼1 ms (Waite et al. 2017), we need only consider droplets up to the height at which they freeze. For droplets carried at the initial velocity of the plume gas (∼3 m $s^{-1}$ from the condensation model), the height of droplet freezing is only on the order of centimeters. Even at much higher velocities of ∼100 m $s^{-1}$ that reflect the speeds of grains near the plume outlet (Schmidt et al. 2008), droplets would only reach ∼1 m above the ocean before freezing.

**Table 2**
Comparison of Enceladus' pH Range, Ocean Composition, and Differing Methodologies between this Work and Other Studies

| Source | pH Range | Composition | Method Notes |
|---|---|---|---|
| Postberg et al. (2009) | 8.5–9.0 | NaCl—$NaHCO_3$—$Na_2CO_3$ | CDA analysis |
| Marion et al. (2012) | 5.74–6.76 | $CO_2$ and $CH_4$ gas hydrates | No fractionation |
| Hsu et al. (2015) | 8.5–10.5 | ... | Based on silica formation |
| Glein et al. (2015) | 10.8–13.5 | Low ($<10^{-7}$ molal) [$CO_2$] | Condensation |
| Waite et al. (2017) | 9–11, assumed | $10^{-7}$–$10^{-4}$ molal [$CO_2$], [$CH_4$], [$H_2$] | pH sets [$CO_2$], other gases set relative to $CO_2$ |
| Glein & Waite (2020) | 8.5–9.0 | $10^{-6}$–$10^{-3}$ molal [$CO_2$] | Condensation, droplet degassing & checked against CDA analysis |
| This study | 7.95–9.05 | NaCl—$NaHCO_3$—$Na_2CO_3$ $(NH_4)HCO_3$—$(NH_4)_2CO_3$; $10^{-5}$–$10^{-3}$ molal [$CO_2$], [$CH_4$], [$H_2$], [$NH_3$] | Dynamic condensation & exsolution, comparison w/ CDA |

Taking 1 m as a very conservative upper limit, a number density of $\sim 10^{12}$ micron-size droplets per $m^3$ within 1 m of the ocean surface would be required to attain similar total surface areas between suspended aerosol droplets and the exposed ocean surface.

Could liquid aerosols be present at these number densities just above the ocean? Operating with the same assumptions of spherical, micrometer-radius, pure water-ice grains used to estimate surface areas of condensation sites in Section 2.1, we estimate a number density of ice grains near the plume outlet of $\sim 10^3$ $m^{-3}$. Assuming that the eruption rate (in kg $s^{-1}$) of ice grains at the outlet is equal to the production of aerosols at the ocean, and accounting for acceleration from $\sim 3$ to $\sim 100$ m $s^{-1}$, we estimate droplet number densities near the ocean of $\sim 10^4$ $m^{-3}$, or even lower in the case of tapering fissures that are wider at the ocean interface. That said, much like in the case of water vapor, it seems unlikely that the flux of ice grains is totally conserved during eruption, so further modeling or laboratory studies of the dynamics and fates of aerosols and ice grains in the plume is necessary. Supercooling of aerosol droplets could also extend the time and vertical distance over which droplets remain in the liquid phase, effectively increasing the total surface area from which gases could exsolve. An additional point of comparison may come from the vicinity of Earth's ocean surface, where aerosols are present at number densities up to $6 \times 10^9$ $m^{-3}$ (Fitzgerald 1991). However, the conditions at Earth's ocean surface are very different from Enceladus (e.g., winds blow across Earth's oceans, while Enceladus' ocean boils), so more targeted modeling and analog studies of aerosol formation relevant to the near-vacuum pressures in the Enceladus environment are needed.

Constraining the relative contribution of the bubble formation model to outgassing on Enceladus is also difficult, requiring knowledge of the geometry of bubble nucleation sites, which could include submerged portions of the ice shell and particles (e.g., large organics) in the ocean. However, the ocean chemistries we predict (that fall within the ionic concentration restrictions of the CDA analysis) are similar between the thin-film model and boiling-dominated model. For example, compare the dark blue and cyan error bars in Figure 5. Additionally, if one (or both) of these outgassing mechanisms produces similar fluxes to aerosol droplet degassing, then we would expect oceanic concentrations of gases and ions to fall between the lower estimates of thin-film or boiling models (blue regions in Figure 4) and the higher concentrations predicted by the droplet degassing model (the orange region in Figure 4). However, the upper limits of the thin-film and boiling-dominated models already go beyond the reasonable chemistries allowed by CDA analysis of the ice grain composition, so any contribution of droplet degassing to overall plume gas production cannot bring the predicted oceanic volatile concentrations any higher. Therefore, regardless of the dominant outgassing processes, we do not expect significant deviations from our predictions in Figure 5.

The pH we calculate for Enceladus' ocean of 7.95–9.05 is closer to neutral and more Earth-like (and possibly early Earth-like; Krissansen-Totton et al. 2018a) than recent estimates, largely due to our higher oceanic $CO_2$ content compared to most other estimates. As discussed in Section 1.3, estimates for Enceladus' ocean pH have varied widely, depending on how each study handled $CO_2$ and ultimately its concentration in the ocean (Table 2). Our pH is greater than the Marion et al. (2012) model, which has the highest concentration of oceanic $CO_2$ of all the models due to its assumption that the mixing ratios in the plume directly reflect the concentrations in the ocean. Our predicted pH of 7.95–9.05 has significance not only for the prospect of life on Enceladus (assuming Earth-like biochemistry, which tends to prefer circumneutral pH), but also for general comparisons of aqueous chemistry. A pH more comparable to Earth's ocean (a preindustrial value of 8.2) opens the door for more in situ Enceladus analog studies of terrestrial ocean environments, although it should be noted that Enceladus' ocean will likely have local pH variation near interfaces with other surfaces (e.g., at the ocean floor, near hypothesized hydrothermal vents).

We infer high ($10^{-2}$–$10^{-1}$ molal) concentrations of ammonium ions ($NH_4^+$) in the ocean, which provides support for the hypothesis that Enceladus was accreted from similar building blocks to comets. The relatively high gas

**Table 3**
Bulk Molecular Abundances of Volatiles for Enceladus as a Whole (this Study) Compared to Observed Ranges in Cometary Ices (Mumma & Charnley 2011)

| Species | Enceladus | Cometary |
|---|---|---|
| $NH_3$ | 0.001%–0.006% | 0.2%–1.4% |
| $NH_4^+$ | 0.010%–0.163% | ... |
| $NH_3 + NH_4^+$ | 0.011%–0.169% | ... |
| $CH_4$ | 0.00001%–0.001% | 0.4%–1.6% |
| $CO_2$ | 0.00003%–0.001% | 2%–30% |
| $CO_2 + CO_3^{2-} + HCO_3^-$ | 0.016–0.16% | ... |

concentrations that we calculate for oceanic $NH_3$ and the lower pH (due to high $CO_2$ abundance) are the cause of relatively high concentrations of $NH_4^+$ in our model. Assuming that our $NH_4^+$ concentration is representative of the concentration in the bulk ocean, and that $NH_4^+$ is negligible in the ice shell (and core), we can estimate a *minimum* bulk abundance for the moon of 0.011%–0.169% $NH_3$+$NH_4^+$, relative to $H_2O$. This bulk $NH_3$+$NH_4^+$, abundance is close to cometary abundances of 0.2%–1.4% $NH_3$ relative to $H_2O$ (Mumma & Charnley 2011; Table 3), and suggests that Enceladus' present-day $NH_4^+$ may have originated as primordial $NH_3$ that has largely been retained through Enceladus' evolutionary history. We also note that the large ($10^{-2}$–$10^{-1}$ molal) concentrations of $NH_4^+$ should imply the presence of ammonium-bicarbonate ($(NH_4)HCO_3$) salts in the ocean, but the $NH_4^+$ that was detected in ice grains has been interpreted as breakdown of organic molecules rather than salts (Khawaja et al. 2019). We note that ammonium bicarbonate and sodium carbonate have been detected on Ceres (De Sanctis et al. 2016; Vu et al. 2017; Carrozzo et al. 2018), a body that may have originated in the outer solar system (McKinnon 2012). The fact that our physical chemistry models allow $NH_4^+$ concentrations >1 molal (before applying the 0.2 molal limit) may motivate quantification of a precise upper limit for $NH_4^+$ in the salt-rich ice grains.

Dissolved ammonia ($NH_3$) is likely stable in the ocean, whereas ammonium ($NH_4^+$) may be incorporated into the rock of Enceladus' core. Ammonia breakdown has previously been explored as a possible source of molecular nitrogen in the plumes (Matson et al. 2007; Sekine et al. 2015; Waite et al. 2017), but even at the high ($10^{-3}$ molal) concentrations we predict, $NH_3$ decomposition into $N_2$ is likely minimal in Enceladus' ocean given the requirements of high temperatures (>700°C; Brandes et al. 1998), catalysts beyond the expected olivine or pyroxene outer core composition, and significant amounts of oxidants such as oxygen (Sekine et al. 2015). Furthermore, an upper limit on the volume mixing ratio of $N_2$ in the plume (<0.5%, Hansen et al. 2011, which translates to <0.0009 molal in our fractionation model) allows us to predict an oceanic $N_2/NH_4^+$ ratio of <0.01, indicating that $NH_4^+$ is by far the dominant N-bearing species in the ocean, and $N_2$ production is likely minimal. Dissolved $NH_4^+$ can be incorporated into minerals during aqueous alteration of terrestrial basalts (Hall 1989). If similar alteration processes occur at Enceladus' ocean floor, then our estimated bulk $NH_4^+$ abundance of 0.011%–0.169% relative to water may represent a lower limit for Enceladus.

Previous work noted that the $CO_2$ abundance in the plume and (estimated abundance) in the ocean is much lower than typical cometary levels (e.g., McKinnon et al. 2018), and we find that this is the case for both $CH_4$ and $CO_2$ in our predictions (Table 3). When including all inorganic carbon species ($CO_2$, $HCO_3^-$, and $CO_3^{2-}$) that come from $CO_2$, we predict a bulk molecular abundance for inorganic carbon of 0.016%–0.16% relative to $H_2O$, which also falls short of cometary $CO_2$ ranges of 2%–30% (Table 3). Alteration of the core through processes such as carbonation could sequester $CO_2$ from the ocean. Thus cometary $CO_2/H_2O$ is unlikely to be preserved in the aqueous phase, though the core could still contain cometary abundances in the form of carbonated rock (Glein & Waite 2020). As with $NH_4^+$, the upper end of our predicted range for Enceladus' inorganic carbon (before setting the 0.2 molal limit) includes [$HCO_3^-$] and [$CO_3^{2-}$] concentrations of >1 molal (Figure 5), which is significantly higher than the estimated 0.1 molal upper limit of $Na_2CO_3$ or $NaHCO_3$ salts (Postberg et al. 2009), again suggesting the possible presence of yet-unmeasured ammonium carbonate or bicarbonate salts. The apparent issue of missing $CH_4$ relative to cometary levels is unresolved.

We find that Enceladus' ocean likely contains abundant energy in the $H_2$-$CO_2$ redox pair that methanogens could potentially use. In Figure 7, we compare our predictions for this available energy to Waite et al. (2017), who also found significant chemical energy available in this reaction. Because we predict a positive value for the 'apparent affinity' in the ocean, there is chemical disequilibrium in the ocean environment that life could use as a source of energy. The stoichiometric coefficients in the methanogenesis reaction ($CO_2 + 4H_2 \rightleftharpoons CH_4 + 2H_2O$) dictate the exponents in the reaction quotient (Equation (36)), and therefore the importance of each species' concentration on affinity, or available energy. The higher maximum available energy that we predict compared to Waite et al. (2017) thus comes primarily from the higher concentration of $H_2$ that we estimate for the ocean, whereas an increase in concentration of $CO_2$ that we predict above the estimate of Waite et al. (2017) is approximately canceled out (in calculation of the reaction quotient) by an increase in $CH_4$ that is the same order of magnitude.

The availability of energy for methanogenesis in Enceladus' ocean could mean that there is no life there to consume it, or that any methanogenic life is nutrient limited, and therefore unable to consume $H_2$ as fast as it is introduced into the ocean. In other words, there could be a small, nutrient-limited biosphere consuming only a fraction of the available energy seen in the $H_2$-$CO_2$ pair. For instance, phosphorus is vital to terrestrial life due to its incorporation in nucleotides, cell membrane lipids, and in energy-storing molecules like adenosine triphosphate, but it has not yet been detected in the plumes. Recent work suggests that the range of affinities found here and by Waite et al. (2017) could be consistent with a methanogenic community with a limited rate at which it can draw down $H_2$, or a limited rate of population growth due to physiological and/or environmental factors (Hoehler 2022).

## 5. Conclusions

We have shown that significant chemical fractionation occurs between the erupted plumes of Enceladus and the subsurface ocean from which the plumes originate. Key chemical differences arise between the easily sampled plume and the more elusive ocean as a result of the removal of water vapor from the plume via condensation on walls of the conduit

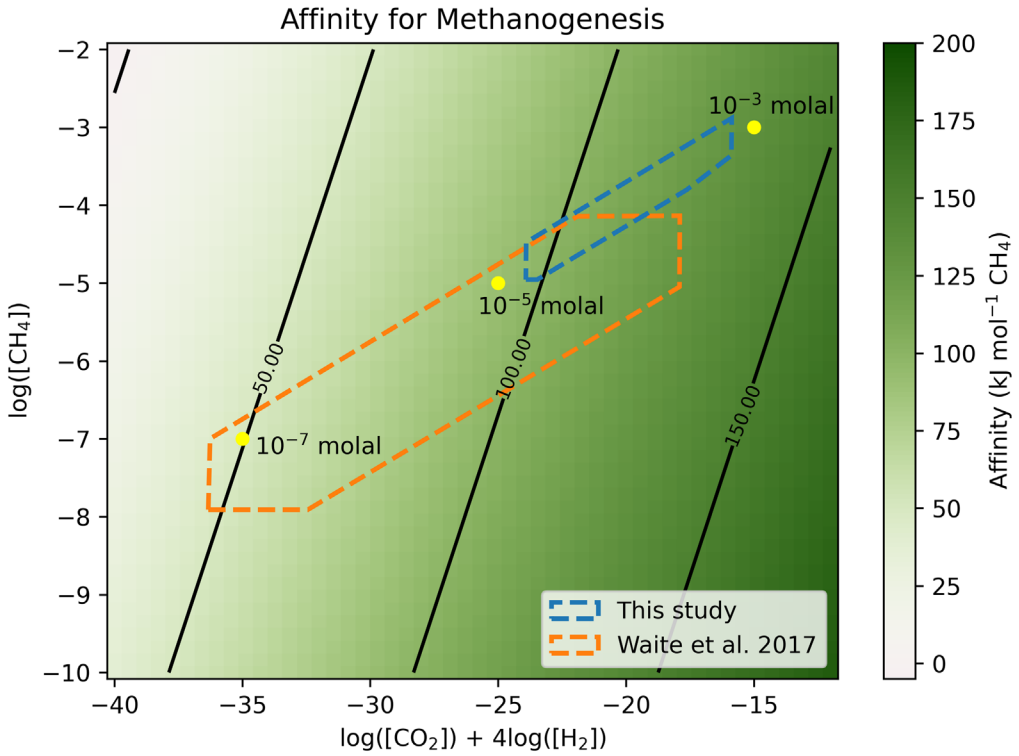


**Figure 7.** Apparent affinity for methanogenesis in the ocean, i.e., the available energy for methanogenesis per mole of reaction in the ocean shown as color shading and black contour lines. The *x*-axis represents the denominator of the reaction quotient (Equation (36)) for the methanogenesis reaction, while the *y*-axis represents the numerator of the reaction quotient (assuming the activity of water ≈1). Increasing concentrations of $CO_2$ or $H_2$ (*x*-axis) increase the energy per mole of reaction (i.e., methanogenesis is more favored), while increasing concentrations of $CH_4$ (*y*-axis) lower the energy per mole of reaction (i.e., methanogenesis is less favored). The region outlined by a blue dashed line encompasses the full range of our predictions for $CO_2$, $H_2$, and $CH_4$ concentrations, with upper limits applied from compatibility with CDA measurements. The region outlined by an orange dashed line encompasses the range of predictions for gas concentrations and affinity from Waite et al. (2017). The yellow circles are points of reference, indicating the affinity for hypothetical oceans with equal concentrations of $CO_2$, $H_2$, and $CH_4$ at $10^{-7}$, $10^{-5}$, and $10^{-3}$ molal. Due to higher gas concentrations overall, we predict a slightly greater maximum affinity, ∼130 kJ $mol^{-1}$ $CH_4$, for methanogenesis in Enceladus' ocean compared to Waite et al. (2017).

between the ocean and space, and by differential rates of gas exsolution from the ocean surface at the bottom of the conduit. Condensation and exsolution compete, through depletion and enrichment of water vapor in the plume, respectively, and while condensation ultimately has the greater effect, it is necessary to account for both processes to extrapolate Enceladus' ocean composition from plume measurements.

With new estimates for the gas content of the ocean, we find an ocean pH of 7.95–9.05, which encompasses the terrestrial ocean pH, high levels of $NH_4^+$ and inorganic carbon consistent with the accretion of Enceladus from comet-like planetesimals, and an abundance of chemical energy for potential Enceladean methanogens. We note here that our discussion of potential biology on Enceladus is decidedly biased toward terrestrial "life as we know it" (due to a lack of other examples), and therefore ocean environmental conditions such as an Earth-like pH may not necessarily be advantageous for extraterrestrial biology. Still, the availability of chemical energy from $H_2$ and $CO_2$ for methanogenesis in the ocean is independent of the chemical structure of life that uses it. Thus the statement that there is available energy for life in Enceladus' ocean need not be limited to strictly Earth-like life.

We would like to thank Christopher Glein for helpful discussions and the two anonymous reviewers for comments and suggestions that improved this paper. L.M.F. would like to thank the University of Washington Design Help Desk for their advice on figure presentation. This work was supported by the NASA Habitable Worlds Program grant No. 80NSSC19K0311. L.M.F. is also supported by NASA FINESST award number 80NSSC21K194. All source code used in this work is freely available through Zenodo (doi:10.5281/zenodo.6633691).

## Appendix A
## Details of the Vapor Condensation Model

As described in Section 2.1, we adopt Nakajima and Ingersoll's (2016) model of plume formation and eruption. Conservation of mass is expressed through

$$v\delta\frac{d\rho}{dz} + \rho\delta\frac{dv}{dz} + \rho v\frac{d\delta}{dz} = E. \quad \text{(A1)}$$

Here, $v$ is velocity, $\delta$ is the fissure diameter, $\rho$ is the plume density, $z$ is the vertical distance (measured from the ocean surface), and $E$ is the mass flux of vapor from the ice walls to the plume vapor (so that $E < 0$ corresponds to condensation onto the ice walls), in units of kg $m^{-2}$ $s^{-1}$. Conservation of momentum is expressed through

$$\rho v\delta\frac{dv}{dz} = -\delta\frac{dp}{dz} - \tau - \rho g\delta - vE^*. \quad \text{(A2)}$$

Here, $p$ is the partial pressure of the plume water vapor, $\tau$ is the stress from the ice walls ($= 12\eta v/\delta + 2C_d\rho v^2$, where $\eta$ is the dynamic viscosity and $C_d$ is the drag coefficient), $g$ is the gravitational acceleration ($= 0.11$ m $s^{-2}$), and $E^*$ is effectively

a mass flux of sublimation from the ice walls ($E^* = E$ when $E > 0$, and $E^* = 0$ when $E < 0$).

Conservation of energy is expressed through

$$\rho v\delta\left(C_v\frac{dT}{dz} - L\frac{ds}{dz}\right) + p\delta\frac{dv}{dz} = -pv\frac{d\delta}{dz} + \frac{p}{\rho}E + v\tau + \frac{1}{2}v^2E^* + L_H sE - \frac{\tau}{v}C_p\Delta T. \quad \text{(A3)}$$

Here, $C_v$ is the specific heat at constant volume, $T$ is the temperature of the plume vapor, $L_H$ is the latent heat of fusion, $s$ is the solid mass fraction (i.e., the fractional contribution to plume mass from solid ice grains), $C_v$ is the specific heat at constant pressure, and $\Delta T(= T - T_w)$ is the temperature difference between the vapor and the ice walls. For simplicity, we take $s$ to be zero because we are more concerned with the dynamics of gases in the plume, and the mass fraction of ice grains does not significantly affect condensation, vapor pressures in the plume, or erupted mass fluxes (Nakajima & Ingersoll 2016).

The mass flux between the conduit walls and the plume, $E$, is defined by

$$E = -2\left(\frac{p}{\sqrt{2\pi RT/M}} - \frac{p_w}{\sqrt{2\pi RT_w/M}}\right). \quad \text{(A4)}$$

Here, $R$ is the universal gas constant, $M$ is the molar mass of water, and $p_w$ is the temperature-dependent saturation vapor pressure over ice, defined by Equation (4).

We adopt Nakajima and Ingersoll's (2016) assumption that the latent heat flux onto the walls due to condensation is (at least partially) responsible for the elevated heat fluxes observed near the tiger stripe fissures, and that the heat flux onto the walls due to condensation ($F_s$) is equal to the heat flux conducted through the ice ($F_c$) and to the heat flux radiated from the surface ($F_r$). This is expressed through

$$F_s(d) = F_c(d) = F_r(d). \quad \text{(A5)}$$

Here, $d$ refers to depth ($= D - z$, where $D$ is the full fissure depth) such that $d = 0$ at the fissure outlet. In the context of the radiated heat flux at the surface ($F_r$), $d$ refers to a horizontal distance away from the fissure, again such that $d = 0$ at the fissure outlet. Heat due to condensation is found by

$$F_s(d) = -2E(d)L_H. \quad \text{(A6)}$$

The conducted heat flux is approximated by

$$F_c(d) = 4k\frac{T_s(d) - T_w(d)}{\pi d}. \quad \text{(A7)}$$

Here, $k$ is the thermal conductivity of ice, and $T_s(d)$ is the surface temperature at horizontal distance $d$ away from the fissure. The radiated heat flux is found by

$$F_r(d) = 2\sigma(T_s^4(d) - T_e^4). \quad \text{(A8)}$$

Here, $\sigma$ is the Stefan–Boltzmann constant, and $T_e$ is the effective temperature of the ice (≈68 K).

To initialize the model, we begin by guessing a value for the pressure at the base of the fissure, $p_0$, just above the ocean surface. Assuming a vapor temperature at the base of the fissure, $T_0$, that is equal to the temperature of the liquid (≈273 K) enables us to find the density of the vapor $\rho_0$ via the ideal gas law. Using Equation (5), which describes the evaporation rate from water, we are able to find the plume velocity at the base of the fissure, $v_0$. In general, we then use Equations (A1), (A2), and (A3), along with Equation (2), the ideal gas law, and an equation for the internal energy ($du = C_v dT$) to solve for each term $dT/dz$, $du/dz$, $ds/dz$, $d\rho/dz$, $dp/dz$, and $dv/dz$ (six equations and six unknowns). Note that $E$ and $T_w$ are two additional unknowns that appear in the mass, energy, and momentum conservation equations, and we take two different approaches to solve for these, described in the next paragraphs. We then use a finite-difference method to approximate each variable ($T$, $u$, $s$, $\rho$, $p$, and $v$) slightly further up in the fissure conduit (e.g., $T(z_0 + \Delta z) = T_0 + (dT/dz)_0 \times \Delta z$), and repeat until we reach the top of the fissure, where $z = D$. We use the bisection method to iteratively adjust our initial guess for $p_0$ until we reach a solution where the velocity at the fissure outlet is equal to one of our velocity boundary conditions (either the sound speed or the escape velocity).

As in Nakajima & Ingersoll (2016), we take two approaches to modeling the condensation and heat fluxes, and find minimal differences in the results between the two approaches. The first approach is less computationally intensive, and involves a semianalytic solution to Equations (A5), (A6), (A7), and (A8). In this semianalytic approach, we begin by assuming that the temperature of the wall, $T_w$, is constant and equal to 273 K at all vertical distances $z$. We then use a numerical solver to solve Equations (A5), (A6), (A7), and (A8), in particular to find the mass flux between fissure walls and the plume $E(d)$ (or, equivalently, $E(z)$ which is the same array of values in reverse order).

In the second approach, we make no assumptions about the temperature of the wall, and instead find a fully numerical solution to the condensation and heat flux Equations (A4)–(A8). The fully numerical approach necessitates solving the Equations (A4)–(A8) at each finite distance $z_n$, by first finding $T(z_n)$ and then solving (A4)–(A8) for the wall temperature at that depth, $T_w(d_n = D - z_n)$, surface temperature at an equivalent horizontal distance away from the fissure, $T_s(d_n = D - z_n)$, and mass flux between the plume and fissure walls at that depth, $E(d_n = D - z_n)$. With these values calculated, we can proceed to find $dT/dz$, $du/dz$, $ds/dz$, $d\rho/dz$, $dp/dz$, and $dv/dz$, as before, and again use the finite-difference method to find $T$, $u$, $s$, $\rho$, $p$, and $v$ all the way up the fissure.

## Appendix B
## Activity Coefficients from Pitzer Parameters

To calculate activity coefficients for dissolved ionic species we use the Pitzer equations, which are appropriate for ionic strengths $I > 0.5$ molal (Marion & Kargel 2008). Ionic strength may be calculated via

$$I = \frac{1}{2}\sum_i m_i z_i^2. \quad \text{(B1)}$$

Here, $m_i$ and $z_i$ are the molality and charge of ionic species $i$.

The activity coefficients are determined from Pitzer parameters that are specific to binary and ternary interactions between aqueous ionic and neutral species. For simplicity, we ignore the effects of ternary interactions and any neutral–ion and neutral–neutral interactions, assuming activity coefficients of the neutral species $NH_3$(aq) and $CO_2$(aq) as equal to 1. Ternary interactions can be discounted at ionic strengths <3.5 molal (Langmuir 1997), and we generally predict ionic

strengths around 1 molal. Neutral–ion interactions are only relevant at particularly high concentrations of neutral species (Marion & Kargel 2008). Marion et al. (2012) have also previously estimated the activity coefficient for ammonia at low temperatures (~273 K) to be ≈1. We also ignore cation–cation and anion–anion interactions because the parameters describing these interactions are not widely reported, and in particular are unavailable for $NH_4^+$ (Marion et al. 2012).

The following equations and notation for the calculation of Pitzer parameters are adopted from Krissansen-Totton et al. (2018b), who used the same simplifications as the Pitzer model described in the previous paragraph, and from Marion & Kargel (2008), where the full versions of all equations can be found.

Activity coefficients for cations ($M$) and anions ($X$) are found via

$$\ln(\gamma_M) = z_M^2 F + \sum_{\text{all anions}} m_a(2B_{Ma} + ZC_{Ma}), \tag{B2}$$

$$\ln(\gamma_X) = z_X^2 F + \sum_{\text{all cations}} m_c(2B_{cX} + ZC_{cX}). \tag{B3}$$

Here,

$$F = -A_\phi\left[\frac{I^{0.5}}{1 + bI^{0.5}} + \frac{2}{b}\ln(1 + bI^{0.5})\right] + \sum_{\text{all pairs}} m_a m_c B'_{ca}, \tag{B4}$$

$$Z = \sum_i m_i|z_i|, \tag{B5}$$

$$B_{MX} = B_{MX}^{(0)} + B_{MX}^{(1)} f(\alpha_1 I^{1/2}) + B_{MX}^{(2)} f(\alpha_2 I^{1/2}), \tag{B6}$$

$$f(x) = \frac{2[1 - (1 + x)\exp(-x)]}{x^2}, \tag{B7}$$

$$B'_{MX} = \frac{B_{MX}^{(1)} f'(\alpha_1 I^{1/2})}{I} + \frac{B_{MX}^{(2)} f'(\alpha_2 I^{1/2})}{I}, \tag{B8}$$

$$f'(x) = \frac{-2[1 - (1 + x + x^2/2)\exp(-x)}{x^2}, \tag{B9}$$

$$C_{MX} = \frac{C_{MX}^\phi}{2\,|z_M z_X|^{1/2}}. \tag{B10}$$

In the above equations, the subscripts $c$ and $a$ refer to cations and anions, respectively. As in Equation (B1), $m$ refers to molality and $z$ refers to charge. In Equations (B2) and (B3), the $B$ and $C$ terms are Pitzer parameters that account for specific cation–anion interactions, and they are derived from Equations (B6) and (B10), respectively. In Equation (B4), $A_\Phi = 0.3915\,\text{kg}^{0.5}\,\text{mol}^{-0.5}$ and $b = 1.2\,\text{kg}^{0.5}\,\text{mol}^{-0.5}$ are constants. In Equations (B6) and (B8), $\alpha_1$ and $\alpha_2$ are constants. In the case of all binary systems except 2:2 electrolytes, $\alpha_1 = 1.4\,\text{kg}^{0.5}\text{mol}^{-0.5}$ and $\alpha_2 = 0\,\text{kg}^{0.5}\text{mol}^{-0.5}$. Because all ion–ion pairs considered here fall under this category (most are 1:1, except for pairs involving $CO_3^{2-}$, which are 1:2), $\alpha_2 = 0\,\text{kg}^{0.5}\text{mol}^{-0.5}$, which allows us to ignore the third term in Equation (B6) and the second term in (B8). The Pitzer parameters $B^{(0)}$, $B^{(1)}$, and $C^\Phi$ are reported in Marion & Kargel (2008) and Marion et al. (2012), and set to 0 where unavailable.

The activity of water, $a_w$, is calculated from

$$a_w = \exp\left(\frac{-\phi\sum_i m_i}{55.50844}\right). \tag{B11}$$

Here, $\phi$ is the osmotic coefficient, given from

$$(\phi - 1) = \frac{2}{\sum_i m_i}\left[\frac{-A_\phi I^{3/2}}{1 + bI^{1/2}} + \sum_{\text{all pairs}} m_c m_a (B_{ca}^\phi + ZC_{ca})\right]. \tag{B12}$$

## Appendix C
## Solvation Energies of Ions

While dissolved ions such as $Na^+$, $Cl^-$ and $NH_4^+$ are included in our aqueous chemistry model (Section 2.4), we do not include them in our exsolution models (Section 2.3) due to their high energies of solvation. For example, $NH_4^+$ has a solvation energy ($W_{sol}$, the energy difference between the gas phase and dissolved phase) of $-88.2$ kcal mol$^{-1}$ ($-3.69 \times 10^{-5}$ J mol$^{-1}$, $-6.13 \times 10^{-19}$ J molecule$^{-1}$; Meot-Ner 1987). We can find a ratio of the number densities of $NH_4^+$ in the vapor phase versus the dissolved phase (Postberg et al. 2009, Supplementary Material) via

$$\frac{n_v}{n_l} \simeq n_l \exp\left(\frac{W_{sol}}{k_B T}\right). \tag{C1}$$

Here, $n_v$ is the number density of a solute (e.g., $NH_4^+$) in the vapor phase, $n_l$ is the number density of the solute in the liquid, $W_{sol}$ is the solvation energy (here in units of J molecule$^{-1}$), $k_B$ is the Boltzmann constant (here in units of J K$^{-1}$), and $T$ is the temperature (taken to be 273.15 K). For $NH_4^+$, we find this ratio to be on the order of $10^{-70}$. For context, the same ratio $n_v/n_l$ for $NH_3$ is much greater, $\sim 2 \times 10^{-3}$ at 273 K. The equation to calculate this ratio for $NH_3$ or other gases with known Henry's law constants is

$$\frac{n_v}{n_l} = \frac{1}{\alpha} = \frac{M_{H_2O}}{HRT\rho_l}. \tag{C2}$$

Here, $\alpha$ is the Bunsen coefficient (a dimensionless version of the Henry's law constant; Sander 2015), $M_{H_2}O$ is the molar mass of water, $H$ is the Henry's law constant in units of Pa$^{-1}$, $R$ is the gas constant, $T$ is the temperature, and $\rho_l$ is the density of water.

## ORCID iDs

Lucas M. Fifer https://orcid.org/0000-0003-0373-9110
David C. Catling https://orcid.org/0000-0001-5646-120X
Jonathan D. Toner https://orcid.org/0000-0003-1681-6189

## References

Affholder, A., Guyot, F., Sauterey, B., Ferrière, R., & Mazevet, S. 2021, NatAs, 5, 805
Bandura, A. V., & Lvov, S. N. 2006, JPCRD, 35, 15
Bapteste, É, Brochier, C., & Boucher, Y. 2005, Archaea, 1, 859728
Bates, R. G., & Pinching, G. D. 1949, J. Res. Natl. Bur. Stand., 42, 419
Bouquet, A., Glein, C. R., & Waite, J. H. 2019, ApJ, 873, 28
Bradley, A. S. 2016, PNAS, 113, 13944
Brandes, J. A., Boctor, N. Z., Cody, G. D., et al. 1998, Natur, 395, 365
Broecker, W. S., & Peng, T.-H. 1982, Tracers in the Sea (Palisades, NY: Lamont-Doherty Geological Observatory of Columbia Univ.), https://www.ldeo.columbia.edu/~broecker/Home_files/TracersInTheSea_searchable.pdf
Cable, M. L., Porco, C., Glein, C. R., et al. 2021, PSJ, 2, 132
Carrozzo, F. G., De Sanctis, M. C., Raponi, A., et al. 2018, SciA, 4, 1
Choblet, G., Tobie, G., Sotin, C., et al. 2017, NatAs, 1, 841

Cussler, E. L. 2009, Diffusion: Mass Transfer in Fluid Systems (3rd ed.; Cambridge: Cambridge Univ. Press)
De Sanctis, M. C., Raponi, A., Ammannito, E., et al. 2016, Natur, 536, 54
Fierer, N., & Jackson, R. B. 2006, PNAS, 103, 626
Fitzgerald, J. W. 1991, AtmEB, 25, 533
Frössling, N. 1938, Gerlands Beiträge Geophys, 52, 170
Glein, C. R., Baross, J. A., & Waite, J. H. 2015, GeCoA, 162, 202
Glein, C. R., & Waite, J. H. 2020, GeoRL, 47, e85885
Goguen, J. D., Buratti, B. J., Brown, R. H., et al. 2013, Icar, 226, 1128
Hall, A. 1989, GeocJ, 23, 19
Hansen, C. J., Shemansky, D. E., Esposito, L. W., et al. 2011, GeoRL, 38, L11202
Hansen, C. J., Esposito, L. W., Aye, K.-M., et al. 2017, GeoRL, 44, 672
Hansen, C. J., Esposito, L. W., Colwell, J. E., et al. 2020, Icar, 344, 113461
Hedman, M. M., Dhingra, D., Nicholson, P. D., et al. 2018, Icar, 305, 123
Hemingway, D. J., Rudolph, M. L., & Manga, M. 2019, NatAs, 4, 234
Higbie, R. 1935, Transactions of the AIChE, 31, 365
Higgins, P. M., Glein, C. R., & Cockell, C. S. 2021, JGRE, 126, e06951
Hoch, M. P., Fogel, M. L., & Kirchman, D. L. 1992, LimOc, 37, 1447
Hoehler, T. M. 2022, NatAs, 6, 4
Hsu, H. W., Postberg, F., Sekine, Y., et al. 2015, Natur, 519, 207
Ingersoll, A. P., & Pankine, A. A. 2010, Icar, 206, 594
Ingersoll, A. P., & Nakajima, M. 2016, Icar, 272, 319
Jayaweera, G. R., & Mikkelsen, D. S. 1990, SSASJ, 54, 1447
Jayaweera, G. R., Paw, K. T. U., & Mikkelsen, D. S. 1990, SSASJ, 54, 1462
Jones, S. F., Evans, G. M., & Galvin, K. P. 1999, AdCIS, 80, 27
Keller, M., & Zengler, K. 2004, Nature Reviews Microbiology, 2, 141
Kempf, S., Srama, R., Postberg, F., et al. 2005, Sci, 307, 1274
Kempf, S., Beckmann, U., & Schmidt, J. 2010, Icar, 206, 446
Khawaja, N., Postberg, F., Hillier, J., et al. 2019, MNRAS, 489, 5231
Kieffer, S. W., Lu, X., Bethke, C. M., et al. 2006, Sci, 314, 1764
Kite, E. S., & Rubin, A. M. 2016, PNAS, 113, 3972
Kocamustafaogullari, G. 1983, ICHMT, 10, 501
Krissansen-Totton, J., Arney, G. N., & Catling, D. C. 2018a, PNAS, 115, 4105
Krissansen-Totton, J., Olson, S., & Catling, D. C. 2018b, SciA, 4, eaao5747
Landau, L. D., & Lifshitz, E. M. 1959, Fluid Mechanics (London: Pergamon), 364
Langmuir, D. 1997, Aqueous Environmental Geochemistry (Upper Saddle River, New Jersey: Prentice Hall)
Liger-Belair, G. 2012, EPJST, 201, 1
MacKenzie, S. M., Neveu, M., Davila, A. F., et al. 2021, PSJ, 2, 77
Magee, B. A., & Waite, J. H. 2017, LPSC, 48, 2974
Marion, G. M., & Kargel, J. S. 2008, Cold Aqueous Planetary Geochemistry with FREZCHEM. Advances in Astrobiology and Biogeophysics (Berlin: Springer)
Marion, G. M., Kargel, J. S., Catling, D. C., & Lunine, J. I. 2012, Icar, 220, 932
Matson, D. L., Castillo, J. C., Lunine, J., & Johnson, T. V. 2007, Icar, 187, 569
McCollom, T. M. 2016, PNAS, 113, 13965
McCollom, T. M., & Seewald, J. S. 2006, E&PSL, 243, 74
McKay, C. P., Porco, C. C., Altheide, T., Davis, W. L., & Kral, T. A. 2008, AsBio, 8, 909
McKinnon, W. B. 2012, LPI Contribution, 1667, 6475
McKinnon, W. B., Lunine, J. I., Mousis, O., Waite, J. H., & Zolotov, M. Y. 2018, in Enceladus and the Icy Moons of Saturn, ed. P. M. Schenk et al. (Tucson, AZ: Univ. Arizona Press), 17
Meot-Ner, M. 1987, JPhCh, 91, 417
Millero, F. J., Pierrot, D., Lee, K., et al. 2002, DSRI, 49, 1705
Montes, F., Rotz, C. A., & Chaoui, H. 2009, Transactions of the ASABE, 52, 1707
Mumma, M. J., & Charnley, S. B. 2011, ARA&A, 49, 471
Murphy, D. M., & Koop, T. 2005, QJRMS, 131, 1539
Nakajima, M., & Ingersoll, A. P. 2016, Icar, 272, 309
Nimmo, F., Spencer, J. R., Pappalardo, R. T., & Mullen, M. E. 2007, Natur, 447, 289
Nock, W. J., Heaven, S., & Banks, C. J. 2016, ChEnS, 140, 171
Park, S. H., Park, C., Lee, J. Y., & Lee, B. 2017, Nucl. Eng. Technol., 49, 692
Perrin, C. L., & Engler, R. E. 1991, JPhCh, 95, 8431
Persad, A. H., & Ward, C. A. 2016, ChRv, 116, 7727
Porco, C. C., Helfenstein, P., Thomas, P. C., et al. 2006, Sci, 311, 1393
Postberg, F., Kempf, S., Schmidt, J., et al. 2009, Natur, 459, 1098
Postberg, F., Khawaja, N., Abel, B., et al. 2018, Natur, 558, 564
Postberg, F., Schmidt, J., Hillier, J., Kempf, S., & Srama, R. 2011, Natur, 474, 620
Rayleigh, L. 1917, The London, Edinburgh, and Dublin Philosophical Magazine and Journal of Science, 34, 94
Reeves, E. P., & Fiebig, J. 2020, Elements, 16, 25
Reh, K., Spilker, L., Lunine, J. I., et al. 2016, in 2016 IEEE Aerospace Conf. (Piscataway, NJ: IEEE), 1
Sander, R. 2015, ACP, 15, 4399
Schmidt, J., Brilliantov, N., Spahn, F., & Kempf, S. 2008, Natur, 451, 685
Sekine, Y., Shibuya, T., Postberg, F., et al. 2015, NatCo, 6, 8604
Spencer, J. R., Nimmo, F., Ingersoll, A. P., et al. 2018, in Enceladus and the Icy Moons of Saturn, ed. P. M. Schenk et al. (Tucson, AZ: Univ. Arizona Press), 163
Taubner, R. S., Pappenreiter, P., Zwicker, J., et al. 2018, NatCo, 9, 748
Teolis, B. D., Perry, M. E., Hansen, C. J., et al. 2017, AsBio, 17, 926
Thomas, P. C., Tajeddine, R., Tiscareno, M. S., et al. 2016, Icar, 264, 37
Vu, T. H., Hodyss, R., Johnson, P. V., & Choukroun, M. 2017, P&SS, 141, 73
Waite, J. H., Combi, M. R., Ip, W.-H., et al. 2006, Sci, 1419, 1419
Waite, J. H., Glein, C. R., Perryman, R. S., et al. 2017, Sci, 356, 155
Waite, J. H., Lewis, W. S., Magee, B. A., et al. 2009, Natur, 460, 487

# Chapter 3: Experimental Investigation of Gas Exsolution under Enceladus Plume Conditions

Lucas M. Fifer[1,2], Kendall Ford[3], Benjamin Mousseau[4], Fabian Klenner[1,2], Jonathan D. Toner[1], David C. Catling[1,2]

*[1]Department of Earth & Space Sciences, University of Washington, Seattle, WA; [2]Astrobiology Program, University of Washington, Seattle, WA; [3]Macalester College, Saint Paul, MN; [4]Yale University, New Haven, CT.*

**Abstract**

Enceladus's erupting plume delivers gases and ice grains from a subsurface ocean to space, where they are readily measurable by in situ and remote techniques. The gas composition of the plume provides vital clues to the chemistry, habitability, and active geological processes within the ocean. However, chemical fractionation during eruption can result in large differences between the plume composition and the source ocean. In particular, the exsolution of gases at different rates can cause their enrichment or depletion in the plume depending on the mass transfer coefficients that describe their exsolution. Mass transfer coefficients for gas-water transfer have been primarily measured and simulated in conditions typical of the terrestrial ocean-atmosphere interface, not at low pressure conditions relevant to Enceladus. In this study, we perform laboratory experiments under the low pressure, low temperature, and mildly saline conditions relevant to plume formation at Enceladus's ocean-gas interface. We find a positive linear correlation between the stir rate in solution and the mass transfer coefficient, and a negligible difference between mass transfer from pure water versus a 0.2 molal NaCl solution, consistent with prior experimental work. We also find mass transfer coefficients (piston velocities) for $CO_2$ of 1–2 x $10^{-5}$ m $s^{-1}$, which is comparable to measurements under terrestrial atmospheric conditions. For $N_2$, we find mass transfer coefficients that are an order of magnitude higher than $CO_2$ and theoretical predictions. These

results suggest that sparingly soluble gases like $N_2$ and $H_2$ may experience enhanced exsolution under low pressure conditions, potentially due to bubble-mediated mass transfer. That insoluble gases exsolve more readily than previously assumed implies a lower minimum concentration in Enceladus's ocean compared to previous estimates.

## 1. Introduction

The erupting plume of Enceladus provides insight into chemical conditions and active processes within the subsurface ocean. In particular, the gas phase of the plume helps to reveal the aqueous chemistry of the plume source (including master variables like pH), the available nutrients and energy for life, and the occurrence of serpentinization and other water-rock reactions (Fifer et al., 2022; Glein et al., 2018; Glein & Waite, 2020; Higgins et al., 2024; Peter et al., 2023; Waite et al., 2017). However, fractionation of gases during eruption complicates estimating ocean chemistry from plume measurements (Bouquet et al., 2019; Fifer et al., 2022; Glein et al., 2015; Glein & Waite, 2020). In particular, the differential rates at which gases exsolve from the ocean will cause relative enrichment in the plume of rapidly exsolving gases (Fifer et al., 2022). Therefore, quantifying the exsolution rates of gases under Enceladus plume conditions is crucial to our understanding of the plume as a proxy for ocean composition.

The majority of previous research on water-gas mass transfer is on dissolution in the context of ocean-atmosphere exchange on Earth. This work includes theoretical, experimental, and in situ oceanographic studies (Broecker & Peng, 1982; Carpenter et al., 2012; Gålfalk et al., 2013; Liss & Johnson, 2014; Liss & Slater, 1974; Merlivat & Memery, 1983; Woolf et al., 2007; Yang et al., 2021). Many of these studies focus on the role of wind speed and breaking waves on the enhancement of mass transfer, as wave-generated bubbles increase the effective surface area for atmospheric gases to dissolve into the ocean (Carpenter et al., 2012; Merlivat & Memery, 1983;

Yang et al., 2021). Other experimental work on gas dissolution centers on the supply of gases to solution for growing microbial cultures, or powering industrial bioreactors (Aroniada et al., 2020; Karimi et al., 2013; Nishimura et al., 1991).

Prior studies focused on *exsolution* of gases tend to focus on very specific chemical environments. For instance, there is a wide body of work on the exsolution of ammonia ($NH_3$) from manures and soils (Montes et al., 2009; Ni, 1999), and an entire sub-field focused on degassing of carbon dioxide from champagne and beer (Liger-Belair, 2012; Liger-Belair & Cilindre, 2021; Lynch & Bamforth, 2002; Shafer & Zare, 1991; Y. Zhang & Xu, 2008). However, regardless of the nature of the source solution, the vast majority of prior gas transfer studies are under terrestrial atmospheric conditions. This motivates our current work to investigate gas exsolution under the low pressure (and low temperature) conditions characteristic of Enceladus and its ocean-plume system.

In this study, we perform laboratory analog experiments of gas exsolution in the Enceladus ocean-plume system. We determine the mass transfer coefficients for $CO_2$ and $N_2$ from aqueous solutions. $CO_2$ is one of the most abundant gases in the Enceladus plume (Peter et al., 2023; Waite et al., 2017), and relating its plume abundance to its oceanic concentration is crucial to determining the pH and ionic speciation in Enceladus's ocean (Fifer et al., 2022; Glein et al., 2015; Glein & Waite, 2020). The detection of $N_2$ in the plume is less certain due to insufficient resolving power of the INMS (Ion and Neutral Mass Spectrometer) to distinguish $N_2$, CO, and $C_2H_4$ (Waite et al., 2009). However, $N_2$ is a useful substitute for other similarly insoluble gases that were measured in the plume such as $H_2$ and $CH_4$, and provides a point of comparison against $CO_2$, which is roughly 50-times more soluble (Sander, 2015). Therefore, experimental determination of $N_2$ exsolution

rates help to constrain the exsolution and oceanic concentrations of sparingly soluble but biologically important gases like $H_2$ and $CH_4$.

We also investigate the possible effect of ocean salinity on gas exsolution. The diffusion coefficient of $CO_2$ tends to decrease with salinity (Belgodere et al., 2015; W. Zhang et al., 2015), so we may expect a similar decrease in the mass transfer rate of exsolution. The salinity of Enceladus's ocean is currently constrained by measurements of ice grains in the plume and E-ring (Postberg et al., 2009, 2011, 2023), though salt concentration and precipitation during ice grain freezing could result in differences between their salinity and the ocean source (Fox-Powell & Cousins, 2021; Klenner et al., 2025). Future electromagnetic and geophysical observations of Enceladus could better constrain the concentration of salts in the ocean (Castillo-Rogez et al., 2022; Vance et al., 2018), so we attempt to answer whether this chemically and astrobiologically important factor also has an influence on the eruption rates of gases.

## 2. Methods

### *2.1. Experimental Apparatus*

The reaction vessel is a sealed, cylindrical, stainless steel chamber with 485 ml internal volume (Figure 1). A line of vacuum-tight stainless steel piping connects the reaction chamber to a gate valve, and then a T-junction that leads to both a turbo molecular vacuum pump, and a compressed gas cylinder. The reaction vessel is also submerged in an ice bath, and placed on top of a magnetic stirrer to enable mixing of both the ice bath and solutions inside the reaction vessel. The ice bath allows us to perform experiments at the temperature conditions at the ocean-plume interface, where contact between the ocean and ice walls should produce a temperature of 273 K.

The rate of stirring of solution within the reaction chamber can be varied, enabling investigation of different mixing rates on gas exsolution.

The primary experimental measurement is the gas pressure in the headspace, acquired by a pressure transducer that is connected the reaction chamber. The pressure transducer has two separate channels: a low pressure channel (1.00–130.00 mbar), and a high pressure channel (1.0–1300.0 mbar). The two pressure channels take measurements nearly simultaneously (within <0.4 s of each other), and the data are sent via a wired connection to an MKS Type 2000 PDR (power supply and digital readout) Dual Capacitance Diaphragm Gauge Controller. Pressures can be monitored directly on the PDR, but are also sent to a computer running LabView. We have a custom LabView interface to record pressure readings from both channels at user-defined sampling intervals. In practice, the shortest possible sampling interval is ~0.8s. We save the pressures and their corresponding sample times as data tables.

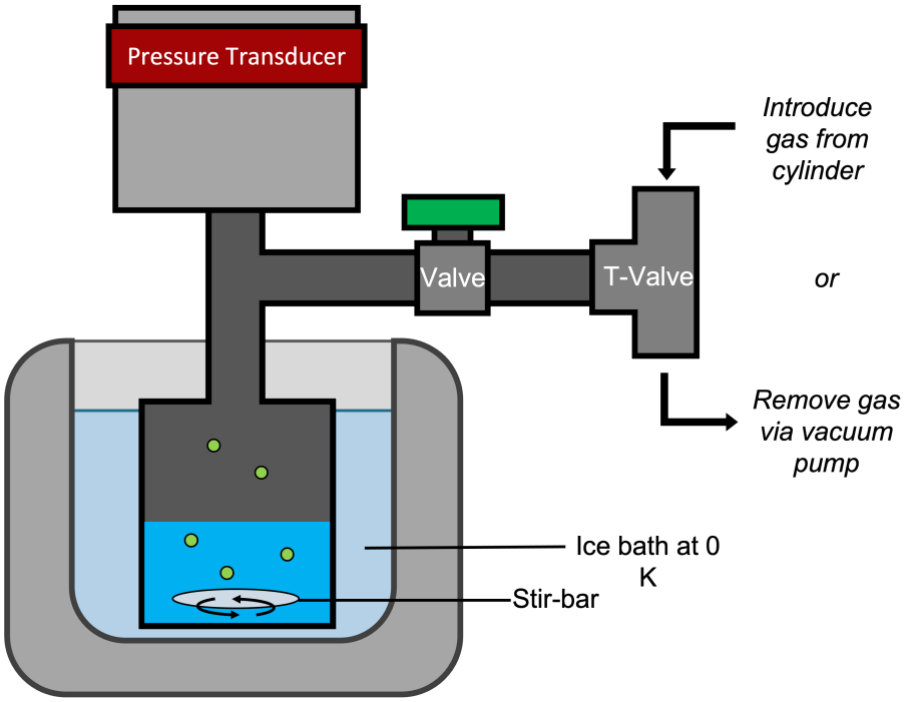


**Figure 1.** The experimental apparatus used to measure gas exsolution. At lower left, the reaction chamber holds the simulated Enceladus ocean solution and a stir bar, and is submerged in a ice bath. At top, the pressure transducer measures the gas pressure in the headspace, and this data is read into LabVIEW and recorded over time. The valves at right enable the system to be opened to a compressed gas cylinder (to add the targeted gas for experiments), or to a vacuum pump (to remove initial atmospheric gases, and later to partially remove the headspace and drive exsolution of the targeted gas).

### *2.2. Experimental Procedure*

We prepared 200 ml solutions for our simulated Enceladus ocean water. The first solution we used was pure deionized water, while the second was a 0.2 molal NaCl solution, representing a salt concentration at the high end of the measured salinity in the Enceladus plume ice grains (0.05–0.2 molal NaCl; Postberg et al. 2009). The prepared solution was added to the reaction chamber along with a magnetic stir bar, the chamber was sealed, and we used the vacuum to

remove most of the atmospheric gas in the headspace. The reaction chamber was then placed in a sonication bath, and we performed three cycles of 15-minutes of sonication (to nucleate gas bubbles and facilitate exsolution) and ~10 seconds of vacuuming to remove residual atmospheric gas from both the solution and headspace. Following the degassing cycles, the reaction chamber was submerged in the ice bath and allowed to cool for ~1 hour. Finally, we used the vacuum again to remove residual water vapor that was supersaturated in the headspace. At this point, the only pressure in the chamber headspace should be the saturation vapor pressure of water at 273 K (~6.11 mbar), and the solution was ready for the introduction of the experimental gas ($CO_2$ or $N_2$).

To introduce a gas into the reaction chamber, we used the connection to a compressed gas cylinder. At this stage, we began recording the pressure readings in LabVIEW at a rapid sampling interval (~0.8s). We briefly opened the gate valve to add the gas, targeting between 600–1000 mbar of headspace pressure. We then closed the valve, and allowed the gas to dissolve to equilibrium for 2-3 hours. Approximately 10 minutes after introduction of the gas, we switched the pressure sampling to a slower interval (30-60 seconds) to keep file sizes efficient. The rapid sampling interval was used to capture short-term changes in the headspace (due to gas introduction or removal), while the slower sampling interval was sufficient to record the slower processes of equilibration over 10s of minutes or several hours. The 6.11 mbar contribution from water vapor was subtracted from the total pressure to find the partial pressure of the non-water gas.

After the gas dissolved to equilibrium, we began measurement of gas exsolution from the aqueous phase. With sampling pressures at the rapid (0.8s) interval, we opened the gate valve again very briefly (<1s), using the vacuum pump to remove ~30% of the headspace pressure. This drove gas exsolution by creating a pressure gradient between the effective pressure in the solution and a lower pressure in the headspace. With the gate valve closed, we allowed the gas to exsolve to a

new equilibrium pressure intermediate between the previous equilibrium pressure and the lowest pressure achieved during gas removal. Again we reverted to the slower sampling interval ~10 minutes after gas removal. We repeated the exsolution process several times, until reaching headspace pressures ~30 mbar. At this point, water vapor constituted a significant fraction (~20%) of the pressure in the headspace, so our measurements targeting the non-water gas were more prone to interference (e.g., from evaporation, or temperature variation inside the chamber or pressure transducer), and we concluded the experiments.

### *2.3. Derivation of Mass Transfer Coefficient from Pressure Data*

To derive the mass transfer coefficient of exsolution, we used the following equation of mass transfer:

$$J = K_P(p^* - p) = K_P \Delta p \quad (1)$$

Here, J is the molar flux (mol $m^{-2}$ $s^{-1}$), $K_p$ is the overall mass transfer coefficient (mol $m^{-2}$ $Pa^{-1}$ $s^{-1}$), $p^*$ is the effective partial pressure (Pa) of the non-water gas in the liquid, $p$ is the measured partial pressure in the headspace (Pa), and $\Delta p$ is the difference between these pressures. From the ideal gas law, the molar flux (mol $m^{-2}$ $s^{-1}$) was derived from the changing pressure in the headspace as follows:

$$J = \frac{dp}{dt}\frac{V_{gas}}{RTA} \quad (2)$$

Here, $dp/dt$ is the time-derivative of the headspace pressure (Pa $s^{-1}$), $V_{gas}$ is the volume in the headspace ($m^3$), R is the gas constant (8.314 J $mol^{-1}$ $K^{-1}$), $T$ is the temperature (~273 K), and $A$ is the surface area of the solution (5.34 x $10^{-3}$ $m^2$).

We determined the effective pressure in the solution (a time-dependent variable), $p^*$, based on mass balance. The total moles of gas ($CO_2$ or $N_2$) in the reaction chamber following gas removal was determined from a sum of the moles in the headspace and the moles in solution:

$$n_{total} = n_{e,gas} + n_{e,soln} \tag{3}$$

Here, the subscript *e* refers to the scalar quantity at the final equilibrium point at the end of the exsolution experiment. We reframed the molar quantities above in terms of the measured partial pressure using the ideal gas law and Henry's law:

$$n_{total} = p_e \left( \frac{V_{gas}}{RT} + H_{cp} V_{soln} \right) \tag{4}$$

Here, $p_e$ is the partial pressure in the headspace at the end of the experiment, $H_{cp}$ is the Henry's law solubility constant of the gas (mol $m^{-3}$ $Pa^{-1}$) and $V_{soln}$ is the volume of the solution ($m^3$). Since $p_e$ is measured, and all other variables in the above equation are known, $n_{total}$ could be determined.

Knowing $n_{total}$, we solved for the time-dependent moles of gas in solution again using mass balance:

$$n_{total} = n_{gas}(t) + n_{soln}(t) \tag{5}$$

We again reframed in terms of partial pressures using the ideal gas law and Henry's law, and rearranged to find $p^*$:

$$n_{total} = p(t) \frac{V_{gas}}{RT} + p^*(t) H_{cp} V_{soln} \tag{6}$$

$$p^*(t) = \frac{\left( n_{total} - p(t) \frac{V_{gas}}{RT} \right)}{H_{cp} V_{soln}} \tag{7}$$

Here, $p(t)$ is the recorded partial pressure in the headspace, $p^*(t)$ is the derived effective pressure in solution, and both are time-dependent.

Finally, we subtracted the two pressure terms to find the time-dependent effective pressure difference ($\Delta p$) across the liquid-gas interface, as described in equation (1). Knowing both $\Delta p$ and $J$ (from equation (2)), we found a linear fit for their relationship. The resulting slope is $K_P$, the overall mass-transfer coefficient from equation (1). We compared our experimentally derived $K_P$ to the predictions of a thin-film model:

$$K_P \approx k_x H_{xp} = k_L c_{H2O} H_{xp} = \frac{D_L c_{H2O} H_{xp}}{\Delta} \quad (8)$$

Here, $k_x$ is the liquid-sided mass transfer coefficient (mol $m^{-2}$ $s^{-1}$), $H_{xp}$ is the Henry's law coefficient (here in units of $Pa^{-1}$), $k_L$ is another liquid-sided mass transfer coefficient, often referred to as the piston velocity or transfer velocity (m $s^{-1}$), $c_{H2O}$ is the molar concentration of water (5.55 x $10^4$ mol $m^{-3}$), $D_L$ is the diffusion coefficient for the gas in water ($m^2$ $s^{-1}$), and $\Delta$ is the thin film thickness (m). Thin film thicknesses typical of terrestrial ocean-atmosphere exchange are on the order of 40-100 μm (Broecker & Peng, 1982; Cussler, 2009).

## 3. Results

We used the recorded pressure and mass balance (equations 3-7) to determine the effective partial pressure in solution, $p^*$, and the partial pressure difference across the liquid-gas interface, $\Delta p$ (Figure 2). We found that the $CO_2$ experiments take much longer to equilibrate (~2 hours) compared to $N_2$ (~8 minutes), consistent with $CO_2$'s greater solubility. Determining the effective pressure difference across the liquid-gas interface in the $N_2$ experiments was more difficult than for $CO_2$, because only a small fraction (~1.5%) of the total moles of $N_2$ are present in solution at equilibrium. As a result, the mass balance calculation (equation 7) to find the effective pressure of $N_2$ in solution, $p^*(t)$, was highly sensitive to small variations in the headspace pressure, $p$(t). This was not the case for $CO_2$, where ~50.7% of the total moles of $CO_2$ are in solution at equilibrium.

We subsampled our timeseries for $N_2$ (10s sampling interval) to minimize the effect of noise in the recorded $p(t)$, which significantly affects both $\Delta p$ and $dp/dt$ (Figure 2). Due to $N_2$'s rapid rate of exsolution and the limitations of the pressure transducer's sampling rate, our measurements were also less sensitive to the earliest moments of degassing when $\Delta p$ and $dp/dt$ are greatest.

We converted the time-derivative of pressure to a molar flux (equation 2) and found the linear relationship between the molar flux, $J$, and the effective pressure difference, $\Delta p$. This linear relationship yielded the overall mass transfer coefficient $K_P$. $K_P$ depends on the solubility of the gas (equation 8), so we converted $K_P$ to the liquid-sided mass transfer coefficient $k_L$ (which is independent of solubility) for ease of comparison between gases. $CO_2$ and $N_2$ have comparable diffusion coefficients ($D_{L,CO2}$=7.3 x $10^{-10}$ $m^2$ $s^{-1}$, $D_{L,N2}$=4.9 x $10^{-10}$ $m^2$ $s^{-1}$ at 273 K), so their $k_L$ should be proportionately comparable.

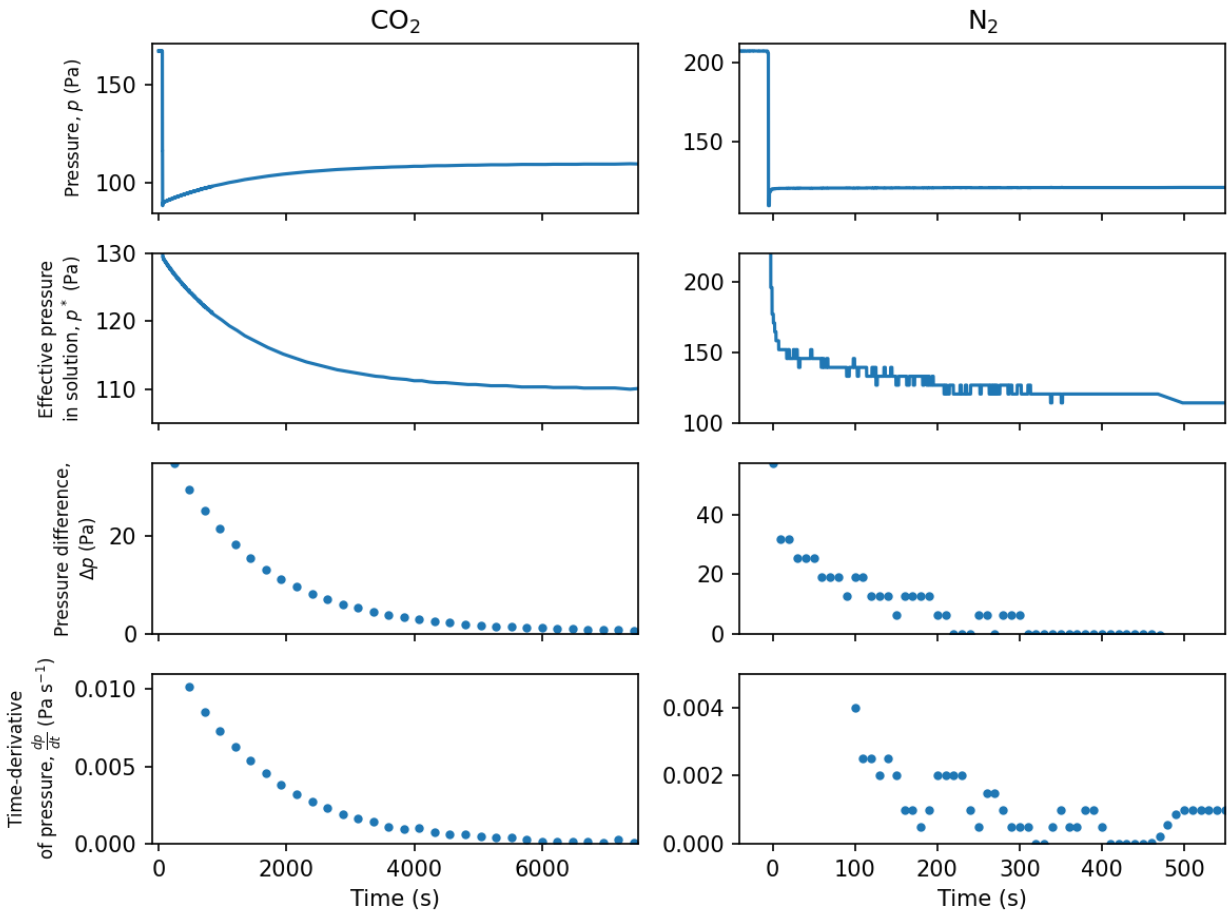


**Figure 2.** Key variables plotted over time from two example exsolution experiments ($CO_2$ on the left, $N_2$ on the right). The headspace pressure (top row) is recorded using the pressure transducer, while all other variables are derived (see equations 2-7). The pressure difference and time-derivative of pressure (bottom two rows) are subsampled relative to the original sampling rate to reduce noise (120s interval for $CO_2$, 10s for $N_2$). For $N_2$, a moving average (100s window) is also applied to the time-derivative of pressure (bottom row) for smoothing.

In Figures 3 and 4, we show the derived mass transfer coefficients for the $CO_2$ and $N_2$ exsolution experiments as a function of stir rate in the reaction chamber. The magnet driving the stir bars is visible, so we determined stir rates by recording short (~10s) videos of the spinning magnet at a high frame rate and counting the rotations. The plotted error in stir rate was determined either by the standard error (for multiple videos within a given experiment) or assuming an observation error of 0.25 rotations (for a single video within a given experiment). The numbered

dial on the magnetic stirrer was not a reliable determination of stir rate because the dial number is proportional to the power supplied to the spinning magnet, but the actual stir rate depended on the distance between the driving magnet and the stir bar in the chamber (which varied slightly between experiments).

Figure 3 shows the experimental results for $CO_2$ exsolution from both pure water and a 0.2 molal NaCl solution. We found a linear relationship ($R^2$=0.48) between stir rate and the mass transfer coefficient (from pure water). Two outliers with anomalously low mass transfer coefficients ($k_L < 1 \times 10^{-5}$ m $s^{-1}$) appeared at stir rate > 5.0 rotations/second, and were excluded from Figure 3 and the linear fit. These two experiments very likely suffered from the stir bar decoupling from the driving magnet, resulting in a lower rate of mixing. The individual measurements of the magnet's spin rate during those two experiments showed a steady acceleration, which tended to occur whenever the stir bar decoupled, and which we did not observe in any of the other experiments. The mass transfer coefficients and corresponding thin film thicknesses (from equation 8) were very consistent with canonical values for terrestrial-ocean atmosphere exchange, 40-100 μm (Broecker & Peng, 1982; Cussler, 2009). Notably, the presence of 0.2 molal NaCl in solution did not affect the rate of exsolution, within uncertainties.

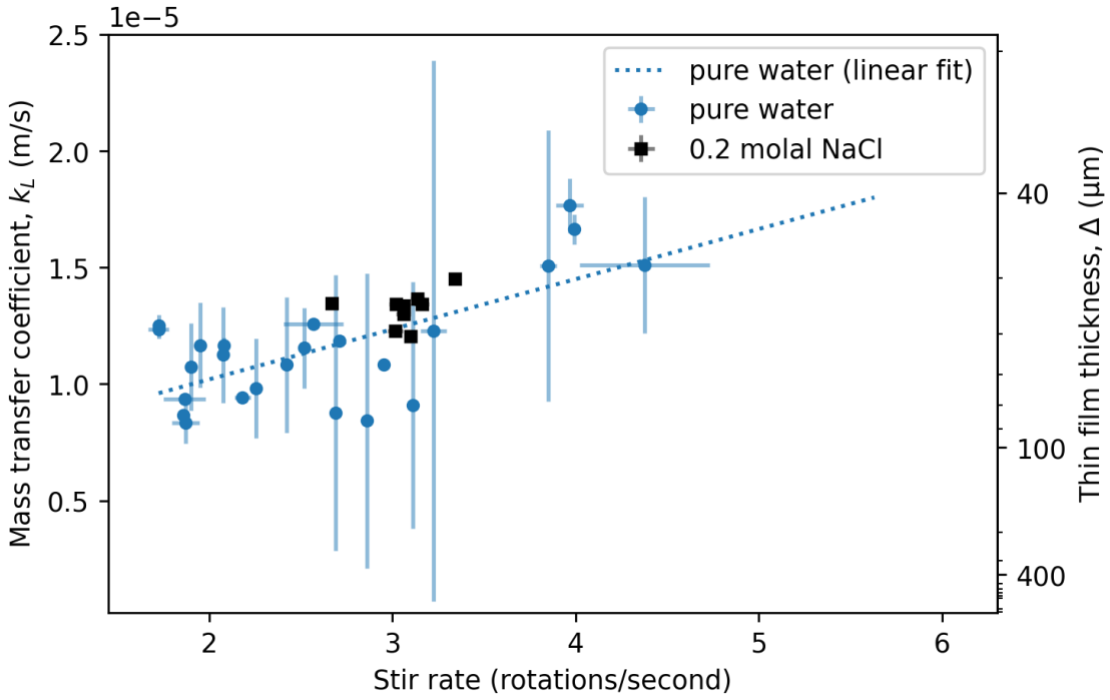


**Figure 3.** Mass transfer coefficient (or piston velocity) for $CO_2$ from two different solutions (pure water and saline), plotted as a function of the stir rate in the liquid. The derived thin film thickness (see equation 8) is shown on the right y-axis. The derived thin film thickness is consistent with literature values for terrestrial ocean-atmosphere exchange, 40-100 μm. The presence of NaCl has a negligible effect on $CO_2$ exsolution rates.

We also found a weak positive correlation between mass transfer coefficient and stir rate for $N_2$ exsolution (Figure 4). We were able to attain stir rates > 5 rotations/second in these experiments by reducing the distance between the magnetic stirrer and stir bar, reducing chances for decoupling. Based on the linear fits, stir rate appeared to have a stronger effect on exsolution in the pure water case compared to the saline solution. However, this was likely due to experimental error rather than a physical effect, given the wide scatter in mass transfer coefficients from 0.2 molal NaCl and the lack of a fit ($R^2$ =0.09) compared to pure water ($R^2$=0.43). The important point is that across almost all $N_2$ experiments, the derived thin film thicknesses were ~1

order of magnitude lower than expected from the literature (and lower than our results for $CO_2$), and the inferred piston velocities ranged from ~5 x $10^{-5}$ to 6 x $10^{-4}$ m $s^{-1}$.

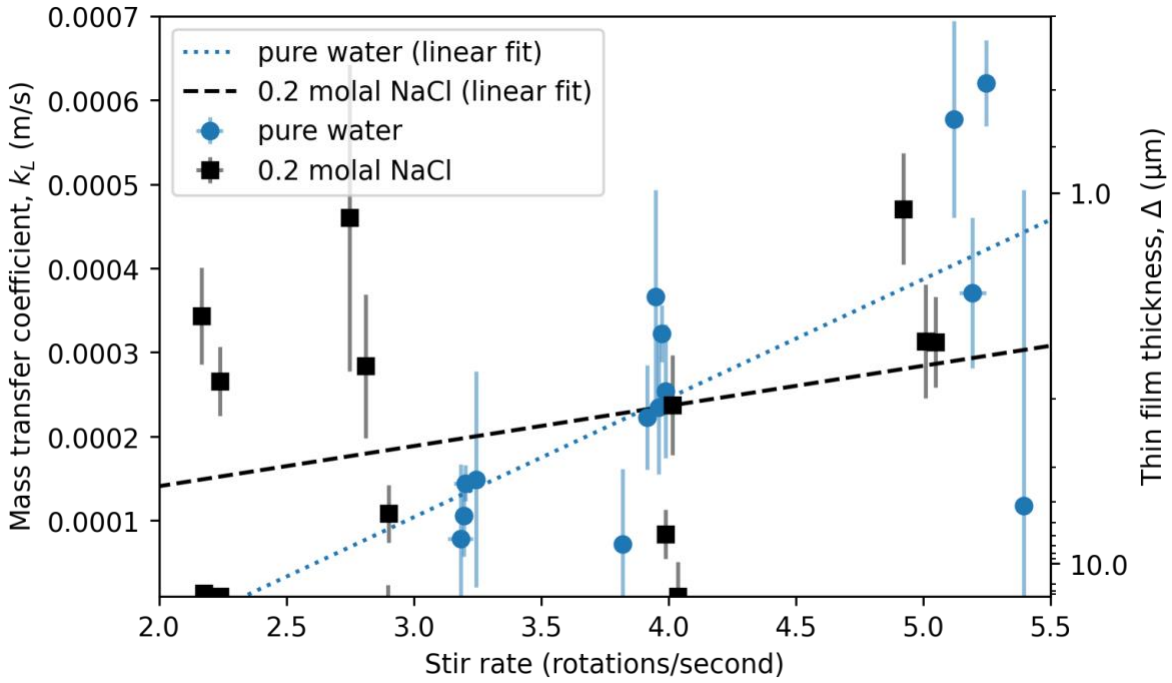


**Figure 4.** Mass transfer coefficient (or piston velocity) for $N_2$ from two different solutions (pure water and saline), plotted as a function of the stir rate in the liquid. The derived thin film thickness (see equation 8) is shown on the right y-axis. Linear fits are shown in the dotted blue line (for pure water) and the dashed black line (for 0.2 molal NaCl). The derived thin film thickness is lower by ~1 order of magnitude than for $CO_2$, and theoretical expectations, indicating faster exsolution rates that may have been enhanced due to bubble formation.

## 4. Discussion

The mass transfer coefficients we find for $CO_2$ are very consistent with prior theoretical, experimental, and in situ oceanographic determinations. This prior work has shown that not only $CO_2$, but gases such as $N_2O$, $CH_4$, He, Ar, and dimethyl sulfide (DMS) all share piston velocities on the order of ~1 x $10^{-5}$ to 2 x $10^{-4}$ m $s^{-1}$ (Broecker & Peng, 1982; Carpenter et al., 2012; Gålfalk et al., 2013; Kharecha et al., 2005; Merlivat & Memery, 1983; Woolf et al., 2007). Given the

relevance of this problem to ocean-atmosphere exchange, many prior studies have focused on the positive correlation between wind speed and piston velocity. The mass transfer coefficients we find for $CO_2$ are comparable to oceanographic measurements at low wind speeds, i.e., under relatively quiescent conditions (Carpenter et al., 2012).

On the other hand, the mass transfer coefficients that we find for $N_2$ push the boundaries of gas transfer in terrestrial settings, even under the most turbulent conditions. Higher wind speeds tend to increase rates of gas transfer by producing breaking waves and in turn, bubbles (Broecker & Peng, 1982; Merlivat & Memery, 1983). Only at the highest measured wind speeds (~15 m $s^{-1}$) do piston velocities approach 2 x $10^{-4}$ m $s^{-1}$ (Carpenter et al., 2012). In an experimental study of bubble-mediated gas transfer at terrestrial atmospheric pressure, sparingly soluble gases like He were found to have a maximum piston velocity of ~2 x $10^{-4}$ m $s^{-1}$ (Woolf et al., 2007). $N_2$ has a comparable solubility to He (~1.6-times more soluble (Sander, 2015)), which is within our data range (Figure 4).

Our exsolution data suggest that bubble formation under low pressure conditions may have enhanced the exsolution of $N_2$ (but not $CO_2$). The stainless steel chamber in our experimental setup does not have windows to observe the inside. However, in our initial attempts to recreate the exsolution experiments using a transparent glass reaction chamber, we do not find a large difference between $N_2$ and $CO_2$ in terms of their tendencies to form bubbles. In both cases, when removing comparable amounts of gas as in the stainless steel experiments, we do not observe bubbles forming. Only when we left the chamber open to the vacuum for >5 seconds did bubbles begin to form, and again with no obvious difference in the rate of bubble formation between $N_2$ and $CO_2$. The glass reaction chamber was non-ideal for the exsolution experiments due to (1) low thermal conductivity that can make the internal solution warmer than the ice bath or cooler after

evaporation, and (2) a nonsecure connection that allows some atmospheric air to enter the chamber when below atmospheric pressure. We leave more detailed investigation on the question of bubble formation to future work, for which a modified version of the stainless steel vessel with a transparent window would be ideal.

The linear dependence of mass transfer coefficient on stir rate that we find is consistent with similar linear trends found in prior experimental studies (Karimi et al., 2013; Lee et al., 2015; Nishimura et al., 1991). Experimental determination of oxygen mass transfer in a stirred reactor suggests that mass transfer coefficients may begin to plateau at high stir rates (Karimi et al., 2013), suggesting a physical upper limit to the mass transfer rate, possibly limited by a minimum thickness to the thin film. The issue of magnetic decoupling of the stir bar limits the possibilities of investigating such an upper limit on our present experimental apparatus. At low stir rates, mass transfer coefficients may similarly plateau (Carpenter et al., 2012; Karimi et al., 2013) to a non-zero mass transfer coefficient. We performed some exsolution trials with $CO_2$ in pure water with no stir bar, and found mass transfer coefficients of ~7 x $10^{-7}$ m $s^{-1}$, corresponding to a thin film thickness of ~1 mm (1000 μm).

Our findings have important implications for the gas exsolution rate from Enceladus's ocean. First, the mass transfer coefficients that we measure for $CO_2$ are consistent with theoretical estimations from the thin film model, so we would estimate the same $CO_2$ exsolution rates as in Fifer et al., 2022, and therefore the same concentrations of $CO_2$ in the ocean. On the other hand, the enhanced exsolution for $N_2$ that we measure suggests that sparingly soluble gases like $H_2$ may exsolve more readily than previously estimated. If the enhanced exsolution we measure is *not* bubble-mediated, then we would predict an oceanic concentration of $H_2$ that is ~10-times lower than previous estimates (Fifer et al., 2022), producing a new lower limit of ~1.4 x $10^{-6}$ molal $H_2$.

However, if the enhanced exsolution *is* bubble mediated, then the lower limit can only be as low as the minimum concentration for $H_2$ bubble formation, ~8 x $10^{-6}$ molal (Fifer et al., 2022). Bubble nucleation of one gas (such as $H_2$) would also serve to increase the effective surface area of mass transfer for other gases. Therefore $H_2$ bubbles could enhance the mass transfer of all dissolved gases. We leave the investigation of multi-gas exsolution to future work.

Finally, the negligible effect of NaCl on gas exsolution suggests that uncertainty in the salinity of Enceladus's ocean has little bearing on the exsolution rate of gases into the plume. Our results are consistent with investigations of the salinity-dependent diffusion coefficient for $CO_2$, which found a linear relationship between NaCl concentration and diffusion coefficient that would produce only a ~2% reduction in the diffusion coefficient at 0.2 molal NaCl (Belgodere et al., 2015).

Organic molecules may have a greater effect on mass transfer, as surfactant organic molecules in terrestrial settings can reduce ocean-gas transfer by up to ~50% (Yang et al., 2021). The effects of organics on gas transfer are highly dependent on their composition and concentration, both of which are currently poorly constrained for Enceladus's bulk or near-surface ocean, so we leave an investigation of organic interference on plume gas exsolution to future work.

## 5. Conclusions

In this study, we have experimentally investigated the exsolution of two gases, $CO_2$ and $N_2$, under physical and chemical conditions relevant to the formation of Enceladus's plume. Generally, we find that $CO_2$ exsolution rates under low pressure, low temperature conditions are equally predictable by thin film models that are typically used to describe mass transfer at the terrestrial ocean-atmosphere interface. We find a linear dependence of mass transfer on stir rate,

consistent with prior work, and a negligible effect of salinity on gas exsolution. The exsolution rates we find for $N_2$ are notably ~1 order of magnitude greater than some theoretical predictions and most oceanographic measurements, suggesting a possible enhancement in exsolution due to bubble-mediated gas transfer. While generally our results add confidence to prior estimations of Enceladus's gas content that used the thin film model, our results for $N_2$ suggests that sparingly soluble gases like $H_2$ may experience greater rates of exsolution, and therefore their abundance in the plume may be explainable with lower concentrations in the Enceladus ocean.

# Chapter 4: Enceladus's Chemical Evolution and Missing Methane Explained by Initial Cometary Bulk Composition and Plume Volatile Loss

Lucas M. Fifer[1,2], David C. Catling[1,2], Rachael E. Hamp[3], Fabian Klenner[1,2], Jonathan D. Toner[1]

*[1]Department of Earth & Space Sciences, University of Washington, Seattle, WA; [2]Astrobiology Program, University of Washington, Seattle, WA; [3]AstrobiologyOU, School of Environment, Earth and Ecosystem Sciences, Faculty of Science, Technology, Engineering and Mathematics, The Open University, Milton Keynes, UK.*

This chapter is currently ready for journal submission.

**Abstract**

Measurements and computational models of Enceladus's plume suggest that it derives from a subsurface ocean rich in methane, inorganic carbon, and ammonia/ammonium species. This volatile-rich composition, along with the measured D/H ratio of plume and surface ice, suggests that Enceladus formed from building blocks similar to Jupiter-family comets. However, estimated oceanic concentrations of inorganic carbon are at least one order of magnitude below cometary bulk abundances, and methane is mysteriously missing by at least two orders of magnitude. By modeling the effects of long-term plume eruption on Enceladus's ocean chemistry in reverse, we find that carbon dioxide and ammonia are retained more easily in the ocean than methane due to their aqueous speciation, explaining the relative depletion of methane today. Our model for loss of volatiles in Enceladus's plume shows that inorganic carbon, methane, total ammonium, and D/H

of water can evolve from a comet-like starting point to the modern composition if plume eruption has lasted for ~30-300 Myr.

## 1. Introduction

### *1.1. The ocean-plume connection on Enceladus*

An erupting plume of ice grains and gases at the south pole of Saturn's moon Enceladus (C. C. Porco et al., 2006) provides evidence of a subsurface ocean (Postberg et al., 2008, 2009; Waite et al., 2009), which is likely global (Thomas et al., 2016). The plume composition can be used to understand the composition of the ocean (Fifer et al., 2022; Glein & Waite, 2020; Postberg et al., 2018). Gases in the plume were analyzed by the Cassini spacecraft's Ion and Neutral Mass Spectrometer (Waite et al., 2004) during eight flythroughs of the plume (Waite et al., 2017), while ice grains were measured by the Cosmic Dust Analyzer (Srama et al., 2004) both in the plume and in the derivative E-ring (Postberg et al., 2011, 2023). The measurements suggest that the subsurface ocean is salty and contains dissolved gases and various organic molecules (Khawaja et al., 2019; Postberg et al., 2009, 2011, 2018; Waite et al., 2006, 2009, 2017). Recently, astrobiologically relevant phosphate and hydrogen cyanide have also been identified (Peter et al., 2023; Postberg et al., 2023). Modeling of the aqueous geochemistry in Enceladus's interior also predicts a phosphate- and carbonate-rich ocean, consistent with plume measurements (Hao et al., 2022; Randolph-Flagg et al., 2023).

The presence of salts in the ice grains of the plume provides strong evidence that the plumes originate from the subsurface ocean (Meyer et al., 2025; Postberg et al., 2009), while other evidence bears on the chemistry of the ocean. Amorphous silica nanograins propagating away from the Saturnian system are thought to originate from hydrothermal water-rock reactions occurring at

the interface between Enceladus's subsurface ocean and a rocky core (Hsu et al., 2015; Schoenfeld et al., 2023; Sekine et al., 2015). Molecular $H_2$ in the plume also suggests hydrothermal reactions (Waite et al., 2017). Gases in the plume may be sourced from the ocean, but the exact relationship between the gas composition of the plume versus dissolved gases in the ocean is uncertain, because fractionation processes like water vapor condensation and gas exsolution can create chemical differences between the ocean and plume (Fifer et al., 2022; Glein et al., 2015; Glein & Waite, 2020; Klenner et al., 2025).

The degree to which the plume is fractionated depends on several poorly constrained factors, such as the depth (or range of depths) where the ocean transitions into the plume, and the (potentially varying) width of the tiger-stripe fissures through which the plume erupts (Fifer et al., 2022). While detailed predictions vary between fractionation models, most estimates of Enceladus's ocean composition predict relatively abundant gases including $CO_2$, $H_2$, $CH_4$ and $NH_3$ (Bouquet et al., 2015; Fifer et al., 2022; Glein & Waite, 2020; D. L. Matson et al., 2012; Waite et al., 2017). Because of these high predicted gas concentrations, and ice grain measurements that suggest the ocean is rich in carbonate or bicarbonate salts, Enceladus is sometimes described as having a "perrier" or "soda" ocean (Glein et al., 2015; D. Matson et al., 2010; D. L. Matson et al., 2012).

**Table 1: Comparison of bulk volatile abundances and D/H ratio on Enceladus versus Jupiter-Family Comets**

| Species | Enceladus | Comets |
|---|---|---|
| Total Ammonia ($NH_3$+$NH_4^+$) | <0.17% [a] | 0.2 – 4% [b, c] |
| Dissolved Inorganic Carbon ($CO_2$+$HCO_3^-$+$CO_3^{2-}$) | <0.16% [a] | 2 – 30% [d] |
| Methane ($CH_4$) | <0.001% [a] | 0.1 – 0.8% [c] |
| Carbon Monoxide (CO) | <0.003% [*] | 0.3 – 8.8% [c] |
| | | |
| D/H | Plume: $2.9\ (+1.5/-0.7) \times 10^{-4}$ [e]<br>Northern Hemisphere: $2.2 \pm 0.6 \times 10^{-4}$ [f]<br>Southern Hemisphere: $1.9 \pm 0.6 \times 10^{-4}$ [f] | $1.37 – 2.95 \times 10^{-4}$ [g, h] |

Bulk abundances of species are given as a percent relative to water. Species abundances for Enceladus are derived from plume data with a fractionation model and extrapolated to the bulk ocean and ice shell, excluding the core. D/H is the ratio measured in $H_2O$.
[a](Fifer et al., 2022); [b](Altwegg et al., 2020); [c](Lippi et al., 2021); [d](Mumma & Charnley, 2011); [e](Waite et al., 2009); [f](Clark et al., 2019); [g](Altwegg et al., 2015); [h](Mandt et al., 2024).
[*]Estimated from ~0.7% mixing ratio in the plume from Peter et al. 2023 (Peter et al., 2023), and assuming comparable fractionation to $CH_4$ from the Fifer et al. 2022 (Fifer et al., 2022) model.

### *1.2. A comet-like composition for Enceladus?*

It has been suggested that Enceladus formed from comet-like building blocks because the plume is volatile-rich (Waite et al., 2006, 2009, 2017). Comets have high abundances of $H_2O$, $CO_2$, $CH_4$ and $NH_3$, albeit in the form of ices (see Table 1; (Altwegg et al., 2020; Lippi et al., 2021; Mumma & Charnley, 2011). Of particular interest are Jupiter-family comets, which also originate in the outer solar system. The D/H of water that was measured in Enceladus's plumes and of ice at the surface is similar to the D/H ranges of Jupiter-family comets (Altwegg et al., 2015; Clark et al., 2019; Mandt et al., 2024; Waite et al., 2009). Organic molecules detected on Enceladus (Postberg et al., 2018) are also consistent with a cometary origin (Schuhmann et al., 2019).

Consequently, a comet-like composition is a reasonable initial composition for Enceladus (McKinnon et al., 2018).

However, abundance discrepancies exist between Enceladus's and cometary volatiles. For example, carbon monoxide (CO) is abundant in comets, at similar abundances to $CO_2$, but CO's presence in the plume could not be confirmed by INMS (McKinnon et al., 2018) until recently (Peter et al., 2023). $CO_2$ is also generally at lower abundances in the plume relative to water than it would be in comets, but can be explained by other forms of Dissolved Inorganic Carbon (DIC) in the ocean, which are relatively abundant, i.e., $CO_3^{2-}$ and $HCO_3^-$ (Fifer et al., 2022; Glein & Waite, 2020; McKinnon et al., 2018). In other words, primordial $CO_2$ would have speciated into these alternative forms when the ocean formed. Carbonate minerals may have also precipitated in the rocky core of Enceladus, meaning that a separate, solid reservoir of inorganic carbon that is *not* expressed in the plume is needed to account for Enceladus's total $CO_2$ (Glein & Waite, 2020).

The degree to which Enceladus's composition resembles comets depends on the previously mentioned fractionation processes. For example, models that predict significant removal of water vapor over the course of plume eruption find dissolved gas abundances in the ocean that are at lower concentrations than in comets (Glein et al., 2015; Glein & Waite, 2020). On the other hand, the volatile abundances estimated in Fifer et al. (2022) are reproduced in Table 1, and compared to more volatile-rich abundances from Jupiter-family comets. From these estimates, Enceladus reaches approximately cometary levels of total ammonia (summing $NH_4^+$ and $NH_3$), and has within an order of magnitude of cometary levels of dissolved inorganic carbon (DIC, summing $CO_2$, $HCO_3^-$, and $CO_3^{2-}$). The aforementioned precipitated carbonate in the core could represent a secondary reservoir of inorganic carbon to close this apparent gap.

However, $CH_4$ is at least two orders of magnitude lower on Enceladus than in comets (Table 1). It is worth noting that this estimate for $CH_4$ is the highest of any recent estimates for Enceladus's ocean (Fifer et al., 2022), and yet it still falls far short of cometary values. If a cometary composition is a good starting assumption for Enceladus, then why is the $CH_4$ abundance much lower today? Where did the $CH_4$ go?

### *1.3. A dynamically evolving volatile composition*

The discrepancy in Enceladus's $CH_4$ budget suggests that $CH_4$ has been lost, possibly through plume eruption. Because the molar ratio of $CH_4$ to water is likely higher in the plume than in the predicted ocean composition (Fifer et al., 2022; Glein et al., 2015; Glein & Waite, 2020), more $CH_4$ should be lost relative to water. This means that $CH_4$ should become more dilute in the ocean over time (and that it was more concentrated in the past), and the same should be true of $CO_2$ and $NH_3$.

Long-term plume eruption may also lead to isotopic evolution of Enceladus's volatiles, e.g., the deuterium/hydrogen (D/H) ratio of water. Whether Enceladus's plume is in vapor equilibrium with ice at the plume outlet (e.g., (Ingersoll & Nakajima, 2016) or out of equilibrium (i.e., supersaturated) with respect to the surface ice due to rapid evaporation or sublimation, the D/H of water vapor in the plume should be lighter than the D/H of Enceladus's ocean and/or surface. Both equilibrium and kinetic fractionation between water vapor and a liquid (or solid) phase favor the lighter isotopologue entering the gas phase (Cappa et al., 2003; Lamb et al., 2017). At present, the uncertainties in measurements of D/H in the plume gas and at Enceladus's surface are too great to confirm whether fractionation currently occurs between the plume and surface D/H (see Table 1; (4, 31). But if Enceladus's plume D/H is lighter than the bulk D/H, as expected from

isotopic fractionation factors between phases, then long-term eruption should drive the bulk D/H heavier over time.

The possibility of a dynamically evolving Enceladus that is continuously losing gas has not been considered in depth before, but this scenario bears on whether Enceladus's ocean is inhabited. For example, Affholder et al. (2021) explored sources of $CH_4$ on Enceladus, with numerical models of both abiotic (hydrothermal) and biotic (methanogenic) production of $CH_4$. They assumed that Enceladus's $CH_4$ is in a steady state, and showed that abiotic sources were insufficient to reproduce the observed $CH_4$ eruption rates. Therefore, under steady state conditions, and if an origin of life on Enceladus was favorable, they concluded that plume $CH_4$ fluxes would be more likely biological than geochemical, with the caveat that $CH_4$ could alternatively be primordial, i.e., left over from formation. In fact, the $CH_4$ could be a primordial remnant from an initial cometary composition.

Here, we explore the possibility of long-term plume eruption over geologic (Myr – Gyr) timescales, and the consequent budgets of $CH_4$, inorganic carbon, and ammoniacal species on Enceladus. Our reverse modeling approach determines if a chemically evolving ocean allows Enceladus's $CH_4$ to be solely primordial. By modeling the effects of long-term eruption, we aim to answer whether Enceladus could have started with a cometary budget of $CH_4$ and lost it over time, and whether the modern eruption rates and inferred volatile abundances in the ocean are consistent with such a picture. We explore how ocean chemistry may have changed over time, and constrain the longevity of plume eruption by determining at what point in the past (if any) Enceladus possessed a cometary budget of $CH_4$, inorganic carbon, and ammoniacal species. Finally, we estimate upper bounds on the potential long-term D/H fractionation on Enceladus due to preferential loss of light H in the plume, and compare the results with cometary D/H to

assess if a cometary starting D/H ratio for Enceladus is reasonable.

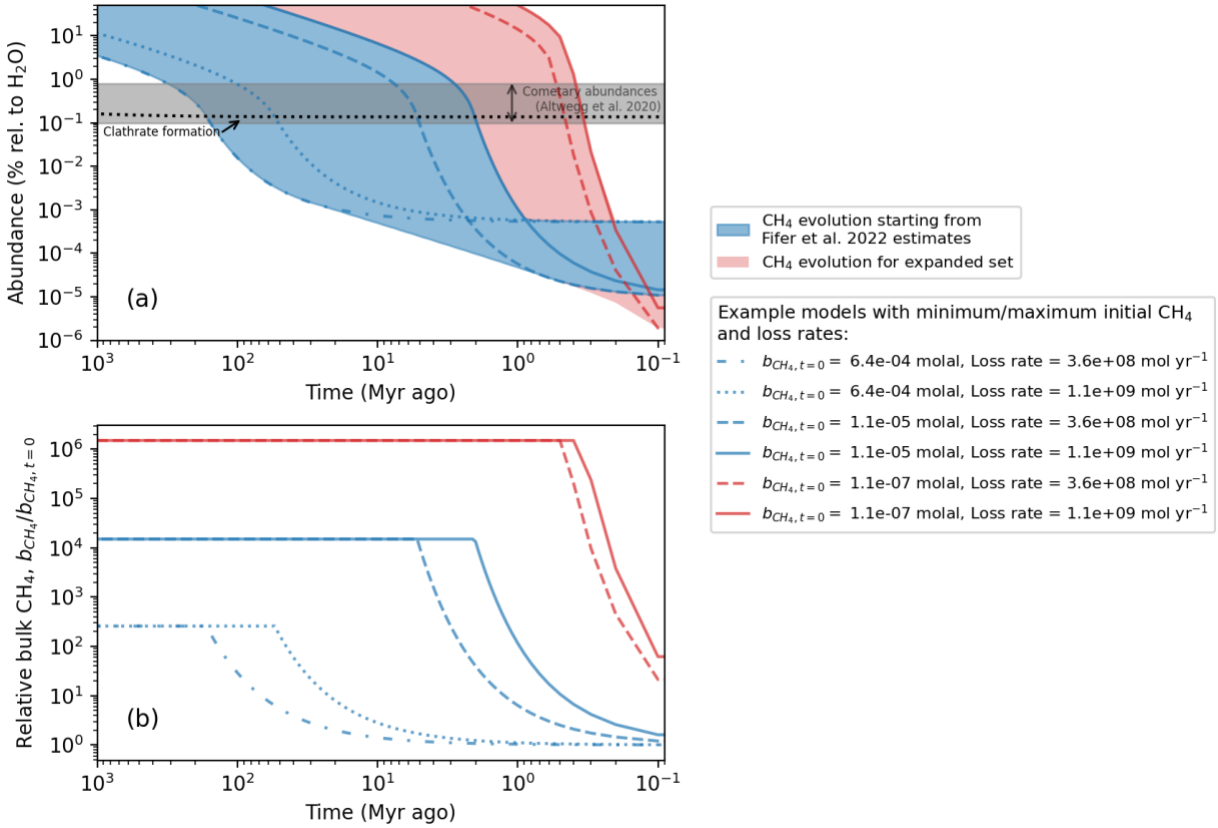


**Fig. 1. The modeled evolution of $CH_4$ on Enceladus. (A)** Model results for the evolution of bulk $CH_4$ abundance on Enceladus (blue shaded region), starting from modern values on the right, and going back in time to the left (up to 1 Gyr ago). The red-shaded region is an expanded set of models that includes 100-times lower modern $CH_4$ abundances than predicted by Fifer et al. (2022). The solid, dashed, or dotted lines are example models with initial $CH_4$ and loss rates at the extreme ends of the explored parameter space (blue for the "standard" set of initial model conditions, red for the expanded set with lower modern gas concentrations). The y-axis shows the bulk $CH_4$ abundance as a percent relative to water, where the water abundance includes the ocean and ice shell. The grey shaded region represents the range in $CH_4$ ice observed in comets, as a percent relative to water ice (Altwegg et al., 2020). Above the dotted black line $CH_4$ becomes saturated in the aqueous phase, and clathrates begin to form. Plume eruption lasting between ~2-300 Myr could explain the modern discrepancy between Enceladus's $CH_4$ abundance and a cometary starting composition. **(B)** Model results for the time-dependent $CH_4$ concentration as a ratio to the modern ($t$=0) $CH_4$ concentration. The different lines represent the same combinations of input parameters (initial $CH_4$ concentration, loss rate) as in (a). All lines eventually plateau when they reach the same saturation concentration of $CH_4$, but the y-axis value where the lines plateau differ between models because the y-axis is a ratio to the initial (modern) concentration. Thus, cases with low modern abundances (e.g., the red lines) reach higher $b_{CH4}/b_{CH4(t=0)}$ ratios than cases with higher modern abundances. As a result, cases with low modern abundances also have the greatest plume loss rates and recover cometary abundances most rapidly, due to the linear dependence between loss rate and $b_{CH4}/b_{CH4(t=0)}$ in our model (Equation (1)).

## 2. Results

Using the reverse evolution model, we obtain a range of possible histories for Enceladus's volatile inventory. In general, we calculate that the ocean would have contained higher concentrations of volatiles in the past. However, the evolution of inorganic carbon and ammoniacal species is complicated by their aqueous speciation (see Section 4.1). So, we find two distinct paths for Enceladus's chemical evolution (depending on uncertainty in the modern ocean and plume compositions) that lead to two endmembers: 1) an early Enceladus ocean that is $CO_2$-rich and relatively acidic, and 2) an early Enceladus ocean that is $NH_3$-rich and relatively basic. We describe these two diverging paths in Sections 2.2. and 2.3 and explore the initial parameters that lead to the diverging endmember compositions in the Discussion section.

### *2.1. A $CH_4$-rich, comet-like early Enceladus*

Volatile enrichment in Enceladus's past is clear in the results for $CH_4$ (Figure 1). Figure 1 shows the sum of aqueous $CH_4$ and $CH_4$ clathrates as a function of time. Moving backward in time, $CH_4$ concentrations increase because the ratio of $CH_4/H_2O$ is higher in the plume than in the ocean. As the relatively gas-rich plume that is lost to space is added back into the ocean in the reverse model, the ocean becomes more gas-rich too. Simultaneously, as the $CH_4$ concentration increases backwards in time, the eruption loss rate increases as well (following Equation (1)) creating a feedback between aqueous concentrations and eruption rates. The exponential increase in overall $CH_4$ abundance continues until the solubility limit, ~3 x $10^{-3}$ mol per mol $H_2O$ (Waite et al., 2009), which is a bulk abundance of ~1.35 x $10^{-3}$ mol per mol $H_2O$ (due to the added water mass of an assumed pure ice shell) and shown by the dotted line in Figure 1. At this solubility limit, achieved

~2 to 100 Myr ago, the concentration of aqueous $CH_4$ becomes constant, as does the $CH_4$ eruption rate, and all additional $CH_4$ further back in time is captured into clathrates.

Going forward in time, the ocean was clathrate-rich early in Enceladus's history and aqueous $CH_4$ (and its eruption rate) was initially held constant due to saturation. However, the total $CH_4$ budget decreased as $CH_4$ was lost via the plume and replenished by dissociating clathrates (Figure 1). Once the supply of clathrates was completely exhausted, both aqueous $CH_4$ and eruption rates declined over time to their lower modern values. The results of our model indicate that cometary levels of $CH_4$ existed ~2 to 300 Myr ago for plume eruption at modern rates of activity (Figure 1).

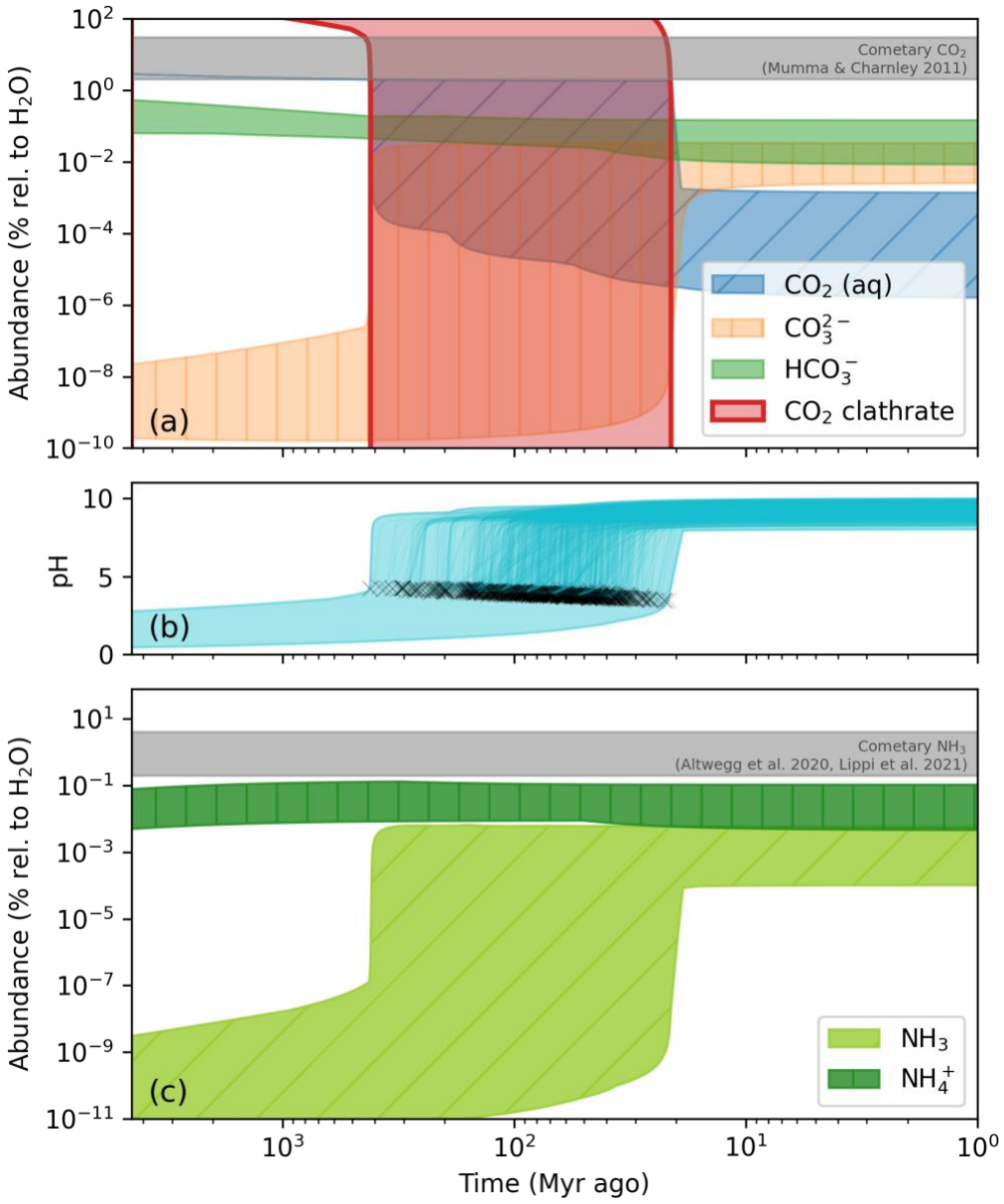


**Fig. 2. Model results showing an acidic, $CO_2$-rich early Enceladus ocean.** Model results show two endmembers, an acidic, $CO_2$-rich early Enceladus ocean (see Section 2.2), and a basic, $NH_3$-rich ocean (see Section 2.3). Here, the results for the former are shown. **(A)** The modeled reverse evolution of carbonate species on Enceladus, starting from modern values on the right, and going back in time to the left. Cometary levels of inorganic carbon are recovered in the reverse model for plume eruption lasting between 20 – 400 Myr. **(B)** Model results for the reverse evolution of pH. Individual models are shown as low-opacity dark blue lines and all models (for the $CO_2$-rich, acidic endmember) are encompassed within the lighter blue shaded region. The black x's indicate the times (and corresponding ocean pHs) when individual model runs *exceed* cometary levels of $CO_2$ (see (a)), and the individual model lines end at those points. At its most acidic, this version of an early Enceladus ocean would have pH ~4–5. **(C)** Model results for the reverse evolution of ammonia species. Although total ammonia does not cross into cometary abundances, it does remain within a factor of ~1.2 of the minimum ammonia abundance observed in Jupiter-family comets (Altwegg et al., 2020; Lippi et al., 2021). Additional ammonium could also be present today if present in clay minerals in the core.

### *2.2. A $CO_2$-rich and acidic early Enceladus ocean endmember*

The chemical evolution of inorganic carbon and ammoniacal species leads to two distinct early endmember compositions. In the first endmember, the evolution of $CO_2$ and related species follows a similar trend as for $CH_4$, where we find overall higher concentrations of inorganic carbon in Enceladus's past (Figure 2a). However, the rate of increase (in the reverse model) is somewhat slower than for $CH_4$, because as $CO_2$ is added back into the ocean it speciates partially into $HCO_3^-$ and $CO_3^{2-}$, which do not contribute to the overall eruption rate. As such, it takes longer to recover (or in the forward model, to lose) cometary levels of inorganic carbon through plume eruption alone, ~20-400 Myr (Figure 2a). By coincidence, the saturation concentration of $CO_2$ (seen in Figure 2a where $CO_2$ plateaus into a single blue line and clathrates become more dominant) translates to a bulk abundance that is approximately the same as the minimum cometary abundance.

Higher concentrations of $CO_2$ in Enceladus's past produce a lower pH in the ocean, as low as ~4 during the $CO_2$-rich period >20 Myr ago (Figure 2b). The more acidic pH changes the dominant form of carbon in the ocean. Early Enceladus begins with most $CO_2$ in the form of clathrates; once the clathrates are exhausted and aqueous forms dominate, the main component is $CO_2$ (aq), and then $HCO_3^-$ (Figure 2a).

In contrast to $CH_4$ and inorganic carbon, the total ammonia abundance ($NH_3$ + $NH_4^+$) on Enceladus (in this set of models) has a less drastic evolutionary path, remaining relatively steady even over billions of years (Figure 2c). While total ammonia initially trends towards slightly higher abundances in the past due to increased aqueous $NH_4^+$ (the likely dominant form today), the amount of aqueous $NH_3$ tends to decrease by three to four orders of magnitude going backwards in time. Both the relatively steady total ammonia and lower $NH_3$ in the past are caused by the behavior of the carbonate system and the lower pH in the past. With excess of $CO_2$ driving the

ocean to lower pH values in the past, the speciation of $NH_3$ shifts strongly towards $NH_4^+$. Low abundances of $NH_3$ in turn lead to low exsolution rates (Equation (1)), so that further eruption has minimal effect on total ammonia.

In this inorganic-carbon-rich endmember, the abundance of total ammonia relative to water exhibits a slight *decrease* moving backwards in time, at times >~1 Gyr ago (Figure 2c). This is because $NH_3$ reaches a concentration low enough that its exsolution rate is outpaced by the eruption rate of water vapor, which is constant in our model. When the ratio of $NH_3/H_2O$ in the ocean is so low that $NH_3$ exsolution is negligible, then even as the total moles of $NH_3$ in the ocean remain relatively constant, the $NH_3$ abundance relative to water is controlled by adding or removing water via the plume. At this stage, $NH_3$ is diluted by the addition of water (in the reverse model) or concentrated by its removal (in the forward model) of water. However, the billions of years of eruption that are required to reach this stage are unlikely, as we will explore in the Discussion section.

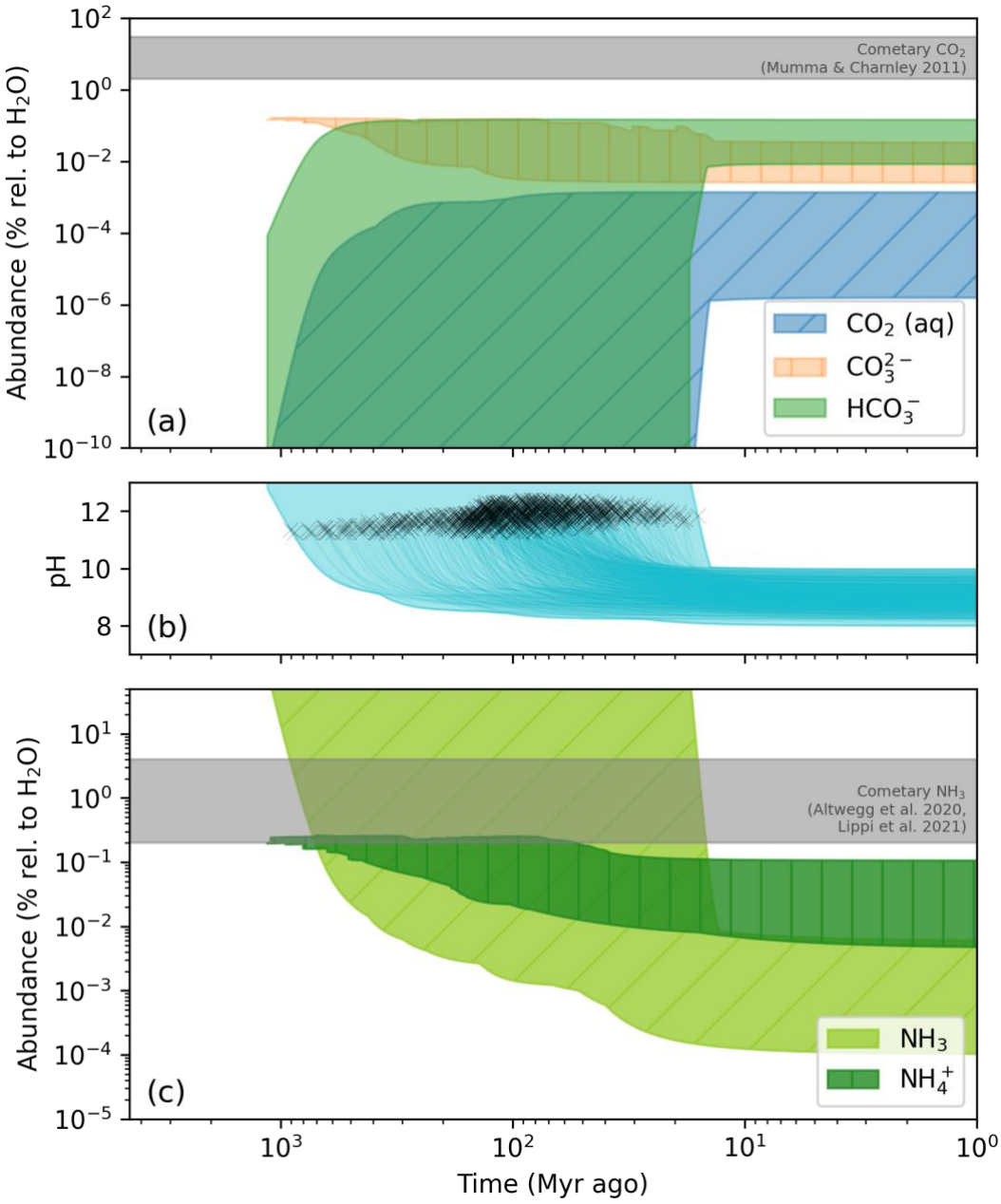


**Fig. 3. Model results for the second endmember, a basic, $NH_3$-rich early Enceladus ocean (see Section 2.3).** **(A)** The modeled reverse evolution of carbonate species on Enceladus, starting from modern values on the right, and going back in time to the left. Cometary abundances of inorganic carbon are not recovered in this endmember, but additional carbonate could be present in the form of minerals in the core (Glein & Waite, 2020). **(B)** Model results for the reverse evolution of pH. Individual models are shown as low-opacity dark blue lines and all models (for the $NH_3$-rich, basic endmember) are encompassed within the lighter blue shaded region. The black x's indicate the times (and corresponding ocean pHs) when individual model runs *exceed* cometary levels of $NH_3$ (see (c)), and the individual model lines end at those points. At its most basic, this version of an early Enceladus ocean would have pH ~11–12. **(C)** Model results for the reverse evolution of ammoniacal species. Cometary levels of ammonia are recovered in ~15 Myr – 1 Gyr of continuous eruption at modern rates.

### *2.3. An $NH_3$-rich and basic early Enceladus ocean endmember*

In the second group of model outcomes, the histories of inorganic carbon and ammoniacal species are swapped, suggesting an $NH_3$-rich and relatively $CO_2$-poor early ocean composition for Enceladus (Figure 3). We discuss the modern conditions that lead to the split in endmembers in Section 3.2. From the perspective of the reverse evolution model, this is a set of cases where the $NH_3$ being added back into the ocean outpaces the $CO_2$ being added in, resulting in an early ocean pH that is increasingly basic (Figure 3b). The basic pH amplifies this initial trend, as ammoniacal speciation trends away from highly soluble $NH_4^+$, and towards less soluble $NH_3$. Because $NH_3$ (aq) is the controlling factor on $NH_3$ exsolution, the loss rate via exsolution into the plume (or the rate at which $NH_3$ is added back into the ocean in the reverse model) increases with this shift in speciation. Thus, $NH_3$ continues to increase in the reverse model, ultimately recovering cometary abundances of $NH_3$ between 15 Myr – 1 Gyr of total plume eruption (Figure 3c).

By contrast, in this $NH_3$-rich endmember, dissolved inorganic carbon fails to reach cometary abundances when the effects of plume eruption are reversed even over the age of the solar system (Figure 3a). The reason for this is again illuminated by the pH evolution (Figure 3b). More basic pH causes the dominant inorganic carbon species to shift (in the reverse model) from $CO_2 \rightarrow HCO_3^- \rightarrow CO_3^{2-}$. Speciation of $CO_2$ into ionic forms also prevents the formation of $CO_2$ clathrates in this endmember. With low concentrations of aqueous $CO_2$, the $CO_2$ exsolution rate stays relatively low, so the efficiency of plume eruption as a loss mechanism stays low, and thus the influence of plume eruption on the long-term evolution of *total* dissolved inorganic carbon is negligible. This relative lack of evolution for total DIC suggests that, in this subset of model cases, the modern DIC in Enceladus's ocean (that is also expressed in the plume) closely reflects the initial DIC budget that Enceladus acquired during formation.

### *2.4. D/H evolution*

Generally, our model of D/H evolution (Section 4.2) predicts that the isotopic content of Enceladus's water has grown slightly heavier over time, meaning that the accreted D/H may have been lighter than what we observe today (Figure 4). However, given the large uncertainty in D/H measurements at Enceladus (Clark et al., 2019; Waite et al., 2009), and in cometary D/H values (Altwegg et al., 2015; Mandt et al., 2024; see Table 1), the evolution of Enceladus's D/H provides little constraint on the timescales of eruption. The model with equilibrium fractionation between the icy plume outlet and the plume vapor has only a minor effect on the long-term evolution even over the age of the solar system, with the initial D/H only lighter than modern values by a factor of ~.85 (green trend in Figure 4). Long-term eruption with fractionation closer to the maximum (blue trend in Figure 4) could potentially be more illuminating as a measure of eruption longevity if we had better certainty of Enceladus's D/H today. However, even in the maximum fractionation case, the accreted D/H is only as low as ~.55 of the modern value.

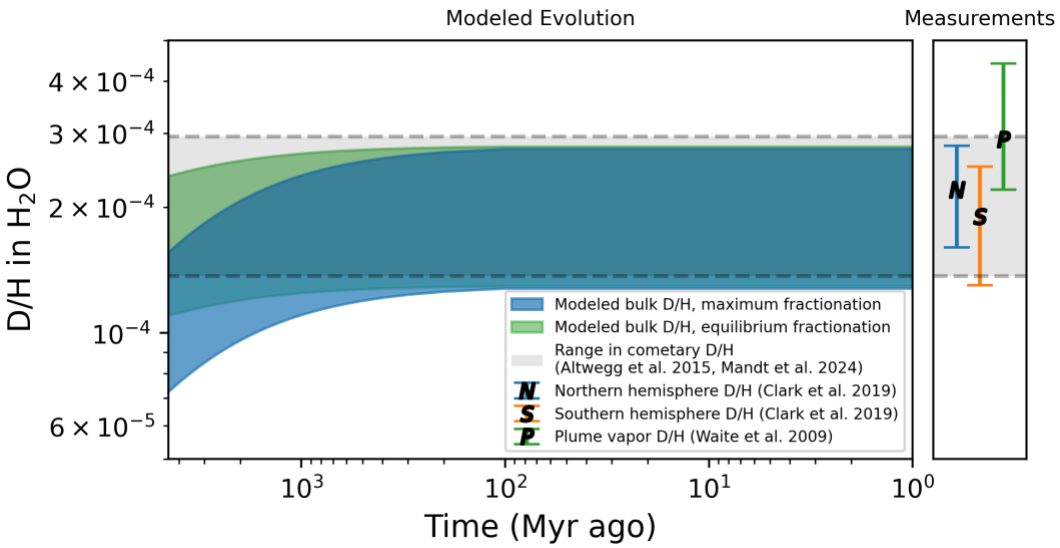


**Fig. 4. Modeled D/H evolution and measurements of D/H at Enceladus.** The modeled long-term evolution of D/H, assuming a case for maximum fractionation where the plume contains 100% light H (blue shaded region), and a case assuming equilibrium fractionation between the plume vapor and icy plume outlet (green shaded region). The grey shaded region with dotted lines shows the D/H range measured in Jupiter-family comets. The error bars at right show measurements of D/H in the plume and at Enceladus's surface (Clark et al., 2019; Waite et al., 2009). In our models, the modern bulk D/H (including the ocean) is assumed to be equal to that of the surface.

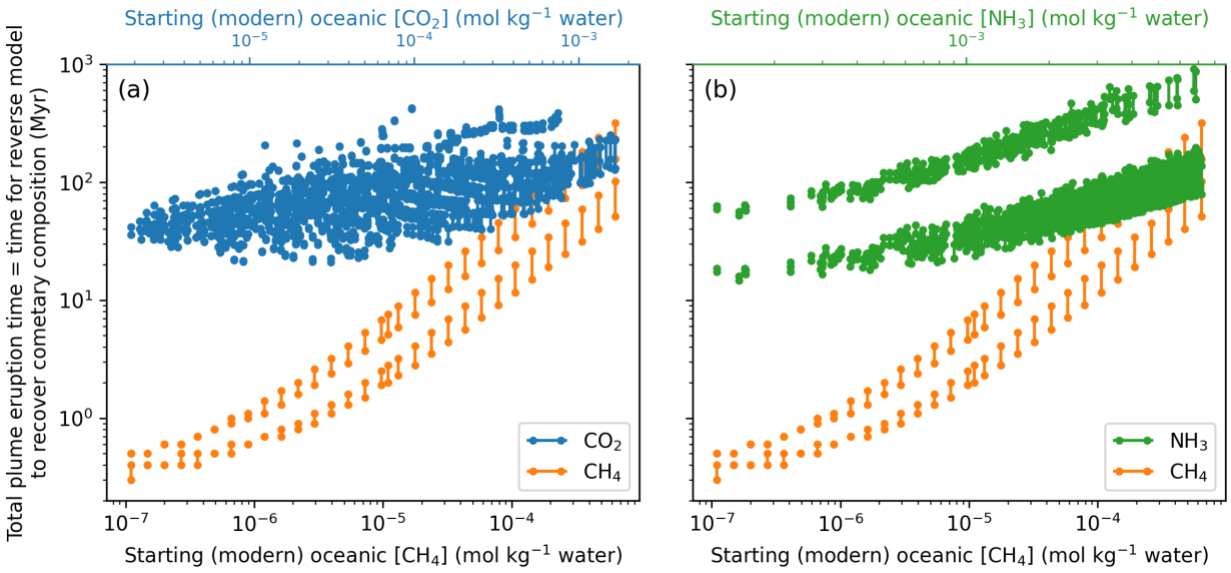


**Fig. 5. Comparison between permissible eruption timescales for different volatiles, assuming a cometary starting composition for Enceladus.** The y-axis shows the time to recover cometary abundances of a volatile (in the reverse model), given some modern oceanic concentration (x-axes). In both plots, the bottom and top x-axes are aligned based on the correlation between their ranges in uncertainty. In other words, for a given $CH_4$ concentration on the bottom x-axis, the corresponding concentration on the top x-axis is a reasonable estimate for the volatile labeled there. **(A)** A comparison between permissible eruption timescales based on our reverse modeling for $CO_2$ and $CH_4$, in the $CO_2$-rich endmember that recovers cometary levels of both $CO_2$ and $CH_4$. The orange markers are for $CH_4$ (refer to Figure 1), the blue for $CO_2$ (refer to Figure 2a). The eruption timescales for $CO_2$ and $CH_4$ are most self-consistent in models with a relatively gas-rich ($>10^{-4}$ mol $kg^{-1}$) modern ocean, and have overlapping eruption timescales of ~30–300 Myr. **(B)** A comparison between permissible eruption timescales based on our reverse modeling in the $NH_3$-rich early endmember that recovers cometary levels of both $NH_3$ and $CH_4$. The orange markers are for $CH_4$ (Figure 1), the dark green are for $NH_3$ (as shown in Figure 3c). Here again, the eruption timescales for both volatiles are most self-consistent for a gas-rich modern ocean, and have overlapping eruption timescales of ~30–300 Myr.

## 3. Discussion

### *3.1. Combined history of volatile evolution*

Taken together, the modeled evolution of $CH_4$, $CO_2$, and $NH_3$ suggest that Enceladus's plume eruption may have persisted for ~$10^7$–$10^9$ years, assuming a cometary starting composition, and comparable eruption rates to today. More specifically, our results for $CH_4$ constrain plume eruption to 2–300 Myr, whereas the models of $CO_2$ evolution (for the $CO_2$-rich early endmember) suggest eruption for 20–400 Myr. $NH_3$'s evolution (for the $NH_3$-rich early endmember) constrains

eruption to 15 Myr–1 Gyr. Based on the overlap between timescales of $CH_4$ eruption and either $CO_2$ or $NH_3$ eruption (Figure 5), we estimate that plume eruption should have lasted between ~30–300 Myr (in both endmember scenarios).

Our model results may help to explain the apparent deviations in Enceladus's modern volatile budget from cometary levels (Table 1). $CH_4$ is lost most rapidly, because $CH_4$ cannot speciate into more soluble ionic forms that would be retained in the ocean, so $CH_4$ is the most depleted volatile relative to Jupiter-family comets. On the other hand, $CO_2$ can distribute into alternative ionic forms that tend to remain in the ocean, preserving higher abundances in the ocean even over longer timescales of eruption. Finally, $NH_3$ is similarly retained over long timescales because most total ammonia is likely in the form of more soluble $NH_4^+$.

Notably, however, we find that Enceladus's ocean can retain only *one* of the latter two groups of species (inorganic carbon or ammoniacal species). For example, in the $NH_3$-rich, basic early Enceladus ocean, the high pH leads to speciation towards $NH_3$, which is readily lost to plume eruption, while simultaneously pushing inorganic carbon speciation towards the more soluble and more easily retained $HCO_3^-$ and $CO_3^{2-}$. In contrast, the acidic, $CO_2$-rich early Enceladus ocean leads to higher loss rates of $CO_2$ in the plume. The acidic conditions leave ammonia mostly in the protonated, soluble form of $NH_4^+$, which tends to remain in the ocean. In other words, a high post-accretion concentration of either inorganic carbon or total ammonia in Enceladus's ocean causes its loss via the plumes, but the other volatile is retained in the ocean. As a result, our reverse models tend to recover *either* cometary levels of inorganic carbon *or* total ammonia, but not both. This result is consistent with previous models showing that the interaction between inorganic carbon and ammoniacal species is a key determinant to the chemistry of ocean worlds (40), and even their early atmospheres (Amsler Moulanier et al., 2025).

$CO_2$ clathrates are only present in the early acidic $CO_2$-rich endmember because $CO_2$ dissociates to maintain aqueous $CO_2$ at saturated concentrations. The fact that Enceladus's modern ocean pH is relatively alkaline (e.g., (Glein & Waite, 2020; Hsu et al., 2015; Postberg et al., 2009) may therefore suggest that $CO_2$ clathrates are not currently present in the ocean. A layer of $CO_2$ clathrates at the ocean floor might have inhibited water-rock reactions on early Enceladus (in the $CO_2$-rich endmember).

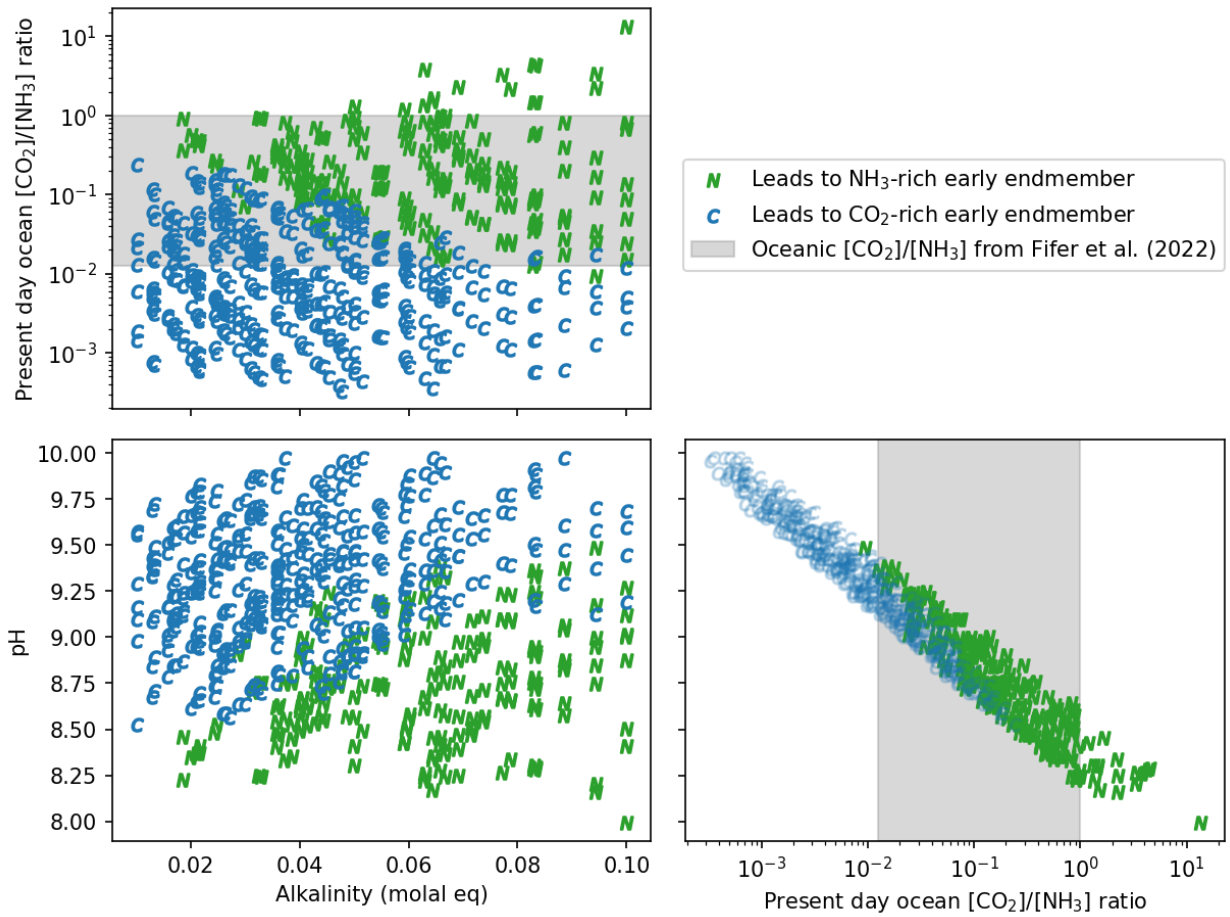


**Fig. 6. Early endmember compositions depending on uncertainty in Enceladus's modern ocean chemistry.** Early endmember compositions (distinguished by marker and color) are shown as a function of the wide range in possible chemical conditions in the modern ocean (initial parameters to the reverse evolution model; x- and y-axes). These plots show results for a model case with eruption rates of 2.2 x $10^9$ mol $yr^{-1}$ (corresponds to a plume mixing ratio of ~0.6%) for each of $NH_3$ and $CO_2$. In this case of 1:1 eruption rates for $NH_3$:$CO_2$, models that initialize with modern ocean conditions with relatively high pH, low total alkalinity and/or a low ratio of aqueous $CO_2$/$NH_3$ tend to lead to the acidic, $CO_2$-rich early endmember. By contrast, models with lower pH, higher total alkalinity, and/or a higher ratio of aqueous $CO_2$/$NH_3$ tend to lead to the basic, $NH_3$-rich early endmember. Cases where the eruption rates of $NH_3$:$CO_2$ are not 1:1 are explored in Figure 7.

### *3.2. Modern ocean & plume conditions that lead to distinct early endmembers*

The diverging paths of the $CO_2$-rich and $NH_3$-rich endmembers result from uncertainty in the present-day chemistry of Enceladus's ocean and plume. The modern ocean gas concentrations,

pH and total alkalinity are all critical inputs to our long-term evolution model, but depend on the highly uncertain relationship between the aqueous composition of the ocean and the (gaseous and solid) composition of the plume (e.g., Fifer et al., 2022; Glein et al., 2015; Glein & Waite, 2020; Klenner et al., 2025; Postberg et al., 2009, 2023). Figure 6 shows how combinations of chemical parameters of the modern ocean lead to the diverging endmembers, assuming that $NH_3$ and $CO_2$ are erupted at a rate of 1:1 (i.e., they have equal mixing ratios in the plume). Under that assumption, models that have low $CO_2/NH_3$ ratios in the modern ocean tend to lead to the $CO_2$-rich endmember, whereas models with high $CO_2/NH_3$ ratios tend to lead to the $NH_3$-rich endmember. This follows from the fact that, for a given volatile, a low concentration today implies efficient loss in the past. An analogous trend is seen in the evolution of $CH_4$ (Figure 1), where models with low modern concentrations recover high cometary abundances fastest due to the eruption rate scaling in equation (1). Similarly, models with high modern pH tend to lead to the $CO_2$-rich and acidic early endmember, and low modern pH conditions lead to the $NH_3$-rich and basic early endmember (Figure 6).

However, varying the present-day loss rates (plume mixing ratios) can drastically shift the tendency of our model to produce one endmember or another. Thus, the trends described above do not necessarily hold if the modern $NH_3/CO_2$ ratio *in the plume* is not 1:1. We ran a set of models with a plume ratio of $NH_3/CO_2$ ranging from 0.5 (representing plume mixing ratios of 0.3% $NH_3$ and 0.6% $CO_2$) to 3.0 (representing plume mixing ratios of 1.8% $NH_3$ and 0.6% $CO_2$, a closer approximation of the plume composition determined by Peter et al. (2023). For cases with plume $NH_3/CO_2 \leq 0.7$, all modern ocean chemistries reached the acidic, $CO_2$-rich endmember, regardless of the modern pH, total alkalinity, or $CO_2/NH_3$ ratio in the ocean (Figure 7). For cases with plume $NH_3/CO_2 \geq 1.9$, all modern ocean chemistries reached the basic, $NH_3$-rich endmember. Here again

we see that “efficient” loss of a particular volatile implies that it was much more abundant in the past. The ratio of $NH_3/CO_2$ in the plume is relatively uncertain, ranging from ~0.5 to ~4.3 (10), with more recent reanalysis suggesting a ratio of ~3.5 to ~4.6 (Peter et al., 2023). Therefore it is crucial to better resolve the time-average, precise relative abundance of $NH_3$ and $CO_2$ in the plume to better constrain the moon’s chemical history.

Improved constraints on the relative loss rates of $NH_3$ and $CO_2$ via Enceladus’s plume can be achieved through in situ analyses (e.g., mass spectrometry) or remote observations (e.g., absorption spectroscopy using stellar occultations). Europa Clipper will employ both mass spectrometry and absorption spectroscopy to characterize volatiles (and potential plumes) at Europa with the MAss Spectrometer for Planetary EXploration (MASPEX) and Ultraviolet Spectrograph (UVS) instruments, respectively (Retherford et al., 2024; Waite et al., 2024). Similar measurements could be performed by future missions to Enceladus (Hendrix et al., 2019; MacKenzie et al., 2022), and determine any temporal changes in plume composition.

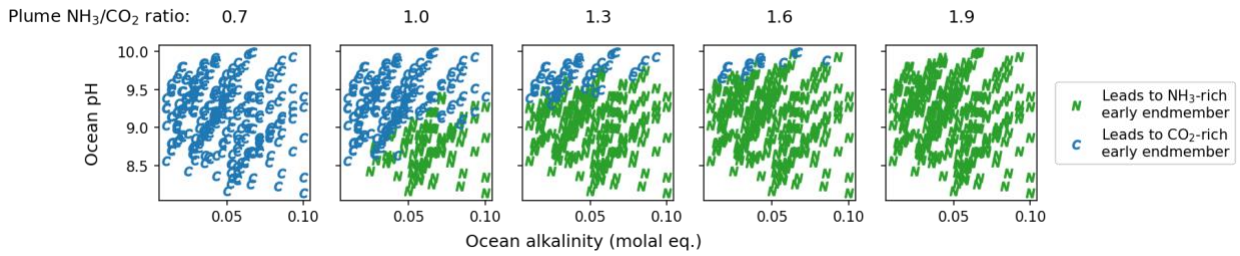


**Fig. 7. Early endmember compositions depending on uncertainty in the modern plume and ocean chemistry.** Early endmember compositions (distinguished by marker and color) are shown as a function of modern ocean alkalinity (x-axis), modern ocean pH (y-axis), and $NH_3/CO_2$ mixing ratio in the plume (separate subplots). Regardless of the modern ocean composition, a plume ratio of $NH_3/CO_2 \leq 0.7$ will always lead to the acidic, $CO_2$-rich early endmember. Conversely, a plume ratio of $NH_3/CO_2 \geq 1.9$ will always lead to the basic, $NH_3$-rich early endmember.

### *3.3. Independent constraints on the early composition of Enceladus's ocean*

While uncertainty in the present-day plume and ocean composition precludes us from determining which early endmember ($CO_2$-rich and acidic, or $NH_3$-rich and basic) is more likely, geochemical modeling of Enceladus shortly after accretion may provide insight. Based on previous geochemical studies, the ocean of Enceladus could have had a relatively high pH (~8-12) throughout its entire history (Neveu et al., 2017; Zolotov, 2007). If the ocean on an early Enceladus was a cometary melt, it would have had a pH of 6-10.8, depending on temperature and pressure (Neveu et al., 2017), prior to any water-rock interactions. Over its history, the ocean composition and alkalinity will have changed (independent of the plume loss we model here) because of water-rock reactions on the ocean floor. Interestingly, the pH of the fluid remains relatively constant across a range of W/R (water/rock) ratios, which could be used to represent the extent of aqueous alteration over time. However, temperature plays a large role in changing the pH of the ocean, with higher temperature producing a moderately basic pH (~8) and lower temperature generating even

higher pH (Neveu et al., 2017; Zolotov, 2007). These models align with the $NH_3$-rich endmember for early Enceladus.

Aqueous speciation throughout time has also been investigated thermochemically. For cometary fluid, over most temperature and W/R conditions, aqueous species are primarily reduced, e.g., carbon as $CH_4$, nitrogen as $NH_4^+$ and/or $NH_3$, and sulfur as $HS^-$ (Neveu et al., 2017). Resultant fluids from a model that reacted cometary fluid with a chondritic solid material were dominated primarily by $NH_3$, and secondarily by $CH_4$ (Neveu et al., 2017). Although $CH_4$ was more abundant than $NH_3$ in the starting fluid, it was also more easily lost (as in our model) to exsolution (Neveu et al., 2017). A second model that investigated fluid interaction with a CI chondritic-type interior had a resultant ocean fluid dominated by $Na^+$, $Cl^-$ and $HCO_3^-$ as major species, with a salinity of 2–20 g $kg^{-1}$ $H_2O$ (Zolotov, 2007). Both studies found that carbon solutes remain relatively high because the lack of divalent cations (such as $Ca^{2+}$, $Mg^{2+}$) prevents massive carbonate precipitation (Neveu et al., 2017; Zolotov, 2007). However, other models suggest that carbonate mineral precipitation is likely widespread on Enceladus (Glein & Waite, 2020), which our $NH_3$-rich endmember requires to match cometary levels of inorganic carbon (see Section 3.4). Zolotov (2007) found that low temperature (<150°C) water-rock reactions tend to produce very low abundances of $CO_2$ and $CH_4$, so that high temperature reactions might be needed to account for the measured plume composition. While not definitive, these modeling studies of the early Enceladus ocean composition are more consistent with the basic, $NH_3$-rich endmember.

### *3.4. Additional volatile reservoirs and sources*

Our model focuses on the changing budgets of volatiles that are dissolved in the ocean, and our model assumes that solid phases containing $CO_2$, $NH_3$, and $CH_4$ make minimal contributions

to Enceladus's bulk chemistry. However, two additional factors could affect volatile budgets: (1) minerals in the core, and (2) $CH_4$ resupply.

*3.4.1. Minerals in the core:* The presence of volatile-bearing minerals in the core could resolve the tendency of our reverse models to recover only one of cometary inorganic carbon or total ammonia. Modeling suggests that Enceladus's core may become more carbonate-rich over time, as $CO_2$ (aq) reacts with the rocky core to form siderite ($Fe_2CO_3$) and/or magnesite ($Mg_2CO_3$) (Glein & Waite, 2020). Carbonate minerals in the core could be where currently "missing" $CO_2$ resides. Glein & Waite (2020) estimate that at least 30% of Enceladus's core has likely been carbonated, based on reasonable estimates for the water/rock ratio and starting composition of Enceladus.

We can calculate how the above estimates of carbonation from Glein and Waite (2020) would compare to cometary abundances, and include this geological carbon reservoir in our models. For a spherical core of radius ~190 km and density ~2400 kg/m$^3$ (Hemingway et al., 2018), ~30% of the core would translate to ~2.07 x $10^{19}$ kg of carbonated rock. Assuming an average molar mass of 100 g mol$^{-1}$ (corresponding to a 50:50 split between $FeCO_3$ and $MgCO_3$), one can estimate that the bulk molar abundance of $CO_2$ may be as high as ~10.5% relative to $H_2O$, an abundance that is well within cometary ranges (see Table 1). Even if only ~6% of the core were carbonated today, this would translate to the low end of the Jupiter-family cometary range, ~2% $CO_2$ relative to $H_2O$.

If we include carbonate minerals in our model, we add a separate reservoir to Figure 2a that is already within the cometary range of $CO_2$ at modern times. Running the reverse model, the behavior of $CO_2$ (aq), $HCO_3^-$, $CO_3^{2-}$ and $CO_2$ clathrates is unchanged, so total DIC does not *exceed* cometary levels until approximately the same time of total eruption as the base model, ~400 Myr,

where the slope of changing abundance is steepest (Figure 2a). Thus, because the carbonate mineral model already possesses cometary levels of total $CO_2$ in the modern era, the permissible total time of eruption for $CO_2$ (in the inorganic-carbon-rich endmember) is between 0-400 Myr. In the $NH_3$-rich endmember (Figure 3), any timescale of eruption would be permissible for inorganic carbon if minerals in the core already contain cometary levels of $CO_2$. The evolution of $CH_4$ is unchanged by the presence of carbonate minerals, so the intersection of the two models ($CO_2$ including carbonate minerals, and $CH_4$) leads to an *overall* eruption rate of 2-300 Myr, for either endmember.

In the core, $NH_4^+$ could also be present. Secondary clay minerals such as saponite have been proposed as a product of water-rock interactions with Enceladus's rocky core (Hsu et al., 2015; Postberg et al., 2023; Sekine et al., 2015; Zolotov, 2007). Saponite and other smectite clay minerals readily exchange $NH_4^+$ for $Na^+$, $Ca^{2+}$, or $K^+$ cations (Alshameri et al., 2018; Mizutani et al., 1995; Sugahara et al., 2017), so if clays are present on Enceladus, they could constitute a "hidden" reservoir of ammonium, not necessarily expressed in plume eruption. However, total ammonia on Enceladus is likely very close to cometary levels today (Table 1), so our evolution models are already reconcilable with a starting cometary budget of total ammonia without invoking $NH_4^+$ minerals.

*3.4.2. $CH_4$ resupply:* Another process possibly missing in our model is endogenous $CH_4$ production, which is likely thermodynamically favorable on Enceladus (e.g., (Higgins et al., 2024; Liu et al., 2024). This $CH_4$ source could be abiotic (i.e., purely geological, through Fischer-Tropsch or analogous reactions), or biological. However, Affholder et al. (2021) demonstrated that likely fluxes of geological $CH_4$ would be insufficient to match eruption rates and maintain the steady state in the ocean, so a biological source was their favored explanation. Recent modeling of the

differentiating interiors of icy bodies like Enceladus suggests that primordial organic matter can accumulate in the core, up to ~10s of weight % (54, 55). The implications for the slow release of hydrocarbons (including $CH_4$) from such an organic-rich core have yet to be explored.

A clathrate contribution to Enceladus's $CH_4$ budget today is likely negligible for three reasons. First, the predicted concentrations of $CH_4$ in the ocean (Fifer et al., 2022; Waite et al., 2017) are far below the saturation concentration for clathrates, ~0.17 molal, so dissolved $CH_4$ should only be undersaturated if clathrate dissociation is somehow kinetically limited. Second, $CH_4$-clathrate dissociation is rapid (Gainey & Elwood Madden, 2012) compared to the timescales of plume eruption. As an example, a global layer of clathrates covering the surface of Enceladus's rocky core would have a surface area of ~$4.5 \times 10^{11}$ $m^2$, and multiplying this by a conservatively low empirical dissociation flux of $3 \times 10^{-6}$ mol $m^{-2}$ $s^{-1}$ (Gainey & Elwood Madden, 2012) produces an overall dissociation rate of ~$4 \times 10^{13}$ mol $yr^{-1}$, some ~4-5 orders of magnitude greater than the loss rate of $CH_4$ via the plume. Finally, the density of $CH_4$ clathrates is lower than that of water, so clathrates would rise to regions with lower hydrostatic pressures (closer to the ice shell) where they would become unstable and dissociate (Bouquet et al., 2015). On Earth, burial under seafloor sediment enables long-term storage of $CH_4$ clathrates (e.g., Buffett, 2000), but widespread sedimentation on Enceladus's seafloor is precluded by a lack of continental input.

If there is a sufficient supply of $CH_4$ to match eruption rates (due to biology, or some slow-releasing primordial source), then the lifetime of $CH_4$ in the ocean can be extended as long as that resupply mechanism is active, and the only constraint on total eruption timescales in our model comes from the other volatiles, $CO_2$ and $NH_3$. Even if $CO_2$ is being converted (abiotically or biotically) into $CH_4$, this secondary sink of $CO_2$ only negligibly affects the overall evolution of $CO_2$, because eruption rapidly becomes the biggest sink in the reverse model. Therefore the overall

eruption timescale permissible for $CO_2$ remains the same as the base model, ~20–400 Myr for the $CO_2$-rich endmember.

### *3.5. Possible loss of organic molecules via the plume*

Our model did not consider the loss and evolution of organic compounds (except $CH_4$). The current understanding of organics in Enceladus's ocean comes in large part from CDA analysis of ice grains (e.g., Khawaja et al., 2019; Postberg et al., 2018). However, ice grain eruption via the plume is not an efficient loss mechanism compared to gas loss, because ice grains constitute only ~10% of the plume mass (Hedman et al., 2018) and only ~10% of those ice grains escape from Enceladus's gravity (Schmidt et al., 2008) while the rest fall back to the surface (Porco et al., 2017). Importantly, the relationship between organic concentrations in ice grains versus the ocean is highly uncertain, so it is unclear whether steady loss of (a small fraction of) erupted organic-bearing ice grains would make the ocean more organic-rich or organic poor. Some lower-mass organics (e.g., acetylene, formaldehyde) may escape more readily because they volatilize easily. However, constraining the eruption rates of these molecules is difficult because of significant ambiguity in their abundance in the gas phase of the plume (Magee & Waite, 2017). We leave a more detailed exploration of organic evolution to future work.

### *3.6. The importance of future D/H measurements*

While the results of our model of D/H evolution are at present inconclusive about Enceladus's early composition and outgassing history, better measurements of the modern D/H at Enceladus may improve its usefulness as a chemical tracer. New measurements of the D/H in icy plume particles (which could be obtained using time-of-flight mass spectrometry (Ulibarri et al.,

2023)), and updated measurements of the plume gas and icy surface would all be helpful to constrain both the modern D/H of Enceladus and the degree of fractionation between Enceladus's bulk D/H and the material that is lost via the plume gas. In our calculation, we assume that the D/H of surface ice at the plume outlet is equal to the D/H elsewhere on the surface, but in reality they may differ. Models of plume eruption suggest that some amount of water vapor should condense onto the walls of the fissure, possibly rapidly enough to maintain equilibrium between the plume gas phase and the ice at the outlet (Glein et al., 2015; Nakajima & Ingersoll, 2016). Therefore ice closest to the plume outlet may more closely represent equilibrium fractionation of condensing water vapor from the plume.

Our second assumption, that the modern surface D/H is approximately equal to that in the ocean may be more grounded in reality, as the surface of Enceladus is coated in erupted plume particles, which are thought to reflect the ocean composition. Direct comparison between the D/H of ice particles in the plume and the broader surface ice could help to confirm or refute this assumption. The distribution of plume fallout is heterogeneous across Enceladus's surface, with much higher deposition rates at the south pole compared to the north pole (Southworth et al., 2019). Better spatially-resolved measurements of D/H at Enceladus's surface could test the validity of our long-term eruption model, as we would expect a heavier D/H where Enceladus's surface is youngest (i.e., near the plume source) and a lighter D/H where Enceladus's surface is older and plume fallout is minimal. The D/H of ejected ice particles from Enceladus can also be investigated to some degree on other moons of Saturn such as Rhea, due to transport of said particles via the E-ring (e.g., Hirata et al., 2014; Verbiscer et al., 2007). The D/H measured on the surface of Rhea, $1.8 \pm 0.3 \times 10^{-4}$, is close to that on Enceladus (Clark et al., 2019).

### *3.7. Comparison to other age estimates*

Our evolution models predict total eruption timescales of 30–300 Myr, with the possibility of eruption as long as 400 Myr if there is a sufficiently productive $CH_4$ source within Enceladus that has been active over the same $10^8$-year timescales. Age estimates for Enceladus range from ~100 Myr to 4.5 Gyr (see Cable et al., 2021; Nimmo et al., 2023 for reviews). Some models of tidal dissipation, orbital evolution, and ring particle dynamics in the Saturnian system estimate that Saturn's rings and most of its moons, including Enceladus, are only ~100 Myr old (Estrada & Durisen, 2023; Kempf et al., 2023; cf. Hyodo et al., 2025), suggesting that Enceladus may have reaccreted from material that originated from an earlier generation of moons (Ćuk et al., 2016). Other assumptions about Saturn's tidal dissipation produce ages for Enceladus between a few Gyr and the age of the solar system, ~4.5 Gyr (Fuller et al., 2016; Lainey et al., 2020; Neveu & Rhoden, 2019; Nimmo et al., 2018). Crater counts suggest that some parts of Enceladus's surface are 2–4 Gyr old (unlike the much younger south polar terrain), but these estimates have large uncertainties surrounding the impact history in the Saturnian system (Nimmo et al., 2023).

Our model does not constrain the age of Enceladus, only the duration of its eruptive activity, so our results allow for several possible histories. These possibilities include a young (100 Myr) Enceladus that has been active for 2–100% of its lifetime, or an old (4.5 Gyr) Enceladus that has been active for between 0.04–9% of its lifetime. We do not directly model the possible concentration of non-water solutes in the ocean due to freezing of the ice shell (e.g., Manga & Wang, 2007). However, we estimate that if the mass of the ice shell were added to the ocean mass (e.g., on a very early Enceladus where the entire hydrosphere is liquid), the ocean mass would only be ~2.2-times the current mass of the ocean. Therefore the concentrating effect of gradual freezing

of the ocean would be at most a factor of ~2.2, which is minimal compared to the orders of magnitude decrease in oceanic concentrations we predict due to eruption alone (Figures 1-3).

It is also worth comparing our results to other age estimates for plume and hydrothermal activity on Enceladus. Waite et al. (2009) found evidence for $^{40}$Ar in the gas phase of Enceladus's plume, and used its observed eruption rate to estimate that a reasonable starting reservoir of radiogenic $^{40}$Ar would be lost in less than 10 Myr of the present plume eruption rate. Others have estimated the longevity of plume eruption from the buildup of ice particles on other moons within Saturn's E-ring. Hirata et al. (2014) used crater counting to estimate that ice deposits on Helene originating from Enceladus's plume would have likely formed over 40-50 Myr of eruption. Ages of the E-ring deposits as young as 0.3–5 Myr, or as old as 200–500 Myr are also possible, depending on the rates and mass distributions of impactors in the Saturnian system (Hirata et al., 2014). By contrast, studies of icy regolith generation on Enceladus by plume fallout require Gyrs of eruption at modern rates to produce observed regolith thicknesses (Martin et al., 2017, 2023). This suggests that the plume eruption rate (or at least the eruption and deposition rate of ice grains in the plume) may have been higher in the past to be consistent with shorter eruption timescales (Martin et al., 2023). Modeling of the thermal evolution of Enceladus due to tidal stresses suggests that the ice shell may thicken and thin on ~100 Myr timescales, with a thinner shell favoring the formation of fissures through which plumes can erupt (Rudolph et al., 2022). Additionally, geochemical modeling suggests that serpentinization reactions in Enceladus's core can only persist for up to ~75 Myr, and thus might be reaching (or have already reached) the end of their productivity today even if Enceladus is young (Zandanel et al., 2021). It is unclear whether there is a direct link between the mechanisms powering hydrothermalism and plume eruption (though tidal forces likely play a key role for both (Berne et al., 2024; Hedman et al., 2013; C. Porco et al.,

2014; Schoenfeld & Yin, 2024)), but the studies described above have independently converged towards a view of Enceladus as a body that has only been dynamically active in the last ~10–100 Myr. A duration of 30–300 Myr from our modeling is consistent with this view.

A caveat to our and previous attempts to estimate the timescales of activity on Enceladus is that it is difficult to deconvolve *timescales* from the *rates* of plume or hydrothermal activity, which may be variable. Plume activity varies over diurnal and decadal timescales (Hansen et al., 2017; Hedman et al., 2013; Ingersoll et al., 2020; Nimmo et al., 2014; Teolis et al., 2017; Yeoh et al., 2017), but variation over geologic timescales is unknown. In our own modeling and in the studies described in the previous paragraph, continuous modern levels of plume eruption rate are assumed to be the norm. But what if we are witnessing an unusually dynamic moment in Enceladus's lifetime? For example, if the average rate of plume eruption over Enceladus's lifetime is only 10% of the rate we observe today, then plume eruption might have persisted over ~Gyr timescales. The converse argument can also be made, that higher amounts of activity in the past would imply shorter permissible timescales of eruption. A combined model of long-term plume eruption tied to the tidal and thermal evolution of Enceladus may help to resolve this degeneracy.

### *3.8. Summary & implications*

We modeled the long-term effects of sustained plume eruption on Enceladus's volatile chemistry to generate a range of possible histories of the levels of $CH_4$, $CO_2$, $NH_3$, and D/H ratios in the ocean. Our models demonstrate that $CH_4$ can be lost relatively quickly, while $CO_2$ and $NH_3$ are more easily retained and tend to suppress each other's loss due to their speciation into more soluble carbonate species and ammonium ions. The relative ease with which an oceanic reservoir of $CH_4$ is lost via the plume helps to explain why today $CH_4$ is the most depleted volatile relative to a cometary composition. Therefore, we find that a cometary starting composition is consistent

with the modern composition of the ocean if plume eruption has lasted long enough (~$10^7$–$10^8$ years) to fractionate gases from residual ocean water over time. Assuming comparable eruption rates to today, we constrain the total timescale of Enceladus's plume eruption to ~30–300 Myr. We expect that Enceladus's bulk D/H ratio has become lighter over time. While our reverse models of D/H allow for an initial comet-like D/H ratio, they do not help constrain the timescales of eruptive activity.

We have also shown that a steady state for Enceladus's ocean composition over geologic time is not a safe assumption. The present rates of $CH_4$ eruption are consistent with eruption of a primordial stock of $CH_4$ that has been mostly lost over time, with no need to invoke biology to explain $CH_4$'s presence in the plume or ocean today, unlike previous work (Affholder et al., 2021). However, biological production of $CH_4$ is not precluded by our model results.

Our models imply two possible endmembers for the early composition of Enceladus's ocean. In one, Enceladus's early ocean is saturated in $CO_2$ and acidic ($pH \geq 4$), due to a cometary budget of $CO_2$ that is primarily in the form of clathrates. In this scenario, the total ammonia in the early ocean is likely comparable to today (though additional $NH_4^+$ could be present in clays at the seafloor). In the other endmember, Enceladus's early ocean is basic ($pH \leq 12$) and rich in both $NH_3$ and $NH_4^+$. In this scenario, the early budget of Enceladus's $CO_2$ can only be consistent with a cometary composition if Enceladus's core contains abundant carbonate minerals (see (Glein & Waite, 2020). Although uncertainty in both the plume and ocean composition limits our ability to say which endmember is more likely, geochemical modeling of Enceladus's early composition from accretion onward favors the basic, $NH_3$-rich endmember (e.g., (Neveu et al., 2017). Further measurements to tighten constraints on the modern ocean composition, and especially on the

relative loss rates of $NH_3$ and $CO_2$, would reveal which of the two endmembers better represents Enceladus's early ocean chemistry.

The model we present here may be relevant to other icy ocean worlds if they also have sustained cryovolcanic activity. Our present view of the solar system is that Enceladus is unique among ocean worlds for its relatively constant plume eruption (Baum et al., 1981; Porco et al., 2006; Villanueva et al., 2023). Within a decade, the Europa Clipper mission seeks to confirm or refute the presence of plume-like activity at Europa, and constrain the composition and origin of these putative eruptions (Vance et al., 2023). If eruptions at Europa are similarly long-lived and connected to a liquid water reservoir, then our modeling approach may be applicable there too. Cryovolcanism may also be present and eventually observable on icy ocean worlds beyond our solar system (Quick et al., 2023), so the chemical evolution of these worlds due to sustained eruption is worth modeling as well, just as the effects of atmospheric escape on composition are investigated on terrestrial planets.

Our work adds to the picture of Enceladus as a dynamic and evolving body, where temporal variations of the ocean composition would affect abiotic chemistry and biological potential (see also Cockell et al., 2024). The early $NH_3$-rich endmember, for example, is an aquatic environment that may have favored production of amines (Liu et al., 2024), amino acids (Barge et al., 2020; Kebukawa et al., 2017; Koga & Naraoka, 2022; Pizzarello et al., 2011), and even peptides (Takahagi et al., 2019). Overall, our chemical model is consistent with geophysical models that suggest Enceladus has been active (eruptively and/or hydrothermally) only in the past ~$10^7$–$10^8$ Myr, and demonstrate that plume eruption helps explain Enceladus's evolution from a bulk cometary composition to today's state.

## 4. Materials and Methods

### *4.1. Volatile reverse evolution model*

We model the evolution of Enceladus's volatiles in reverse, starting from estimates for the modern ocean composition and going backwards in time. Gases in Enceladus's erupting plume are likely entirely lost to space, because their thermal velocities exceed the escape velocity (Hansen et al., 2006, 2020). Therefore, in the reverse model, the composition of the erupted plume is added back into the ocean, changing the ocean chemistry because the plume and ocean are likely not chemically identical (Fifer et al., 2022; Glein et al., 2015; Glein & Waite, 2020).

In the initial stage of our model, we use non-water gas eruption rates that were constrained by Cassini measurements, ~$10^9$ mol $yr^{-1}$ each for $CH_4$, $CO_2$, and $NH_3$, with the following variation between gases based on their measured mixing ratios (Waite et al., 2009, 2017). For $CH_4$, we use an initial eruption rate of $3.6\times10^8$–$1.1\times10^9$ mol $yr^{-1}$. We use a $CO_2$ eruption rate of $2.2\times10^9$ mol $yr^{-1}$, corresponding to a $CO_2$ mixing ratio of ~0.6 %, $H_2O$ mixing ratio of ~97 % (Waite et al., 2017), and overall vapor loss rates of ~200 kg $s^{-1}$ (Hansen et al., 2020). We explore possible initial $NH_3$:$CO_2$ loss ratios of 1:2, 1:1, 3:1, and intermediate values (reflecting uncertainty in plume measurements, the 3:1 case representing a higher $NH_3$ mixing ratio in the plume from Peter et al. (2023). At all other times in the model, the non-water gas eruption rates are scaled linearly from these initial (modern day, $t$=0) values based on the fractional change in aqueous concentration:

$$\phi_i(t) = \frac{b_i(t)}{b_i(t=0)}\phi_i(t=0) \quad (1)$$

Here, $\phi_i$ is the eruption rate (mol $yr^{-1}$) of any gas $i$, and $b_i$ is the molal concentration (mol $kg^{-1}$water) of gas $i$ in the ocean. Eruption rates and oceanic concentrations are a function of time, $t$ (yr). We note that there is significant uncertainty surrounding the exact mechanism(s) of plume eruption, and in particular the nature of the aqueous-to-gas phase transition (Mitchell et al., 2024). However,

in all proposed mechanisms, the eruption rate of an individual gas is linearly proportional to its concentration in the ocean, as in Equation (1). For example, in a model where the plume gas is produced by exsolution directly from an ocean surface, or exsolution into bubbles that burst at the ocean surface (Fifer et al., 2022), the exsolution rates (and ultimately the gas eruption rates) depend linearly on the aqueous concentrations, with higher concentrations leading to higher exsolution rates, and vice versa. In a model where the plume gas is produced primarily via degassing of aerosols (Glein & Waite, 2020; Klenner et al., 2025), the eruption rate is also linearly dependent on the aqueous concentration, because the concentrations of gases are preserved between the degassing droplets and the resulting gas phase. Modeling of ice shell melting induced by shear heating suggests that the plume could alternatively derive from an interstitial melt pocket instead of the ocean (Meyer et al., 2025). In that model, non-water components in the plume (e.g., salts, silica, and gases) can be explained if they were incorporated into an early ice shell during freezing, and later released during partial melting and eruption. However, the relationship between chemical abundances in the plume versus an interstitial melt source have yet to be explored. Therefore, in this work, we assume a direct link from ocean to plume.

For Enceladus's modern ocean, we use estimated dissolved gas and ion concentrations (Fifer et al., 2022; Glein & Waite, 2020; Waite et al., 2017), with additional restrictions on sodium ($Na^+$), chloride ($Cl^-$), bicarbonate ($HCO_3^-$) and carbonate ($CO_3^{2-}$) based on salts in the plume ice grains (Postberg et al., 2009). Generally, the uncertainty in oceanic concentrations is much greater than the uncertainty in eruption rates, due to ambiguity in how gases are fractionated during eruption (Fifer et al., 2022; Glein & Waite, 2020). Therefore, we vary the modern oceanic gas concentrations and eruption rates independently, to remain as agnostic as possible to different eruption and fractionation models. We base the modern Enceladus ocean chemistry primarily on

the gas-rich composition predicted by Fifer et al. (2022), but also expand our lower limits for initial $CH_4$, $CO_2$ and $NH_3$ by two orders of magnitude, to reflect the possibility of a less gas-rich modern ocean (e.g., Glein & Waite, 2020; Waite et al., 2017), with the caveat that we have included $NH_3$ where these models did not). Specifically we assume modern $[CH_4] = 1.1\times10^{-7}$–$6.4\times10^{-4}$ molal, $[CO_2] = 3.5\times10^{-7}$–$1.8\times10^{-3}$ molal, $[CO_3^{2-}] = 3\times10^{-3}$–$2\times10^{-1}$ molal, $[HCO_3^-] = 3.5\times10^{-5}$–$1.8\times10^{-3}$ molal, $[NH_3] = 9.8\times10^{-6}$–$7.2\times10^{-3}$ molal, $[NH_4^+] < 2\times10^{-1}$ molal, $[Na^+] = 0.06$–$0.3$ molal, $[Cl^-]$ = between (2/3) and (5/6) times $[Na^+]$. We assume a modern pH between 7.95–10.0 as a conservatively broad range that reflects recent estimates of 8.5–9.0 (Glein & Waite, 2020; Postberg et al., 2009), 8.5–10.5 (Hsu et al., 2015), and 7.95–9.05 (Fifer et al., 2022).

In our model, we assume that the eruption rate of water throughout Enceladus's history is equal to the modern eruption rate, $\approx 200$ kg $s^{-1}$ (Hansen et al., 2006, 2020). This is at least justified over decadal timescales, given the comparable eruption rates measured by Cassini in the early 2000s (Hansen et al., 2006, 2020), and by the James Webb Space Telescope (JWST) in 2022 (Villanueva et al., 2023). We explore the implications of this assumption and possible caveats in the Discussion section of this paper. We assume that any water that condenses onto the walls of the tiger stripe fissures (Nakajima & Ingersoll, 2016) is effectively recycled into the ocean, e.g., through subsidence and melting at the base of the fissure (Kite & Rubin, 2016), or dislodged ice falling back into the ocean (Pankine, 2023). Although the ice shell likely incorporates some non-water contaminants such as salts (Buffo et al., 2020, 2023; Naseem et al., 2023; Vance et al., 2021), for simplicity we assume that it is pure water-ice. We assume that this ice shell is 30-km thick with an outer shell diameter of 250 km (Hemingway et al., 2018).

In addition to dissolved, neutral gases (e.g., $NH_3$, $CO_2$), ionic species (e.g., $NH_4^+$, $CO_3^{2-}$, $HCO_3^-$) are a reservoir of volatiles in Enceladus's ocean. Unlike gases which exsolve readily,

dissolved ions will generally remain in solution or precipitate as salts upon ice grain formation (Postberg et al., 2009), and thus should not directly drive the exsolution rate of a given gas (Fifer et al., 2022). Nonetheless, ions are important to the long-term chemical evolution of Enceladus because they contribute to the net mass balance of volatiles, albeit not to exsolution rates.

To calculate chemical speciation between dissolved gases and related ions in the ocean, we use an equilibrium model of aqueous chemistry. Accounting for $CO_2$, $HCO_3^-$, $CO_3^{2-}$, $NH_3$, $NH_4^+$, $Na^+$, $Cl^-$, $H^+$, and $OH^-$ as the major aqueous species, we solve the following charge balance equation:

$$[Na^+] - [Cl^-] = [HCO_3^-] + 2[CO_3^{2-}] + [OH^-] - [H^+] - [NH_4^+]. \quad (2)$$

Here, each bracketed term represents the activity (≈ the molal concentration) of the dissolved ion. Given the definitions of dissolved inorganic carbon (DIC = $[CO_2] + [HCO_3^-] + [CO_3^{2-}]$) and total ammonia nitrogen (TAN = $[NH_3] + [NH_4^+]$), we can rewrite equation (2) in terms of DIC, TAN and equilibrium constants:

$$[Na^+] - [Cl^-] = \frac{DIC}{\left(\frac{[H^+]}{K_1} + 1 + \frac{K_2}{[H^+]}\right)} + 2\frac{DIC}{\left(\frac{[H^+]^2}{K_1 K_2} + \frac{[H^+]}{K_2} + 1\right)} + \frac{a_w K_w}{[H^+]} - [H^+] - \frac{TAN}{\left(1 + \frac{K_a}{[H^+]}\right)}. \quad (3)$$

Here, $K_1$ is the dissociation constant of $H_2CO_3$ into $HCO_3^-$ and $H^+$, $K_2$ is the dissociation constant of $HCO_3^-$ into $CO_3^{2-}$ and $H^+$, $K_w$ is the dissociation constant of water, and $a_w$ is water activity.

In our reverse model, at each timestep we add the appropriate moles of gas back into the ocean (based on gas eruption rates determined by equation (1)), and lost mass (kg) of water based on the constant eruption rate of water. At each timestep, we first calculate DIC, TAN and $[CH_4]$ based on the added gas and water from the plume, and then speciate DIC and TAN according to equation (3), using a numerical solver in Python to find the one unknown, $[H^+]$.

The total alkalinity of a solution can be defined by the difference between the concentrations of conservative cations and anions, all weighted by their charge (Wolf-Gladrow et al., 2007). In our case, total alkalinity is $[Na^+] - [Cl^-]$, eq. (2). Due to a lack of constraints on how the alkalinity or individual ion concentrations in Enceladus's ocean may have changed over time, we assume a constant value. We ignore the loss of $Na^+$ and $Cl^-$ via the plume because they should be lost at approximately the same rate, maintaining constant alkalinity. Additionally, the eruption of ice grains is a much less efficient loss mechanism than gas loss (see Section 3.5).

Although ions should not be preferentially lost due to plume eruption, they are susceptible to precipitation (which would lower the aqueous concentration) and dissolution (which would increase the aqueous concentration). Experimental work is ongoing to better characterize and simulate the mineral composition of Enceladus's rocky core, but there are limited observational constraints on that composition (Hamp et al., 2024). Therefore, we do not directly model water-rock redox reactions and their effect on aqueous composition. However, we do include possible salt mineral formation and precipitation using equilibrium constants. If the aqueous concentration of a particular salt (e.g., ammonium bicarbonate, $NH_4HCO_3$) becomes supersaturated during a model run, then the excess salt is immediately precipitated, and the aqueous concentration is restored to the solubility limit. Generally, the aqueous concentrations of volatiles and their associated ions increase (e.g., $NH_4^+$ or $HCO_3^-$) as our model moves *backwards* in time, which potentially induces supersaturation and precipitation. Thus, moving forward in time, the aqueous concentrations decrease as volatiles are removed from the ocean via the plume, and salts simultaneously dissolve to replace these lost volatiles, maintaining the aqueous concentration at the solubility limit until the solid reservoir of salts is exhausted.

Similar to the solid mineral phases described above, solid clathrate phases could be additional "hidden" reservoirs of volatiles that are reflected neither in the aqueous composition of the ocean nor the plume derived from the ocean. Adopting a similar approach to the one we take for salts, we induce clathrate formation in our model if the aqueous concentrations of *neutral* dissolved gases (e.g., $CO_2$, $CH_4$) exceed solubility limits. We adopt the maximum solubility limits compiled by Waite et al. (2009) (see Table S7 in the supplementary information of that paper). For example, if aqueous $CH_4$ begins to exceed $3 \times 10^{-3}$ mol per mol $H_2O$, then the excess $CH_4$ is relegated to a clathrate phase, and aqueous $CH_4$ is maintained at $3 \times 10^{-3}$ mol per mol $H_2O$. We do not include clathrates for $NH_3$ because $NH_3$ clathrates do not generally form in water, and $NH_3$-hydrates do not form at temperatures >273 K except at extremely high (>200 Mpa) pressures (Lunine & Stevenson, 1987), far beyond the ~5 Mpa pressures expected within Enceladus (Bouquet et al., 2015). It is possible that dissociating $CO_2$ and/or $CH_4$ clathrates make some contribution to the gas phase of the erupting plume (Bouquet et al., 2015; Choukroun et al., 2013; Fortes, 2007; Kieffer et al., 2006). Here we assume an indirect link, whereby clathrates can dissociate to produced dissolved gases, and these dissolved gases exsolve from the ocean to form the plume.

### *4.2. Deuterium/hydrogen (D/H) reverse evolution model*

We also consider the possible isotopic evolution of Enceladus's D/H ratio in water as a result of ongoing plume eruption, which we model under two different assumptions. In the first case, we assume that water vapor in the plume contains 100% light H and 0% heavy D, to model the most drastic possible D/H evolution, i.e., the maximum possible fractionating effect that ongoing eruption could have on the bulk D/H of Enceladus. In the second case, we assume

equilibrium fractionation between the plume vapor and the icy plume outlet, representing a more realistic and conservative estimate for long-term fractionation. For an outlet temperature of ~197 K (Goguen et al., 2013), the ice D/H will be heavier than the plume vapor D/H by a factor of ~1.33 (Lamb et al., 2017). At each timestep ($10^5$ years) in the reverse model, we recalculate the bulk D/H of the moon given plume loss, and recalculate the D/H of the plume given this equilibrium fractionation factor. In both the first case (maximum fractionation) and the second (equilibrium fractionation between plume and outlet), we initialize the model assuming a homogenous modern surface D/H between (1.3 to 2.8) × $10^{-4}$ (Clark et al., 2019). We do not distinguish between the D/H near the plume outlet versus the broader surface due to lack of empirical data on these distance scales, and we assume that the ocean D/H is approximately equal to that of the ice shell. For further discussion of these assumptions, see Section 3.6.

All source code used in this work is freely available on Zenodo:
https://doi.org/10.5281/zenodo.14957448

# Chapter 5: Conclusion

The plume of Enceladus presents a unique opportunity to study the subsurface ocean, but as a proxy it is only as robust as our understanding of the processes that produce it and modify it chemically. In my thesis work, I set out to elucidate these fractionation processes through modeling and laboratory experiments. This work has demonstrated the need for (and benefit of) treating this clearly physically dynamic moon as chemically dynamic too, both on immediate and geological timescales.

In Chapter 2, we develop a numerical model of plume eruption that couples existing models of water vapor eruption and condensation to new models of gas exsolution and chemical fractionation. This work fills a gap in the literature by exploring in detail the chemical implications of physical eruption models that reproduce the plume mass fluxes and surface heat fluxes measured at Enceladus's south pole. We use this model to make new predictions for the gas content in the ocean, finding relatively high (up to ~$10^{-3}$ molal) gas concentrations, higher than other recent estimates that may have overestimated the role of vapor condensation as a fractionating process. We also model aqueous speciation in the ocean to find an ocean pH of ~8-9, less alkaline than other estimates and potentially beneficial for Earth-like life, or at least our ability to understand Enceladus's ocean by analogy to our own. We show how chemical fractionation can change estimates for chemical free energy in the ocean and find that our updated gas concentrations would still produce sufficient free energy for methanogenic life. Finally, we evaluate the bulk abundances of volatiles, finding an ammonium-rich ocean that corroborates the hypothesis that Enceladus accreted from Jupiter family comet-like building blocks. At the same time, we find a bulk abundance for methane that is at least two orders of magnitude lower than cometary levels, posing a mystery that we return to in Chapter 4.

In Chapter 3, we use laboratory analog experiments to get an up-close look at how gases exsolve to form the Enceladus plume. These experiments are key to testing the validity of the numerical models developed in Chapter 2, which relied on theories and coefficients of mass transfer developed for terrestrial conditions. We measure the coefficients of mass transfer associated with two exsolving gases, $CO_2$ and $N_2$, for the first time under Enceladus-relevant temperatures and pressures. We find that $CO_2$ exsolution under Enceladus conditions is well-described by thin film thicknesses and mass transfer coefficients previously determined for ocean-atmosphere exchange on Earth. However, we find that $N_2$'s mass transfer coefficient is ~1 order of magnitude greater than predicted, perhaps due to enhanced mass transfer via bubbles. Our findings suggest that insoluble gases like $N_2$ and $H_2$ could be at lower concentrations in the Enceladus ocean than our estimates from Chapter 2.

In Chapter 4, we consider the fractionating ocean-plume system and ask – what happens if you run this process over deep time? We model long-term plume eruption and the resulting changes to ocean chemistry in reverse, and find that eruptions over 30-300 Myrs can reconcile an accreted comet-like composition with Enceladus's modern bulk volatile abundances from Chapter 2, included the depleted methane reservoir. This suggests that the methane fluxes observed in the plume by Cassini do not require a biological explanation, but are perfectly consistent with long-term loss of an initial cometary stock of methane. We also find that interactions between carbon dioxide and ammonia and their respective speciation leads to two mutually exclusive early endmembers: basic and ammonia-rich or acidic and carbon dioxide-rich. Prior forward modeling of Enceladus's formation, and measurements of the plume flux ratios both favor the basic and ammonia-rich early endmember, which could have favored prebiotic formation of key molecules like amino acids.

The work compiled here represents a step towards understanding the complexities of the ocean-plume connection on Enceladus, but there are many unanswered questions where additional research is needed. A recent publication has reevaluated the mass spectral data of the gas phase of Enceladus's plume (Peter et al., 2023). Of particular note is the newly confirmed detection of hydrogen cyanide, a key prebiotic molecule. The implications of this detection for ocean chemistry have not yet been explored, and we are beginning to work on expanding the model of Chapter 2 (Fifer et al., 2022) to include this wider list of species. Our experiments and apparatus also create many avenues of research to explore, including the exsolution of gas mixtures, exsolution in the presence of organics, and a thorough investigation of the role of bubbles in low pressure gas transfer. While working on this thesis, new models of plume eruption have emerged in the literature, including a hydrogen-driven ascent model (Mitchell et al., 2024) and a model where plumes are sourced not from the ocean directly, but an interstitial "mushy" ice source (Meyer et al., 2025). The implications of these models for fractionation in the plume, the detailed chemistry of their sources, and the long-term evolution of these systems present exciting opportunities for future research.

This work has been informed, inspired, and motivated by both past and potential future missions to Enceladus. This research is only possible thanks to the groundbreaking observations by the Cassini mission, and the immense amount of work in the intervening years by the mission team and the broader scientific community to uncover Enceladus's secrets. The goal of the work presented here has always been to contribute to that larger effort, to better understand what Cassini can still tell us, and to be prepared for future missions as well. Our intent is to lay the groundwork for interpretation of future missions to Enceladus, to increase the potential scientific return by demystifying the ocean-plume connection, and establish what parameters (e.g., ice fissure

geometry, chemical and isotopic ratios in the plume) could be measured to make that complex, fractionating system even clearer.

# Funding Sources

This work was supported by NASA grants #80NSSC19K0311 and #80NSSC21K1944. This work was supported by the UW ESS Robert and Jenny Winglee Endowed Graduate Support Fund and Space Physics Fellowship.

# Bibliography

**This bibliography excludes references from Chapter 2, as those references are contained within the chapter as presented in its published form.**

Affholder, A., Guyot, F., Sauterey, B., Ferrière, R., & Mazevet, S. (2021). Bayesian analysis of Enceladus's plume data to assess methanogenesis. *Nature Astronomy*, *5*(8), 805–814. https://doi.org/10.1038/s41550-021-01372-6

Alshameri, A., He, H., Zhu, J., Xi, Y., Zhu, R., Ma, L., & Tao, Q. (2018). Adsorption of ammonium by different natural clay minerals: Characterization, kinetics and adsorption isotherms. *Applied Clay Science*, *159*(August 2017), 83–93. https://doi.org/10.1016/j.clay.2017.11.007

Altwegg, K., Balsiger, H., Bar-Nun, A., Berthelier, J. J., Bieler, A., Bochsler, P., Briois, C., Calmonte, U., Combi, M., De Keyser, J., Eberhardt, P., Fiethe, B., Fuselier, S., Gasc, S., Gombosi, T. I., Hansen, K. C., Hässig, M., Jäckel, A., Kopp, E., … Wurz, P. (2015). 67P/Churyumov-Gerasimenko, a Jupiter family comet with a high D/H ratio. *Science*, *347*(6220), 4–6. https://doi.org/10.1126/science.1261952

Altwegg, K., Balsiger, H., Hänni, N., Rubin, M., Schuhmann, M., Schroeder, I., Sémon, T., Wampfler, S., Berthelier, J. J., Briois, C., Combi, M., Gombosi, T. I., Cottin, H., De Keyser, J., Dhooghe, F., Fiethe, B., & Fuselier, S. A. (2020). Evidence of ammonium salts in comet 67P as explanation for the nitrogen depletion in cometary comae. *Nature Astronomy*, *4*(5), 533–540. https://doi.org/10.1038/s41550-019-0991-9

Amsler Moulanier, A., Mousis, O., Bouquet, A., & Glein, C. R. (2025). The Role of Ammonia in the Distribution of Volatiles in the Primordial Hydrosphere of Europa. *The Planetary Science Journal*, *6*(1), 1. https://doi.org/10.3847/PSJ/ad9925

Aroniada, M., Maina, S., Koutinas, A., & Kookos, I. K. (2020). Estimation of volumetric mass transfer coefficient (kLa)—Review of classical approaches and contribution of a novel methodology. *Biochemical Engineering Journal*, *155*(October 2019). https://doi.org/10.1016/j.bej.2019.107458

Barge, L. M., Flores, E., VanderVelde, D. G., Weber, J. M., Baum, M. M., & Castonguay, A. (2020). Effects of Geochemical and Environmental Parameters on Abiotic Organic Chemistry Driven by Iron Hydroxide Minerals. *Journal of Geophysical Research: Planets*, *125*(11), 1–12. https://doi.org/10.1029/2020JE006423

Baum, W. A., Kreidl, T., Westphal, J. A., Danielson, G. E., Seidelmann, P. K., Pascu, D., & Currie, D. G. (1981). Saturn's E ring. *Icarus*, *47*(1), 84–96. https://doi.org/10.1016/0019-1035(81)90093-2

Belgodere, C., Dubessy, J., Vautrin, D., Caumon, M. C., Sterpenich, J., Pironon, J., Robert, P., Randi, A., & Birat, J. P. (2015). Experimental determination of CO2 diffusion coefficient in aqueous solutions under pressure at room temperature via Raman spectroscopy: Impact of salinity (NaCl). *Journal of Raman Spectroscopy*, *46*(10), 1025–1032. https://doi.org/10.1002/jrs.4742

Berne, A., Simons, M., Keane, J. T., Leonard, E. J., & Park, R. S. (2024). Jet activity on Enceladus linked to tidally driven strike-slip motion along tiger stripes. *Nature Geoscience*, *17*(5), 385–391. https://doi.org/10.1038/s41561-024-01418-0

Bouquet, A., Glein, C. R., & Waite, J. H. (2019). How Adsorption Affects the Gas–Ice Partitioning of Organics Erupted from Enceladus. *The Astrophysical Journal*, *873*(1), 28. https://doi.org/10.3847/1538-4357/ab0100

Bouquet, A., Mousis, O., Waite, J. H., & Picaud, S. (2015). Possible evidence for a methane source in Enceladus' ocean. *Geophysical Research Letters*, *42*(5), 1334–1339. https://doi.org/10.1002/2014GL063013

Broecker, W. S., & Peng, T. H. (1982). *Tracers in the Sea*. Lamont-Doherty Geological Observatory of Columbia University. https://doi.org/10.1016/0016-7037(83)90075-3

Buffett, B. A. (2000). Clathrate Hydrates. *Annual Review of Earth and Planetary Sciences*, *28*(1), 477–507. https://doi.org/10.1146/annurev.earth.28.1.477

Buffo, J. J., Meyer, C. R., Chivers, C. J., Walker, C. C., Huber, C., & Schmidt, B. E. (2023). Geometry of Freezing Impacts Ice Composition: Implications for Icy Satellites. *Journal of Geophysical Research: Planets*, *128*(3). https://doi.org/10.1029/2022JE007389

Buffo, J. J., Schmidt, B. E., Huber, C., & Walker, C. C. (2020). Entrainment and Dynamics of Ocean-Derived Impurities Within Europa's Ice Shell. *Journal of Geophysical Research: Planets*, *125*(10), 1–23. https://doi.org/10.1029/2020JE006394

Cable, M. L., Porco, C., Glein, C. R., German, C. R., MacKenzie, S. M., Neveu, M., Hoehler, T. M., Hofmann, A. E., Hendrix, A. R., Eigenbrode, J., Postberg, F., Spilker, L. J., McEwen, A., Khawaja, N., Waite, J. H., Wurz, P., Helbert, J., Anbar, A., Vera, J. P. De, & Núñez, J. (2021). The Science Case for a Return to Enceladus. *Planetary Science Journal*, *2*(4), 132. https://doi.org/10.3847/PSJ/abfb7a

Cappa, C. D., Hendricks, M. B., DePaolo, D. J., & Cohen, R. C. (2003). Isotopic fractionation of water during evaporation. *Journal of Geophysical Research*, *108*(D16), 4525. https://doi.org/10.1029/2003JD003597

Carpenter, L. J., Archer, S. D., & Beale, R. (2012). Ocean-atmosphere trace gas exchange. *Chemical Society Reviews*, *41*(19), 6473–6506. https://doi.org/10.1039/c2cs35121h

Castillo-Rogez, J. C., Daswani, M. M., Glein, C. R., Vance, S. D., & Cochrane, C. J. (2022). Contribution of Non-Water Ices to Salinity and Electrical Conductivity in Ocean Worlds. *Geophysical Research Letters*, *49*(16). https://doi.org/10.1029/2021GL097256

Castillo-Rogez, J., Glein, C., Courville, S., Melwani Daswani, M., Castillo-Rogez, J., Glein, C., Courville, S., & Melwani Daswani, M. (2023). Internal Evolution and Current State of Enceladus Accreted from Cometary Material. *55th Annual Meeting of the Division for Planetary Sciences*, *55*(8), 313.02. https://ui.adsabs.harvard.edu/abs/2023DPS....5531302C/abstract

Choukroun, M., Kieffer, S. W., Lu, X., & Tobie, G. (2013). Clathrate Hydrates: Implications for Exchange Processes in the Outer Solar System. In M. S. Gudipati & J. Castillo-Rogez (Eds.), *The Science of Solar System Ices* (Vol. 356, pp. 409–454). Springer New York. https://doi.org/10.1007/978-1-4614-3076-6_12

Clark, R. N., Brown, R. H., Cruikshank, D. P., & Swayze, G. A. (2019). Isotopic ratios of Saturn's rings and satellites: Implications for the origin of water and Phoebe. *Icarus*, *321*(November 2018), 791–802. https://doi.org/10.1016/j.icarus.2018.11.029

Cockell, C. S., Simons, M., Castillo-Rogez, J., Higgins, P. M., Kaltenegger, L., Keane, J. T., Leonard, E. J., Mitchell, K. L., Park, R. S., Perl, S. M., & Vance, S. D. (2024). Sustained

and comparative habitability beyond Earth. *Nature Astronomy*, *8*(1), 30–38. https://doi.org/10.1038/s41550-023-02158-8

Ćuk, M., Dones, L., & Nesvorný, D. (2016). Dynamical Evidence for a Late Formation of Saturn'S Moons. *The Astrophysical Journal*, *820*(2), 97. https://doi.org/10.3847/0004-637x/820/2/97

Cussler, E. L. (2009). *Diffusion: mass transfer in fluid systems* (3rd ed.). Cambridge University Press.

Estrada, P. R., & Durisen, R. H. (2023). Constraints on the initial mass, age and lifetime of Saturn's rings from viscous evolutions that include pollution and transport due to micrometeoroid bombardment. *Icarus*, *400*(September 2022), 115296. https://doi.org/10.1016/j.icarus.2022.115296

Fifer, L. M., Catling, D. C., & Toner, J. D. (2022). Chemical Fractionation Modeling of Plumes Indicates a Gas-rich, Moderately Alkaline Enceladus Ocean. *The Planetary Science Journal*, *3*(8), 191. https://doi.org/10.3847/PSJ/ac7a9f

Fortes, A. D. (2007). Metasomatic clathrate xenoliths as a possible source for the south polar plumes of Enceladus. *Icarus*, *191*(2), 743–748. https://doi.org/10.1016/j.icarus.2007.06.013

Fox-Powell, M. G., & Cousins, C. R. (2021). Partitioning of Crystalline and Amorphous Phases During Freezing of Simulated Enceladus Ocean Fluids. *Journal of Geophysical Research: Planets*, *126*(1), 1–16. https://doi.org/10.1029/2020JE006628

Fuller, J., Luan, J., & Quataert, E. (2016). Resonance locking as the source of rapid tidal migration in the Jupiter and Saturn moon systems. *Monthly Notices of the Royal Astronomical Society*, *458*(4), 3867–3879. https://doi.org/10.1093/mnras/stw609

Gainey, S. R., & Elwood Madden, M. E. (2012). Kinetics of methane clathrate formation and dissociation under Mars relevant conditions. *Icarus*, *218*(1), 513–524. https://doi.org/10.1016/j.icarus.2011.12.019

Gålfalk, M., Bastviken, D., Fredriksson, S., & Arneborg, L. (2013). Determination of the piston velocity for water-air interfaces using flux chambers, acoustic Doppler velocimetry, and IR imaging of the water surface. *Journal of Geophysical Research: Biogeosciences*, *118*(2), 770–782. https://doi.org/10.1002/jgrg.20064

Glein, C. R., Baross, J. A., & Waite, J. H. (2015). The pH of Enceladus' ocean. *Geochimica et Cosmochimica Acta*, *162*, 202–219. https://doi.org/10.1016/j.gca.2015.04.017

Glein, C. R., Postberg, F., & Vance, S. D. (2018). The Geochemistry of Enceladus: Composition and Controls. In *Enceladus and the Icy Moons of Saturn* (Vol. 57, Issue 3, pp. 439–448). The University of Arizona Press. https://doi.org/10.2458/azu_uapress_9780816537075-ch003

Glein, C. R., & Waite, J. H. (2020). The Carbonate Geochemistry of Enceladus' Ocean. *Geophysical Research Letters*, *47*(3), 1689–1699. https://doi.org/10.1029/2019GL085885

Goguen, J. D., Buratti, B. J., Brown, R. H., Clark, R. N., Nicholson, P. D., Hedman, M. M., Howell, R. R., Sotin, C., Cruikshank, D. P., Baines, K. H., Lawrence, K. J., Spencer, J. R., & Blackburn, D. G. (2013). The temperature and width of an active fissure on Enceladus measured with Cassini VIMS during the 14 April 2012 South Pole flyover. *Icarus*, *226*(1), 1128–1137. https://doi.org/10.1016/j.icarus.2013.07.012

Hamp, R. E., Olsson-Francis, K., Schwenzer, S. P., & Pearson, V. K. (2024). An inorganic silicate simulant to represent the interior of enceladus. *Planetary and Space Science*, *248*(July), 105934. https://doi.org/10.1016/j.pss.2024.105934

Hansen, C. J., Esposito, L., Stewart, A. I. F., Colwell, J., Hendrix, A., Pryor, W., Shemansky, D., & West, R. (2006). Enceladus' Water Vapor Plume. *Science*, *311*(5766), 1422–1425. https://doi.org/10.1126/science.1121254

Hansen, C. J., Esposito, L. W., Aye, K. M., Colwell, J. E., Hendrix, A. R., Portyankina, G., & Shemansky, D. (2017). Investigation of diurnal variability of water vapor in Enceladus' plume by the Cassini ultraviolet imaging spectrograph. *Geophysical Research Letters*, *44*(2), 672–677. https://doi.org/10.1002/2016GL071853

Hansen, C. J., Esposito, L. W., Colwell, J. E., Hendrix, A. R., Portyankina, G., Stewart, A. I. F., & West, R. A. (2020). The composition and structure of Enceladus' plume from the complete set of Cassini UVIS occultation observations. *Icarus*, *344*, 113461. https://doi.org/10.1016/j.icarus.2019.113461

Hao, J., Glein, C. R., Huang, F., Yee, N., Catling, D. C., Postberg, F., Hillier, J. K., & Hazen, R. M. (2022). Abundant phosphorus expected for possible life in Enceladus's ocean. *Proceedings of the National Academy of Sciences*, *119*(39), 1–9. https://doi.org/10.1073/pnas.2201388119

Hedman, M. M., Dhingra, D., Nicholson, P. D., Hansen, C. J., Portyankina, G., Ye, S., & Dong, Y. (2018). Spatial variations in the dust-to-gas ratio of Enceladus' plume. *Icarus*, *305*, 123–138. https://doi.org/10.1016/j.icarus.2018.01.006

Hedman, M. M., Gosmeyer, C. M., Nicholson, P. D., Sotin, C., Brown, R. H., Clark, R. N., Baines, K. H., Buratti, B. J., & Showalter, M. R. (2013). An observed correlation between plume activity and tidal stresses on Enceladus. *Nature*, *500*(7461), 182–184. https://doi.org/10.1038/nature12371

Hemingway, D., Iess, L., Tadjeddine, R., & Tobie, G. (2018). The Interior of Enceladus. In *Enceladus and the Icy Moons of Saturn* (Vol. 57, Issue 3, pp. 439–448). The University of Arizona Press. https://doi.org/10.2458/azu_uapress_9780816537075-ch004

Hendrix, A. R., Hurford, T. A., Barge, L. M., Bland, M. T., Bowman, J. S., Brinckerhoff, W., Buratti, B. J., Cable, M. L., Castillo-Rogez, J., Collins, G. C., Diniega, S., German, C. R., Hayes, A. G., Hoehler, T., Hosseini, S., Howett, C. J. A., McEwen, A. S., Neish, C. D., Neveu, M., … Vance, S. D. (2019). The NASA Roadmap to Ocean Worlds. *Astrobiology*, *19*(1), 1–27. https://doi.org/10.1089/ast.2018.1955

Higgins, P. M., Chen, W., Glein, C. R., Cockell, C. S., & Sherwood Lollar, B. (2024). Quantifying Uncertainty in Sustainable Biomass and Production of Biotic Carbon in Enceladus' Notional Methanogenic Biosphere. *Journal of Geophysical Research: Planets*, *129*(3). https://doi.org/10.1029/2023JE008166

Hirata, N., Miyamoto, H., & Showman, A. P. (2014). Particle deposition on the saturnian satellites from ephemeral cryovolcanism on Enceladus. *Geophysical Research Letters*, *41*(12), 4135–4141. https://doi.org/10.1002/2014GL060470

Hsu, H. W., Postberg, F., Sekine, Y., Shibuya, T., Kempf, S., Horányi, M., Juhász, A., Altobelli, N., Suzuki, K., Masaki, Y., Kuwatani, T., Tachibana, S., Sirono, S. I., Moragas-Klostermeyer, G., & Srama, R. (2015). Ongoing hydrothermal activities within Enceladus. *Nature*, *519*(7542), 207–210. https://doi.org/10.1038/nature14262

Hyodo, R., Genda, H., & Madeira, G. (2025). Pollution resistance of Saturn's ring particles during micrometeoroid impact. *Nature Geoscience*, *18*(1), 44–49. https://doi.org/10.1038/s41561-024-01598-9

Ingersoll, A. P., Ewald, S. P., & Trumbo, S. K. (2020). Time variability of the Enceladus plumes: Orbital periods, decadal periods, and aperiodic change. *Icarus*, *344*(June 2019), 113345. https://doi.org/10.1016/j.icarus.2019.06.006

Ingersoll, A. P., & Nakajima, M. (2016). Controlled boiling on Enceladus. 2. Model of the liquid-filled cracks. *Icarus*, *272*, 319–326. https://doi.org/10.1016/j.icarus.2015.12.040

Karimi, A., Golbabaei, F., Mehrnia, M. R., Neghab, M., Mohammad, K., Nikpey, A., & Pourmand, M. R. (2013). Oxygen mass transfer in a stirred tank bioreactor using different impeller configurations for environmental purposes. *Iranian Journal of Environmental Health Science and Engineering*, *10*(6), 1. https://doi.org/10.1186/1735-2746-10-6

Kebukawa, Y., Chan, Q. H. S., Tachibana, S., Kobayashi, K., & Zolensky, M. E. (2017). One-pot synthesis of amino acid precursors with insoluble organic matter in planetesimals with aqueous activity. *Science Advances*, *3*(3), 1–7. https://doi.org/10.1126/sciadv.1602093

Kempf, S., Altobelli, N., Schmidt, J., Cuzzi, J. N., Estrada, P. R., & Srama, R. (2023). Micrometeoroid infall onto Saturn's rings constrains their age to no more than a few hundred million years. *Science Advances*, *9*(19), 2–7. https://doi.org/10.1126/sciadv.adf8537

Kharecha, P., Kasting, J., & Siefert, J. (2005). A coupled atmosphere–ecosystem model of the early Archean Earth. *Geobiology*, *3*(2), 53–76. https://doi.org/10.1111/j.1472-4669.2005.00049.x

Khawaja, N., Postberg, F., Hillier, J., Klenner, F., Kempf, S., Nölle, L., Reviol, R., Zou, Z., & Srama, R. (2019). Low-mass nitrogen-, oxygen-bearing, and aromatic compounds in Enceladean ice grains. *Monthly Notices of the Royal Astronomical Society*, *489*(4), 5231–5243. https://doi.org/10.1093/mnras/stz2280

Kieffer, S. W., Lu, X., Bethke, C. M., Spencer, J. R., Marshak, S., & Navrotsky, A. (2006). A clathrate reservoir hypothesis for enceladus south polar plume. *Science*, *314*(5806), 1764–1766. https://doi.org/10.1126/science.1133519

Kite, E. S., & Rubin, A. M. (2016). Sustained eruptions on Enceladus explained by turbulent dissipation in tiger stripes. *Proceedings of the National Academy of Sciences*, *113*(15), 3972–3975. https://doi.org/10.1073/pnas.1520507113

Klenner, F., Fifer, L. M., Journaux, B., Bravenec, A. D., Leal, A. M. M., Vance, S. D., & Catling, D. C. (2025). Supercooling, Glass Formation, and Mineral Assemblages upon Freezing of Salty Ice Grains from Enceladus's Ocean. *The Planetary Science Journal*, *6*(3), 65. https://doi.org/10.3847/PSJ/adb305

Koga, T., & Naraoka, H. (2022). Synthesis of Amino Acids from Aldehydes and Ammonia: Implications for Organic Reactions in Carbonaceous Chondrite Parent Bodies. *ACS Earth and Space Chemistry*, *6*(5), 1311–1320. https://doi.org/10.1021/acsearthspacechem.2c00008

Lainey, V., Casajus, L. G., Fuller, J., Zannoni, M., Tortora, P., Cooper, N., Murray, C., Modenini, D., Park, R. S., Robert, V., & Zhang, Q. (2020). Resonance locking in giant planets indicated by the rapid orbital expansion of Titan. *Nature Astronomy*, *4*(11), 1053–1058. https://doi.org/10.1038/s41550-020-1120-5

Lamb, K. D., Clouser, B. W., Bolot, M., Sarkozy, L., Ebert, V., Saathoff, H., Möhler, O., & Moyer, E. J. (2017). Laboratory measurements of HDO/H2O isotopic fractionation during ice deposition in simulated cirrus clouds. *Proceedings of the National Academy of Sciences*, *114*(22), 5612–5617. https://doi.org/10.1073/pnas.1618374114

Lee, J., Yasin, M., Park, S., Chang, I. S., Ha, K. S., Lee, E. Y., Lee, J., & Kim, C. (2015). Gas-liquid mass transfer coefficient of methane in bubble column reactor. *Korean Journal of Chemical Engineering*, *32*(6), 1060–1063. https://doi.org/10.1007/s11814-014-0341-7

Liger-Belair, G. (2012). The physics behind the fizz in champagne and sparkling wines. *European Physical Journal: Special Topics*, *201*(1), 1–88. https://doi.org/10.1140/epjst/e2012-01528-0

Liger-Belair, G., & Cilindre, C. (2021). Recent Progress in the Analytical Chemistry of Champagne and Sparkling Wines. *Annual Review of Analytical Chemistry*, *14*, 21–46. https://doi.org/10.1146/annurev-anchem-061318-115018

Lippi, M., Villanueva, G. L., Mumma, M. J., & Faggi, S. (2021). Investigation of the Origins of Comets as Revealed through Infrared High-resolution Spectroscopy I. Molecular Abundances. *The Astronomical Journal*, *162*(2), 74. https://doi.org/10.3847/1538-3881/abfdb7

Liss, P. S., & Johnson, M. T. (2014). Ocean-atmosphere interactions of gases and particles. In *Ocean-Atmosphere Interactions of Gases and Particles*. https://doi.org/10.1007/978-3-642-25643-1

Liss, P. S., & Slater, P. G. (1974). Flux of gases across the Air-Sea interface. *Nature*, *247*(5438), 181–184. https://doi.org/10.1038/247181a0

Liu, C., Xu, W., Zhang, Z., Robinson, K., Lau, M., Huang 黄, F. 放, Huang 黄, F. 方, Glein, C. R., & Hao, J. (2024). The Potential for Organic Synthesis in the Ocean of Enceladus. *The Astrophysical Journal*, *971*(1), 51. https://doi.org/10.3847/1538-4357/ad534f

Lunine, J. I., & Stevenson, D. J. (1987). Clathrate and ammonia hydrates at high pressure: Application to the origin of methane on Titan. *Icarus*, *70*(1), 61–77. https://doi.org/10.1016/0019-1035(87)90075-3

Lynch, D. M., & Bamforth, C. W. (2002). Measurement and characterization of bubble nucleation in beer. *Journal of Food Science*, *67*(7), 2696–2701. https://doi.org/10.1111/j.1365-2621.2002.tb08801.x

MacKenzie, S. M., Neveu, M., Davila, A. F., Lunine, J. I., Cable, M. L., Phillips-Lander, C. M., Eigenbrode, J. L., Waite, J. H., Craft, K. L., Hofgartner, J. D., McKay, C. P., Glein, C. R., Burton, D., Kounaves, S. P., Mathies, R. A., Vance, S. D., Malaska, M. J., Gold, R., German, C. R., … Heldmann, J. (2022). Science Objectives for Flagship-Class Mission Concepts for the Search for Evidence of Life at Enceladus. *Astrobiology*, *22*(6), 685–712. https://doi.org/10.1089/ast.2020.2425

Magee, B. A., & Waite, J. H. (2017). Neutral Gas Composition of Enceladus' Plume – Model Parameter Insights from Cassini-INMS. *Lunar and Planetary Science XLVIII*, 2–3.

Mandt, K. E., Lustig-Yaeger, J., Luspay-Kuti, A., Wurz, P., Bodewits, D., Fuselier, S. A., Mousis, O., Petrinec, S. M., & Trattner, K. J. (2024). A nearly terrestrial D/H for comet 67P/Churyumov-Gerasimenko. *Science Advances*, *10*(46), 1–11. https://doi.org/10.1126/sciadv.adp2191

Manga, M., & Wang, C. Y. (2007). Pressurized oceans and the eruption of liquid water on Europa and Enceladus. *Geophysical Research Letters*, *34*(7), 1–5. https://doi.org/10.1029/2007GL029297

Martin, E. S., Kattenhorn, S. A., Collins, G. C., Michaud, R. L., Pappalardo, R. T., & Wyrick, D. Y. (2017). Pit chains on Enceladus signal the recent tectonic dissection of the ancient cratered terrains. *Icarus*, *294*, 209–217. https://doi.org/10.1016/j.icarus.2017.03.014

Martin, E. S., Whitten, J. L., Kattenhorn, S. A., Collins, G. C., Southworth, B. S., Wiser, L. S., & Prindle, S. (2023). Measurements of regolith thicknesses on Enceladus: Uncovering the record of plume activity. *Icarus*, *392*(November 2022), 115369. https://doi.org/10.1016/j.icarus.2022.115369

Matson, D., Johnson, T., Lunine, J., & Castillo-Rogez, J. (2010). The "Perrier Oceans" of Europa and Enceladus (Invited). *AGU Fall Meeting Abstracts*. https://ui.adsabs.harvard.edu/abs/2010AGUFM.P24A..04M/abstract

Matson, D. L., Castillo-Rogez, J. C., Davies, A. G., & Johnson, T. V. (2012). Enceladus: A hypothesis for bringing both heat and chemicals to the surface. *Icarus*, *221*(1), 53–62. https://doi.org/10.1016/j.icarus.2012.05.031

McKay, C. P., Porco, C. C., Altheide, T., Davis, W. L., & Kral, T. A. (2008). The Possible Origin and Persistence of Life on Enceladus and Detection of Biomarkers in the Plume. *Astrobiology*, *8*(5), 909–919. https://doi.org/10.1089/ast.2008.0265

McKinnon, W. B., Waite, J. H., Mousis, O., Lunine, J. I., & Zolotov, M. Y. (2018). The Mysterious Origin of Enceladus: A Compositional Perspective. In *Enceladus and the Icy Moons of Saturn* (p. A1669). The University of Arizona Press. https://doi.org/10.2458/azu_uapress_9780816537075-ch002

Meyer, C. R., Buffo, J. J., Nimmo, F., Wells, A. J., Boury, S., Fox-Powell, M., Tomlinson, T. C., Parkinson, J. R. G., & Vasil, G. M. (2025). A Potential Mushy Source for the Geysers of Enceladus and Other Icy Satellites. *Geophysical Research Letters*, *52*(3). https://doi.org/10.1029/2024GL111929

Mitchell, K. L., Rabinovitch, J., Scamardella, J. C., & Cable, M. L. (2024). A Proposed Model for Cryovolcanic Activity on Enceladus Driven by Volatile Exsolution. *Journal of Geophysical Research: Planets*, *129*(7), 1–32. https://doi.org/10.1029/2023JE007977

Mizutani, T., Takano, T., & Ogoshi, H. (1995). Selectivity of Adsorption of Organic Ammonium Ions onto Smectite Clays. *Langmuir*, *11*(3), 880–884. https://doi.org/10.1021/la00003a033

Montes, F., Rotz, C. A., & Chaoui, H. (2009). Process Modeling of Ammonia Volatilization from Ammonium Solution and Manure Surfaces: A Review with Recommended Models. *Transactions of the ASABE*, *52*(5), 1707–1719. https://doi.org/10.13031/2013.29133

Mumma, M. J., & Charnley, S. B. (2011). The chemical composition of comets - emerging taxonomies and natal heritage. *Annual Review of Astronomy and Astrophysics*, *49*, 471–524. https://doi.org/10.1146/annurev-astro-081309-130811

Nakajima, M., & Ingersoll, A. P. (2016). Controlled boiling on Enceladus. 1. Model of the vapor-driven jets. *Icarus*, *272*, 309–318. https://doi.org/10.1016/j.icarus.2016.02.027

Naseem, M., Neveu, M., Howell, S., Lesage, E., Melwani Daswani, M., & Vance, S. D. (2023). Salt Distribution from Freezing Intrusions in Ice Shells on Ocean Worlds: Application to Europa. *Planetary Science Journal*, *4*(9). https://doi.org/10.3847/PSJ/ace5a2

Neveu, M., Desch, S. J., & Castillo-Rogez, J. C. (2017). Aqueous geochemistry in icy world interiors: Equilibrium fluid, rock, and gas compositions, and fate of antifreezes and radionuclides. *Geochimica et Cosmochimica Acta*, *212*, 324–371. https://doi.org/10.1016/j.gca.2017.06.023

Neveu, M., & Rhoden, A. R. (2019). Evolution of Saturn's mid-sized moons. *Nature Astronomy*, *3*(6), 543–552. https://doi.org/10.1038/s41550-019-0726-y

Ni, J. (1999). Mechanistic models of ammonia release from liquid manure: A review. *Journal of Agricultural and Engineering Research*, *72*(1), 1–17. https://doi.org/10.1006/jaer.1998.0342

Nimmo, F., Barr, A. C., Běhounková, M., & McKinnon, W. B. (2018). The Thermal and Orbital Evolution of Enceladus: Observational Constraints and Models. In *Enceladus and the Icy Moons of Saturn* (Vol. 57, Issue 3, pp. 439–448). The University of Arizona Press. https://doi.org/10.2458/azu_uapress_9780816537075-ch005

Nimmo, F., Neveu, M., & Howett, C. (2023). Origin and Evolution of Enceladus's Tidal Dissipation. *Space Science Reviews*, *219*(7). https://doi.org/10.1007/s11214-023-01007-4

Nimmo, F., Porco, C., & Mitchell, C. (2014). Tidally modulated eruptions on Enceladus: Cassini ISS observations and models. *Astronomical Journal*, *148*(3). https://doi.org/10.1088/0004-6256/148/3/46

Nishimura, N., Kitaura, S., Mimura, A., & Takahara, Y. (1991). Growth of Thermophilic Methanogen KN-15 on H2-CO2 under Batch and Continuous Conditions. *Journal of Fermentation and Bioengineering*, *72*(4), 280–284.

Pankine, A. A. (2023). Numerical simulations of heat exchange and vapor flow in ice fractures on Enceladus. *Icarus*, *401*(March), 115584. https://doi.org/10.1016/j.icarus.2023.115584

Peter, J. S., Nordheim, T. A., & Hand, K. P. (2023). Detection of HCN and diverse redox chemistry in the plume of Enceladus. *Nature Astronomy*. https://doi.org/10.1038/s41550-023-02160-0

Pizzarello, S., Williams, L. B., Lehman, J., Holland, G. P., & Yarger, J. L. (2011). Abundant ammonia in primitive asteroids and the case for a possible exobiology. *Proceedings of the National Academy of Sciences of the United States of America*, *108*(11), 4303–4306. https://doi.org/10.1073/pnas.1014961108

Porco, C. C., Dones, L., & Mitchell, C. (2017). Could It Be Snowing Microbes on Enceladus? Assessing Conditions in Its Plume and Implications for Future Missions. *Astrobiology*. https://doi.org/10.1089/ast.2017.1665

Porco, C. C., Helfenstein, P., Thomas, P. C., Ingersoll, A. P., Wisdom, J., West, R., Neukum, G., Denk, T., Wagner, R., Roatsch, T., Kieffer, S., Turtle, E., McEwen, A., Johnson, T. V, Rathbun, J., Veverka, J., Wilson, D., Perry, J., Spitale, J., … Squyres, S. (2006). Cassini Observes the Active South Pole of Enceladus. *Science*, *311*(5766), 1393–1401. https://doi.org/10.1126/science.1123013

Porco, C., Dinino, D., & Nimmo, F. (2014). How the geysers, tidal stresses, and thermal emission across the south polar terrain of Enceladus are related. *Astronomical Journal*, *148*(3). https://doi.org/10.1088/0004-6256/148/3/45

Postberg, F., Kempf, S., Hillier, J. K., Srama, R., Green, S. F., McBride, N., & Grün, E. (2008). The E-ring in the vicinity of Enceladus. II. Probing the moon's interior - The composition of E-ring particles. *Icarus*, *193*(2), 438–454. https://doi.org/10.1016/j.icarus.2007.09.001

Postberg, F., Kempf, S., Schmidt, J., Brilliantov, N., Beinsen, A., Abel, B., Buck, U., & Srama, R. (2009). Sodium salts in E-ring ice grains from an ocean below the surface of Enceladus. *Nature*, *459*(7250), 1098–1101. https://doi.org/10.1038/nature08046

Postberg, F., Khawaja, N., Abel, B., Choblet, G., Glein, C. R., Gudipati, M. S., Henderson, B. L., Hsu, H.-W., Kempf, S., Klenner, F., Moragas-Klostermeyer, G., Magee, B., Nölle, L., Perry, M., Reviol, R., Schmidt, J., Srama, R., Stolz, F., Tobie, G., … Waite, J. H. (2018). Macromolecular organic compounds from the depths of Enceladus. *Nature*, *558*(7711), 564–568. https://doi.org/10.1038/s41586-018-0246-4

Postberg, F., Schmidt, J., Hillier, J., Kempf, S., & Srama, R. (2011). A salt-water reservoir as the source of a compositionally stratified plume on Enceladus. *Nature*, *474*(7353), 620–622. https://doi.org/10.1038/nature10175

Postberg, F., Sekine, Y., Klenner, F., Glein, C. R., Zou, Z., Abel, B., Furuya, K., Hillier, J. K., Khawaja, N., Kempf, S., Noelle, L., Saito, T., Schmidt, J., Shibuya, T., Srama, R., & Tan, S. (2023). Detection of phosphates originating from Enceladus's ocean. *Nature*, *618*(7965), 489–493. https://doi.org/10.1038/s41586-023-05987-9

Quick, L. C., Roberge, A., Mendoza, G. T., Quintana, E. V., & Youngblood, A. A. (2023). Prospects for Cryovolcanic Activity on Cold Ocean Planets. *The Astrophysical Journal*, *956*(1), 29. https://doi.org/10.3847/1538-4357/ace9b6

Randolph-Flagg, N. G., Ely, T., Som, S. M., Shock, E. L., German, C. R., & Hoehler, T. M. (2023). Phosphate availability and implications for life on ocean worlds. *Nature Communications*, *14*(1). https://doi.org/10.1038/s41467-023-37770-9

Retherford, K. D., Becker, T. M., Gladstone, G. R., Greathouse, T. K., Davis, M. W., Velez, M. A., Freeman, M. A., Brooks, S. M., Ferrell, S., Giles, R. S., Hendrix, A. R., Hue, V., Johnson, E., Kammer, J. A., Marinan, A. D., D Mamo, B., McGrath, M. A., Molyneux, P. M., Nerney, E. G., … Winkenstern, J. (2024). Europa Ultraviolet Spectrograph (Europa-UVS). *Space Science Reviews*, *220*(8), 89. https://doi.org/10.1007/s11214-024-01121-x

Reynard, B., & Sotin, C. (2023). Carbon-rich icy moons and dwarf planets. *Earth and Planetary Science Letters*, *612*, 118172. https://doi.org/10.1016/j.epsl.2023.118172

Rudolph, M. L., Manga, M., Walker, M., & Rhoden, A. R. (2022). Cooling Crusts Create Concomitant Cryovolcanic Cracks. *Geophysical Research Letters*, *49*(5), 1–11. https://doi.org/10.1029/2021GL094421

Sander, R. (2015). Compilation of Henry's law constants (version 4.0) for water as solvent. *Atmospheric Chemistry and Physics*, *15*(8), 4399–4981. https://doi.org/10.5194/acp-15-4399-2015

Schmidt, J., Brilliantov, N., Spahn, F., & Kempf, S. (2008). Slow dust in Enceladus' plume from condensation and wall collisions in tiger stripe fractures. *Nature*, *451*(7179), 685–688. https://doi.org/10.1038/nature06491

Schoenfeld, A. M., Hawkins, E. K., Soderlund, K. M., Vance, S. D., Leonard, E., & Yin, A. (2023). Particle entrainment and rotating convection in Enceladus' ocean. *Communications Earth and Environment*, *4*(1), 1–8. https://doi.org/10.1038/s43247-023-00674-z

Schoenfeld, A. M., & Yin, A. (2024). Quantifying tidal versus non-tidal stresses in driving time-varying fluxes of Enceladus' plume eruptions. *Icarus*, *415*(March), 116064. https://doi.org/10.1016/j.icarus.2024.116064

Schuhmann, M., Altwegg, K., Balsiger, H., Berthelier, J. J., De Keyser, J., Fiethe, B., Fuselier, S. A., Gasc, S., Gombosi, T. I., Hänni, N., Rubin, M., Tzou, C. Y., & Wampfler, S. F. (2019). Aliphatic and aromatic hydrocarbons in comet 67P/Churyumov-Gerasimenko seen by ROSINA. *Astronomy and Astrophysics*, *630*. https://doi.org/10.1051/0004-6361/201834666

Sekine, Y., Shibuya, T., Postberg, F., Hsu, H.-W., Suzuki, K., Masaki, Y., Kuwatani, T., Mori, M., Hong, P. K., Yoshizaki, M., Tachibana, S., & Sirono, S. (2015). High-temperature water–rock interactions and hydrothermal environments in the chondrite-like core of Enceladus. *Nature Communications*, *6*(1), 8604. https://doi.org/10.1038/ncomms9604

Shafer, N., & Zare, R. (1991). Through a beer glass darkly. *Physics Today*, *44*(10), 48–52. https://doi.org/10.1063/1.881294

Southworth, B. S., Kempf, S., & Spitale, J. (2019). Surface deposition of the Enceladus plume and the zenith angle of emissions. *Icarus*, *319*. https://doi.org/10.1016/j.icarus.2018.08.024

Srama, R., Ahrens, T. J., Altobelli, N., Auer, S., Bradley, J. G., Burton, M., Dikarev, V. V., Economou, T., Fechtig, H., Görlich, M., Grande, M., Graps, A., Grün, E., Havnes, O., Helfert, S., Horanyi, M., Igenbergs, E., Jessberger, E. K., Johnson, T. V., … Zook, H. A. (2004). The Cassini cosmic dust analyzer. *Space Science Reviews*, *114*(1–4), 465–518. https://doi.org/10.1007/s11214-004-1435-z

Sugahara, H., Takano, Y., Ogawa, N. O., Chikaraishi, Y., & Ohkouchi, N. (2017). Nitrogen Isotopic Fractionation in Ammonia during Adsorption on Silicate Surfaces. *ACS Earth and Space Chemistry*, *1*(1), 24–29. https://doi.org/10.1021/acsearthspacechem.6b00006

Takahagi, W., Seo, K., Shibuya, T., Takano, Y., Fujishima, K., Saitoh, M., Shimamura, S., Matsui, Y., Tomita, M., & Takai, K. (2019). Peptide Synthesis under the Alkaline Hydrothermal Conditions on Enceladus. *ACS Earth and Space Chemistry*, *3*(11), 2559–2568. https://doi.org/10.1021/acsearthspacechem.9b00108

Teolis, B. D., Perry, M. E., Hansen, C. J., Waite, J. H., Porco, C. C., Spencer, J. R., & Howett, C. J. A. (2017). Enceladus Plume Structure and Time Variability: Comparison of Cassini Observations. *Astrobiology*, *17*(9), 926–940. https://doi.org/10.1089/ast.2017.1647

Thomas, P. C., Tajeddine, R., Tiscareno, M. S., Burns, J. A., Joseph, J., Loredo, T. J., Helfenstein, P., & Porco, C. (2016). Enceladus's measured physical libration requires a global subsurface ocean. *Icarus*, *264*, 37–47. https://doi.org/10.1016/j.icarus.2015.08.037

Ulibarri, Z., Petro, E., Seixas, M., & Jia-Richards, O. (2023). Ultra-Long Baseline Time-of-Flight Mass Spectrometry with the AMIGAS Multi-Spacecraft Concept. *IEEE Aerospace Conference Proceedings*, *2023-March*, 1–9. https://doi.org/10.1109/AERO55745.2023.10115815

Vance, S. D., Craft, K. L., Shock, E., Schmidt, B. E., Lunine, J., Hand, K. P., McKinnon, W. B., Spiers, E. M., Chivers, C., Lawrence, J. D., Wolfenbarger, N., Leonard, E. J., Robinson, K. J., Styczinski, M. J., Persaud, D. M., Steinbrügge, G., Zolotov, M. Y., Quick, L. C., Scully, J. E. C., … Elder, C. M. (2023). Investigating Europa's Habitability with the Europa Clipper. *Space Science Reviews*, *219*(8). https://doi.org/10.1007/s11214-023-01025-2

Vance, S. D., Journaux, B., Hesse, M., & Steinbrügge, G. (2021). The Salty Secrets of Icy Ocean Worlds. *Journal of Geophysical Research: Planets*, *126*(1), 1–5. https://doi.org/10.1029/2020JE006736

Vance, S. D., Panning, M. P., Stähler, S., Cammarano, F., Bills, B. G., Tobie, G., Kamata, S., Kedar, S., Sotin, C., Pike, W. T., Lorenz, R., Huang, H. H., Jackson, J. M., & Banerdt, B. (2018). Geophysical Investigations of Habitability in Ice-Covered Ocean Worlds. *Journal of Geophysical Research: Planets*, *123*(1). https://doi.org/10.1002/2017JE005341

Verbiscer, A., French, R., Showalter, M., & Helfenstein, P. (2007). Enceladus: Cosmic Graffiti artist caught in the act. *Science*, *315*(5813), 815. https://doi.org/10.1126/science.1134681

Villanueva, G. L., Hammel, H. B., Milam, S. N., Kofman, V., Faggi, S., Glein, C. R., Cartwright, R., Roth, L., Hand, K. P., Paganini, L., Spencer, J., Stansberry, J., Holler, B., Rowe-Gurney, N., Protopapa, S., Strazzulla, G., Liuzzi, G., Cruz-Mermy, G., El Moutamid, M., … Denny, K. (2023). JWST molecular mapping and characterization of Enceladus' water

plume feeding its torus. *Nature Astronomy*, *7*(9), 1056–1062. https://doi.org/10.1038/s41550-023-02009-6

Waite, J. H., Burch, J. L., Brockwell, T. G., Young, D. T., Miller, G. P., Persyn, S. C., Stone, J. M., Wilson, P., Miller, K. E., Glein, C. R., Perryman, R. S., McGrath, M. A., Bolton, S. J., McKinnon, W. B., Mousis, O., Sephton, M. A., Shock, E. L., Choukroun, M., Teolis, B. D., … Siegmund, O. H. W. (2024). MASPEX-Europa: The Europa Clipper Neutral Gas Mass Spectrometer Investigation. *Space Science Reviews*, *220*(3). https://doi.org/10.1007/s11214-024-01061-6

Waite, J. H., Combi, M. R., Ip, W., Cravens, T. E., Jr., R. L. M., Kasprzak, W., Yelle, R., Luhmann, J., Niemann, H., Gell, D., Magee, B., Fletcher, G., Lunine, J., & Tseng, W. (2006). Cassini Ion and Neutral Mass Spectrometer: Enceladus Plume Composition and Structure. *Science*, *1419*(2006), 1419–1422. https://doi.org/10.1126/science.1121290

Waite, J. H., Glein, C. R., Perryman, R. S., Teolis, B. D., Magee, B. A., Miller, G., Grimes, J., Perry, M. E., Miller, K. E., Bouquet, A., Lunine, J. I., Brockwell, T., & Bolton, S. J. (2017). Cassini finds molecular hydrogen in the Enceladus plume: Evidence for hydrothermal processes. *Science*, *356*(6334), 155–159. https://doi.org/10.1126/science.aai8703

Waite, J. H., Lewis, W. S., Magee, B. A., Lunine, J. I., McKinnon, W. B., Glein, C. R., Mousis, O., Young, D. T., Brockwell, T., Westlake, J., Nguyen, M. J., Teolis, B. D., Niemann, H. B., McNutt, R. L., Perry, M., & Ip, W. H. (2009). Liquid water on Enceladus from observations of ammonia and 40Ar in the plume. *Nature*, *460*(7254), 487–490. https://doi.org/10.1038/nature08153

Woolf, D. K., Leifer, I. S., Nightingale, P. D., Rhee, T. S., Bowyer, P., Caulliez, G., de Leeuw, G., Larsen, S. E., Liddicoat, M., Baker, J., & Andreae, M. O. (2007). Modelling of bubble-mediated gas transfer: Fundamental principles and a laboratory test. *Journal of Marine Systems*, *66*(1–4), 71–91. https://doi.org/10.1016/j.jmarsys.2006.02.011

Waite, J. H., Lewis, W. S., Kasprzak, W. T., Anicich, V. G., Block, B. P., Cravens, T. E., Fletcher, G. G., Ip, W.-H., Luhmann, J. G., Mcnutt, R. L., Niemann, H. B., Parejko, J. K., Richards, J. E., Thorpe, R. L., Walter, E. M., & Yelle, R. V. (2004). The Cassini Ion and Neutral Mass Spectrometer (INMS) Investigation. *Space Science Reviews*, *114*(1–4), 113–231. https://doi.org/10.1007/s11214-004-1408-2

Waite, J. H., Lewis, W. S., Magee, B. A., Lunine, J. I., McKinnon, W. B., Glein, C. R., Mousis, O., Young, D. T., Brockwell, T., Westlake, J., Nguyen, M. J., Teolis, B. D., Niemann, H. B., McNutt, R. L., Perry, M., & Ip, W. H. (2009). Liquid water on Enceladus from observations of ammonia and 40Ar in the plume. *Nature*, *460*(7254), 487–490. https://doi.org/10.1038/nature08153

Wolf-Gladrow, D. A., Zeebe, R. E., Klaas, C., Körtzinger, A., & Dickson, A. G. (2007). Total alkalinity: The explicit conservative expression and its application to biogeochemical processes. *Marine Chemistry*, *106*(1-2 SPEC. ISS.), 287–300. https://doi.org/10.1016/j.marchem.2007.01.006

Yang, M., Smyth, T. J., Kitidis, V., Brown, I. J., Wohl, C., Yelland, M. J., & Bell, T. G. (2021). Natural variability in air–sea gas transfer efficiency of CO2. *Scientific Reports*, *11*(1), 1–9. https://doi.org/10.1038/s41598-021-92947-w

Yeoh, S. K., Li, Z., Goldstein, D. B., Varghese, P. L., Levin, D. A., & Trafton, L. M. (2017). Constraining the Enceladus plume using numerical simulation and Cassini data. *Icarus*, *281*, 357–378. https://doi.org/10.1016/j.icarus.2016.08.028

Zhang, W., Wu, S., Ren, S., Zhang, L., & Li, J. (2015). The modeling and experimental studies on the diffusion coefficient of CO2 in saline water. *Journal of CO2 Utilization*, *11*, 49–53. https://doi.org/10.1016/j.jcou.2014.12.009

Zhang, Y., & Xu, Z. (2008). "Fizzics" of bubble growth in beer and champagne. *Elements*, *4*(1), 47–49. https://doi.org/10.2113/GSELEMENTS.4.1.47

Zandanel, A., Truche, L., Hellmann, R., Myagkiy, A., Choblet, G., & Tobie, G. (2021). Short lifespans of serpentinization in the rocky core of Enceladus: Implications for hydrogen production. *Icarus*, *364*(January), 114461. https://doi.org/10.1016/j.icarus.2021.114461

Zolotov, M. Y. (2007). An oceanic composition on early and today's Enceladus. *Geophysical Research Letters*, *34*(23), 1–5. https://doi.org/10.1029/2007GL031234